EXPLORING THE IMPACT OF TiO_2 SURFACE CHEMISTRY ON NUCLEATION AND GROWTH OF PEROVSKITE ACTIVE LAYERS FOR PHOTOVOLTAIC APPLICATIONS

by

Kara C. Saunders

A Thesis Submitted to the Faculty of the

DEPARTMENT OF CHEMISTRY & BIOCHEMISTRY

In Partial Fulfillment of the Requirements

For the Degree of

MASTER OF SCIENCE

In the Graduate College

THE UNIVERSITY OF ARIZONA

2019

THE UNIVERSITY OF ARIZONA
GRADUATE COLLEGE

As members of the Master's Committee, we certify that we have read the thesis prepared by Kara C. Saunders, titled *Exploring the Impact of TiO_2 Surface Chemistry on Nucleation and Growth of Perovskite Active Layers for Photovoltaic Applications* and recommend that it be accepted as fulfilling the dissertation requirement for the Master's Degree.

Prof. Jeanne E. Pemberton Date: 11/26/2018

Prof. S. Scott Saavedra Date: 11/26/2018

Final approval and acceptance of this thesis is contingent upon the candidate's submission of the final copies of the thesis to the Graduate College.

I hereby certify that I have read this thesis prepared under my direction and recommend that it be accepted as fulfilling the Master's requirement.

Prof. Neal R. Armstrong Date: 11/26/2018
Master's Thesis Committee Chair
Department of Chemistry & Biochemistry

ACKNOWLEDGMENT

The author acknowledges Dr. R. Clayton Shallcross for his mentorship, specifically regarding XPS fitting, for sharing unpublished data that aided in the interpretation of data presented in this thesis, and for always making himself available for scientific discussions. The author also acknowledges Prof. Michael F. Toney and Dr. Tim J. Dunn at the Stanford Synchotron Radiation Lightsource (SSRL) at SLAC National Accelerator Laboratory and James Stanfill for fruitful discussions about the GIWAXS data acquired on Beamline 11-3.

Table of Contents

Abstract

We introduce lead ions adsorbed to TiO_2 as a surface modification, which serves as a model system to begin understanding how the chemistry at the TiO_2/perovskite interface influences nucleation and growth of mixed-halide cesium perovskites. The surface chemistry of TiO_2 was incrementally changed by subjecting the thin films to both oxygen and argon plasma treatment and lead adsorption thereafter. A combination of x-ray photoelectron spectroscopy (XPS), x-ray diffraction (XRD), grazing-incidence wide-angle x-ray scattering (GIWAXS), and atomic force microscopy (AFM) were used to evaluate the surface chemistry, crystallinity, and morphology of both the modified TiO_2 and the perovskite active layer on TiO_2 with the hypothesis that lead adsorption on TiO_2 would aid in the initial nucleation of the perovskite film by decreasing interfacial disorder by titrating away the reactive hydroxyl sites on the surface. By photoemission spectroscopy, we show that lead adsorbed from PbI_2 preferentially binds to TiO_2 at surface hydroxyl sites with a surface coverage ranging from 26-68% of a monolayer depending on the initial surface treatment. GIWAXS data reveals that perovskites on TiO_2 exhibit crystal growth with greater preferential orientation of the (100) axis perpendicular to the surface normal and that the degree of preferential orientation depends on the availability of surface hydroxyl sites for the perovskite precursor materials to bind to. Moreover, perovskite films exhibited greater crystallinity and coherence lengths on substrates that have more available hydroxyl groups, such as as-deposited TiO_2. AFM images evaluating the morphology of the perovskite films are consistent with findings acquired by XPS, XRD, and GIWAXS, demonstrating that atomic-scale changes to the interfacial region of this system result in changes visible at the top surface of the perovskite film. Although the data does not support the initial hypothesis, this work highlights the

critical importance that adjacent hydroxyl groups have in the nucleation and growth of perovskite films. Passivation of these reactive sites by lead adsorption inhibits the initial crystal growth. Ultimately, understanding the importance of the reactive sites on TiO_2 paves the way for future work on controlling hydroxyl density with the intent of controlling the nucleation and growth of perovskite active layers on TiO_2 for photovoltaic applications.

Chapter I: Introduction

1.1 Introduction

Perovskites are a next-generation active layer material in photovoltaics and other optoelectronic devices that have captivated scientists at the intersection of chemistry, materials science, and physics with their rapid gain in power conversion efficiency beginning at 3.8% in 2009[1] to 22.1%[2]. Additionally, these new materials are cheaply fabricated as thin films with favorable (and tunable) band gaps[3-6], and carrier mobilities[7-8] by various solution-processing methods, which has opened the possibility of devices that can be manufactured in a roll-to-roll process[9,18]. Perovskite materials are of the general formula ABX_3, where A is a monovalent cation, like methylammonium (MA, $CH_3NH_3^+$) or formamidinium (FA, $CHNH_2NH_2^+$) or cesium, B is a divalent metal that can form octahedral complexes, such as lead (II), and X is chloride, bromide, iodide or mixtures thereof. Figure 1.1 shows the general crystal structure. Recent work by Snaith and colleagues and McGehee and colleagues have shown photovoltaic devices with a power conversion efficiency of ca. 10% that utilize

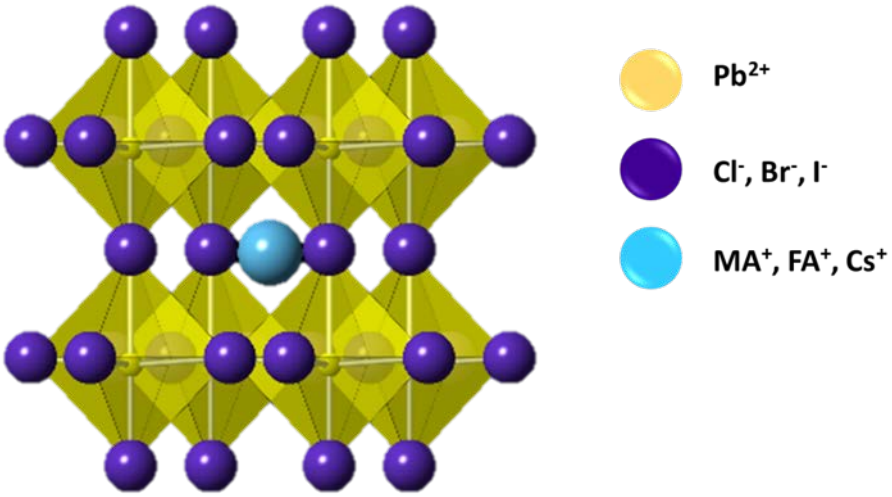

Figure 1.1: Perovskite crystal structure. The perovskite crystal lattice has a characteristic cage-like structure that is formed by eight corner-sharing octahedra with the central cation occupying the site in the center.

$CsPbBr_xI_{3-x}$ as the active layer, which has shown to improve stability over perovskites that utilize an organic cation (MA^+ and/or FA^+) upon exposure to ambient atmosphere [10,11].

Device-relevant perovskite deposition is often done on TiO_2, a common electron selective interlayer[12, 13]. As with other metal oxides, such as indium tin oxide (ITO), the surface chemistry of TiO_2 is amphoteric in nature upon exposure to water vapor[15, 16], which can occur at any step of device processing that does not occur *in vacuo*. Optimization of this surface chemistry through various cleaning procedures and/or surface modification is essential for maximizing the charge harvesting capability of TiO_2 in an optoelectronic device. The energetic offsets of TiO_2 (i.e. the HOMO and LUMO levels) and the Fermi level govern the charge collection efficacy. Any interfacial disorder from chemical changes that impact the energetics results in a myriad of deleterious effects, namely introduction of charge injection barriers, and changes to the surface free energy that inhibit complete wetting of a film during solution processing[17]. Moreover, the energetics of perovskite materials have been shown to be heavily impacted by the energetics of the substrate[19,20]. Thus, controlling the surface chemistry of TiO_2 is critical for both the electrode energetics and the perovskite energetics. In addition to the surface energetics, the crystalline perovskite layer must nucleate on the TiO_2 surface, which is chemically reactive. There is a need for the understanding of how the perovskite precursors interact with TiO_2 and specifically if the TiO_2 surface chemistry can be tuned to control the nucleation and growth of perovskite films.

Perovskites based on a cesium central cation, such as $CsPbBrI_2$ require annealing temperatures in excess of 300°C[81], which limits surface modification of TiO_2 to species that can withstand the high temperatures, (e.g. not organic molecules, as they begin to degrade at these temperatures). This thesis presents work that focuses on studying the effect of

surface modification on TiO_2 using lead adsorption from solution, as TiO_2 has already been implemented for extracting heavy metals from aqueous solution[21-24]. We hypothesize that lead adsorption on TiO_2 will first make the TiO_2 surface less reactive by having Pb^{2+} bound to the most reactive sites on the surface, thus decreasing the interfacial disorder once perovskite deposition occurs. Additionally, we suggest that the morphological heterogeneity of TiO_2 films introduces reactive sites on the TiO_2 surface that would be kinetically slow, yet thermodynamically favorable for perovskite precursor species to bind. Lastly, we hypothesize that lead adsorbed on TiO_2 acts as nucleation sites for the perovskite, whereby the precursor halide ions can displace the residual solvent coordinated to the lead bound to the surface, which has already passivated the most reactive sites on the metal oxide. Surface modification by precursor ion adsorption provides a previously undescribed method of modifying the active layer/electron selective layer interface without introducing any foreign chemical species, such as a carbonaceous self-assembled monolayer.

We characterize the surface chemistry of TiO_2 as-deposited (AD TiO_2) and TiO_2 treated with argon (AP TiO_2) and oxygen plasma (OP TiO_2) using X-ray photoelectron spectroscopy and compare these bare substrates to TiO_2 that is then treated by lead adsorption from DMF solution. Furthermore, we study the effect lead adsorption has on the crystallinity of the perovskite film and the preferential orientation of the film crystallites. Lastly, we observe the influence of the TiO_2 surface chemistry on the morphology of the perovskite film by atomic force microscopy. We show that plasma treatment of TiO_2 with argon works to remove adventitious carbon while preserving the surface chemistry of the as-deposited TiO_2 whereas oxygen plasma treatment introduces a molecular oxygen species that binds to the surface at Ti^{3+} sites, which de-dopes the TiO_2 in the near-surface region.

When the substrates are treated with lead, the lead chemically binds in a bidentate fashion to neighboring hydroxyl groups with a surface coverage of ca. 2-6 x 10^{-11} mol/cm^2, or 26-68% of a monolayer. Contrary to the initial hypothesis, lead-treated TiO_2 surfaces do not produce perovskite films that are more crystalline nor more coherent. However, the data presented in this thesis does illustrate the critical role of hydroxyl groups on TiO_2 in the nucleation and growth of perovskite thin films.

1.2 Perovskites as a Photoactive Material

Perovskite materials were first implemented in photovoltaic devices by Miyasaka *et al.* because they have favorable band gaps for sunlight absorption that are ca. 1.5-2.0 eV and demonstrate good excitonic and electronic properties for photovoltaic applications[1-5]. Perovskite materials reach an intermediate point between organic active layers and traditional silicon. Perovskite-based photovoltaics reach high power conversion efficiencies and have high carrier mobility like silicon yet can be solution processed onto flexible substrates, have a high absorptivity, and can be tunable based on their chemistry like organic photovoltaics.

Seminal work demonstrating the tunability of these perovskite materials has been carried out by Snaith and colleagues[6,7,10] and McGehee and colleagues[11] in which controlled compositional changes in the perovskite halogen content have been shown to change the band gap significantly. For example, these groups demonstrated that the band edge of all-inorganic perovskites with the form $CsPb(Br_xI_{1-x})_3$ can be tuned between 1.73 and 2.25 eV simply by halide substitution. A similar effect is achieved with cation substitution between

MA, FA, and Cs and mixtures thereof[25-30]. The band gap of the perovskite material has an inverse relationship with the ionic radius of the halide atom chosen. For example, the lowest band gap perovskite material is $MAPbI_3$, which has a band gap of *ca.* 1.5-1.6 eV. When bromine is substituted for iodine, the band gap increases to *ca.* 2.1-2.2 eV[2]. The same trend is observable with cesium-based perovskites as well, using UV-vis spectroscopy and X-ray diffraction to showcase that the band gap of $CsPb(Br_xI_{1-x})_3$ can be tuned between 1.7 and 2.3 eV and that there is a corresponding change in the unit cell parameters, with bromine-based perovskite reducing the unit cell dimensions from that of an iodine-based material[11]. With regard to cation substitution, the effects seen when replacing MA with FA are a result of the cation having a greater ability to stabilize the octahedra of the perovskite crystal structure into a particular conformation, e.g. cubic or tetragonal.

Despites these high efficiencies, perovskites encounter major long-term stability issues. They are moisture sensitive and subject to degradation back to their starting materials[33-34]. The degradation process can proceed with the organic central cation gaining a pair of electrons and leaving the crystal lattice as a gas[35]. Moreover, perovskites have a low free energy of formation. For example, Cahen, Hodes and colleagues have shown that a perovskite made from single crystal PbI_2 was found to have a free energy of formation of *ca.* 0.1 eV[36], which is quite low for a crystalline material. To put that number into context, gaseous hydrogen iodide, has a free energy of formation of ca. 1.3 eV, and solid TiO_2 (rutile) has a free energy of formation at 8.8 eV[79]. These numbers are summarized in table 1.1 below. To address these issues with stability, cesium has been incorporated as a replacement for the organic MA and FA cations; however, there are caveats and advantages. For example, replacing MA with Cs causes a slight increase in the optical band gap, which truncates the

Substance	ΔG (kJ/mol)	ΔG (eV)
$MAPbI_3$	9.6	0.1
HI (g)	1.3	1.0×10^{-2}
TiO_2 (rutile)	852.7	8.8

Table 1.1: A table comparing the free energies of formation between perovskite, HI, and TiO_2 with values given in both kJ/mol and eV. Note that 1 eV = 96 kJ/mol.

absorptivity of these materials in the near-IR region of the electromagnetic spectrum and thereby decreasing the solar cell efficiency. Despite the increase in band gap with these materials, this allows cesium perovskites to be incorporated as the front cell of a tandem photovoltaic. Tandem solar cells utilize two active layer materials with two different band gaps that can help mitigate voltage losses in the cell that would otherwise be lost as thermal energy and thus increases the open circuit voltage (V_{OC}) of the overall device. Cost-efficient "all-perovskite" tandem cells have already reported ca. 20% PCE[37,38], which will continue to increase over time as more advances are made in this field.

1.3 Perovskite Deposition Methods from Solution

Although perovskite deposition can be done either in vacuum or by spin-coating from solution, the most common method is a deposition from solution, as the appeal of these materials is their ability to be inexpensively cast from solution. Solution deposition methods can be divided into single-step and two-step methods, where a single-step method is a deposition from a solution that contains all the perovskite precursor salts (e.g. PbX_2, MAX, FAX, CsX, where X = Cl, Br, I) together in the desired molar ratios and a two-step method involves casting a precursor film followed by subsequent conversion to perovskite in a different step. Aforementioned work by Müller-Buschbaum and others[39] have showcased

that a particular perovskite crystallization pathway can be forced by a chosen deposition method.

A single-step method (Figure 1.2 A) is the most common method for producing mixed halide perovskites with a known stoichiometry because the molar ratios of the precursors can be precisely controlled. Most two-step methods that utilize mixed halides or mixed cations result in a final stoichiometry that must be ascertained from X-ray spectroscopies. Since all of the precursor solutions are co-solvated, the chemical equilibria and the different relative solubilities discussed above becomes even more important. Because this method

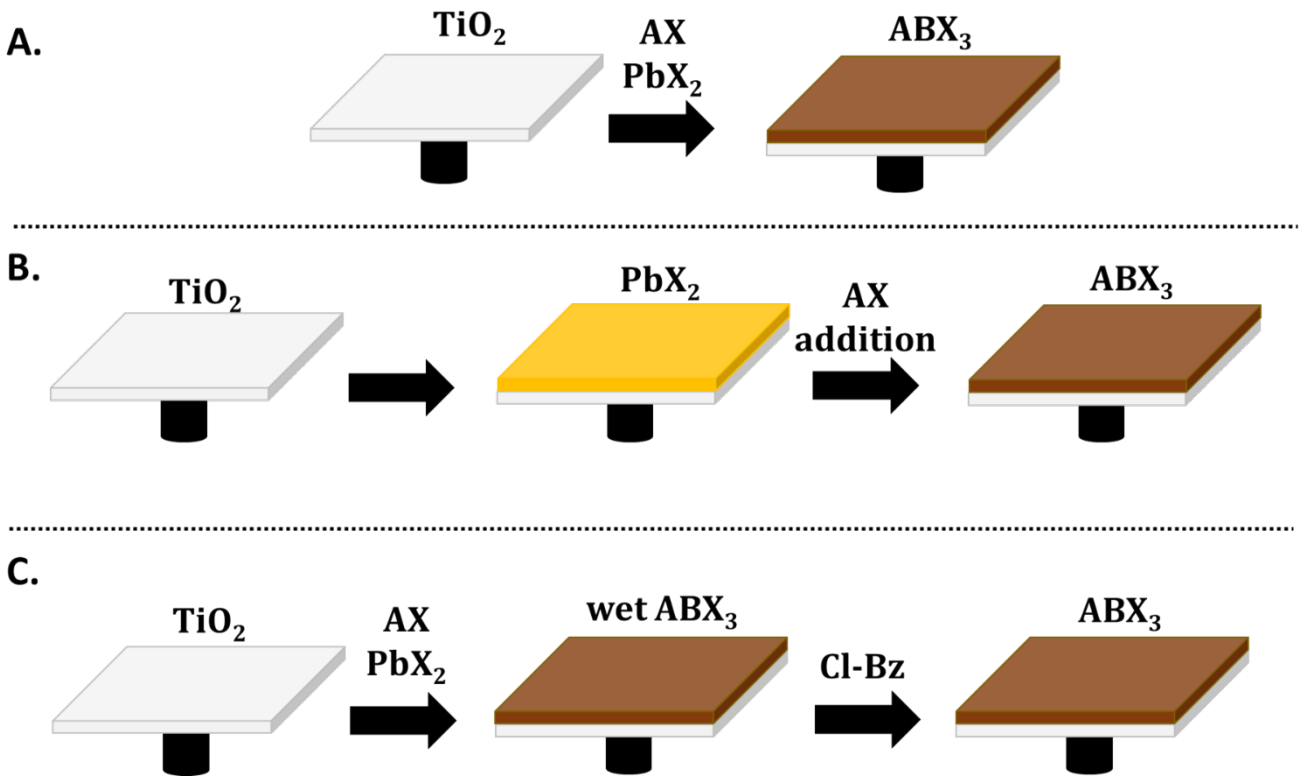

Figure 1.2: A pictorial representation of common perovskite deposition methods. (A.) shows the single step reaction in which the precursors, AX and AX_2 (X= Cl, Br, I) are combined in a single solution. (B.) Shows a common two-step deposition method wherein a film of PbX_2 and subsequently converted to perovskite by introducing the other precursor material. (C.) Shows perovskite preparation using the antisolvent method. The perovskite film is cast and while the film is still wet, an antisolvent, chlorobenzene (Cl-Bz) is added to the film to drive out excess solvent and promote the crystallization process.

directly forms the perovskite on the substrate, the substrate chemistry and crystallinity must be carefully considered when using this particular deposition method.

An important development in the single step deposition process is the antisolvent method (Figure 1.2 C), which involves addition of an antisolvent, most commonly chlorobenzene, that is dropped onto the wet film during spin coating[40,41]. Use of an antisolvent directs perovskite formation through a precipitation reaction. This process begins the crystallization of the perovskite since it is insoluble in this solvent and it helps to drives out the precursor solvent rather than allowing the solvent to evaporate, which reduces the effect that the substrate has on the nucleation and growth process. A study that used grazing-incidence wide-angle x-ray scattering (GIWAXS)[39] indicated that a major caveat of this deposition method is that the crystallization process appears to proceed through an uncontrolled growth mechanism, which is evident by the lack of preferential orientation of the (002)/(110) crystal planes of the perovskite.

Other variations on the single-step deposition method involve substituting the common lead source for the perovskite, lead iodide with lead acetate. When mixed-halide organic perovskite films are prepared using lead acetate instead of lead iodide, the resulting morphology is smoother. Work done by Estroff and colleagues show that the perovskite crystallization activation energy is lower when lead acetate is used as the precursor versus lead iodide or lead chloride[41]. Snaith and colleagues suggest that the acetate anion facilitates the driving out of excess organic materials, (i.e. excess methylammonium salt, solvent, and perovskite byproducts) which can inhibit crystal formation[43]. Moreover, the acetate anion is a Brønsted-Lowry base, which increases the scope of complex solution equilibria occurring

during the nucleation process. Thus, using acetate as the lead source increases the volatility of the perovskite byproducts, which in turn facilitates fast crystallization, smooth morphologies, and enhanced device performance Although this method seems to produce films with favorable properties, this method is not widely used because other methods have resulted in higher efficiency devices with low hysteresis.

Similarly, lead chloride has been used as a precursor salt in conjunction with methylammonium iodide (MAI) to form films with a $CH_3NH_3PbI_{3-x}Cl_x$ stoichiometry. The addition of chloride has shown to improve surface coverage of the perovskite film and has an increased V_{OC} compared to that of a film without any chloride. Moreover, the solar cell efficiency has seen an increase with the addition of chloride[44], although this finding could be the result of improved surface coverage. Most significantly, the addition of chloride has been shown to impact the initial crystallization of the perovskite structure by creating an intermediate pathway that has been observed by X-ray diffraction involving $MAPbCl_3$ that then proceeds into the final film stoichiometry, $CH_3NH_3PbI_{3-x}Cl_x$[44]. Chloride addition has also been studied by DFT and experimental methods at the perovskite/TiO_2 interface, which accumulates preferentially near the interface in a perovskite film[45].

Although many advancements have been made in understanding the crystal formation of the perovskite using single step deposition methods, a two-step deposition method (Figure 1.2B) has shown the largest increases in power conversion efficiency[46]. Most commonly, the two-step deposition method involves first casting a thin film of one of the precursor salts, which is usually lead iodide. The precursor film is then converted to perovskite by introducing the cation-containing precursor by a variety of methods including

(but not limited to) dip-coating, vapor conversion, or solution conversion. Perovskite deposition in two steps has shown to give higher efficiency devices than modified one-step methods[46]. The two-step methods first involve the deposition of a thin film of lead iodide and then the perovskite cation (methylammonium, formamidinium, or cesium) is introduced to the film by dip-coating, by vapor conversion, or by the intercalation method. A significant advantage that the two-step method has over single-step methods, is that the perovskite nucleation begins from an already oriented lead iodide film. Indeed, this has been shown to have preferential orientation by GIWAXS for the primary low-index plane of the perovskite to lie perpendicular to the substrate, which is the same orientation that the lead iodide film has in the case of solution conversion. The mechanism of this process is proposed to be an expansion and contraction of the PbI_6 octahedra to accommodate the central cation. This process can also occur during a post-deposition solvent vapor annealing step, which allows for mobile ionic species to diffuse and reincorporate themselves into the perovskite lattice by a dissolution-reconstruction process[47]. In general, the perovskite crystal structure can form through different reaction pathways, which are more readily accessible depending on the deposition method chosen. Despite that recent work[36] has shown a greater interest in the impact the substrate has on the final crystal structure, there is much work that remains to be done on understanding the TiO_2/perovskite interfacial chemistry. Specifically, questions remain regarding how the perovskite precursor materials interact with the TiO_2 surface and how the surface chemistry of TiO_2 impacts the nucleation and growth of perovskite materials in a way that maximizes the charge harvesting capability of TiO_2.

1.4 TiO_2 as an Electron Selective Interlayer

Titanium dioxide is one of the most thoroughly studied metal oxides because it sees widespread industrial use in sunscreens, pigments, coatings, and as a photocatalyst[48-52]. Additionally, TiO_2 has been utilized for decades as an electron selective interlayer in a multitude of photovoltaic platforms including dye-sensitized solar cells, organic photovoltaics, and perovskite solar cells due to the favorable energetic offsets of TiO_2 with respect to the active layer frontier orbital energetics, the high electron mobility within the material[52], and the stability of TiO_2 compared to the electronically similar zinc oxide.

TiO_2 is most effective as an electron selective layer and a photocatalyst in its anatase form[53-55]. TiO_2 anatase (Figure 1.3) is a tetragonal crystal system with titanium atoms that

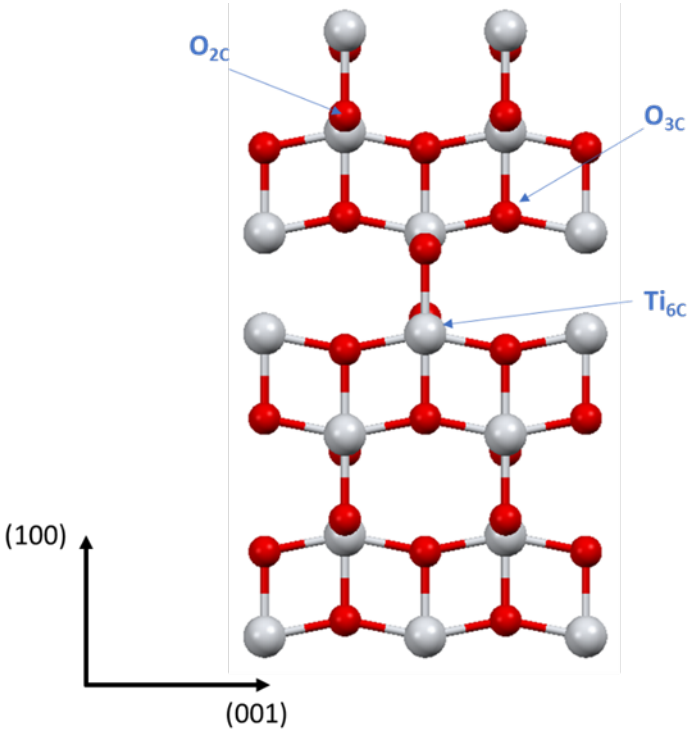

Figure 1.3: Crystal structure of TiO_2 anatase. Titanium atoms are shown in grey and oxygen atoms are shown in red. An example of oxygen atoms that are 2-fold coordinated and 3-fold coordinated are denoted by O_{2C} and O_{3C}, respectively. The titanium atoms are six-fold coordinated in the bulk of the material.

are 6-fold coordinated to oxygen atoms in an octahedron, which can be 2-fold coordinated or 3-fold coordinated. However, real systems often have defects in the bulk of the TiO_2 and have defects in the near-surface region that range in their chemical properties. Some of these defects include oxygen vacancies, where an oxygen is missing from an otherwise complete octahedron, resulting in a Ti_{5C} site. The defect density of TiO_2 can be controlled by subjecting the films to plasma treatments and different annealing temperatures[54], thus providing a variety of handles with which to alter the energy level alignment of TiO_2.

Like other metal oxides, the surface chemistry can be amphoteric in nature by both the Brønsted-Lowry and the Lewis acid-base definitions, as demonstrated by Diebold and Henderson[53,56]. Ti^{4+} can accept electrons and O^{2-} can donate an electron pair. If the surface of TiO_2 is exposed to water, the water can adsorb dissociatively and the hydrated surface can now have hydroxyl species and if there is a nearby species to screen the charge, aqua ligands can coordinate to the titanium octahedral centers[53]. In addition to the varied surface chemistry, TiO_2 can have defect sites, which include undercoordinated titanium centers (oxygen vacancies). These defects cause a shift of the core levels in X-ray photoemission spectroscopy (XPS) and form a gap state that is ca. 0.8 eV below the conduction band[57]. Moreover, the surface of TiO_2 itself is a defect because it is the termination of the crystal

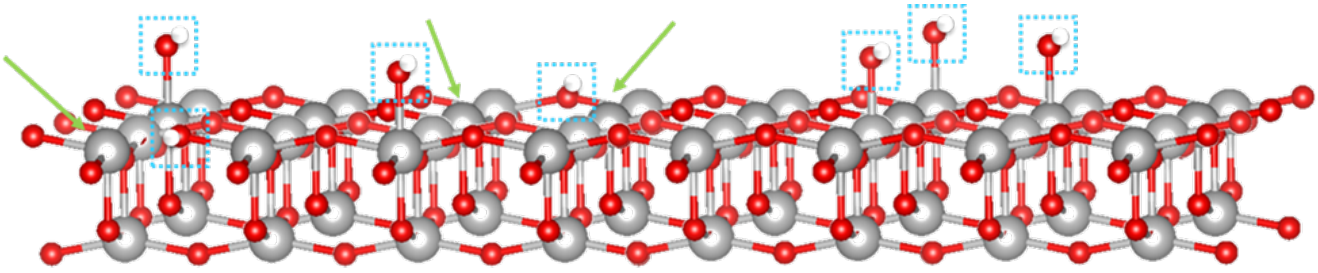

Figure 1.4: The surface of TiO_2 anatase. This surface has undercoordinated titanium atoms (oxygen vacancies) and hydroxyl groups that formed from bridging oxygen atoms at the surface. Green arrows indicate undercoordinated titanium atoms and hydroxyl groups are in cyan boxes.

lattice. This surface, which is shown in Figure1.4, shows the unique landscape that is formed when the crystal is terminated.

An additional property of TiO_2 anatase surfaces is a difference in reactivity between an atomically flat terraced region, versus a step-edge region. Diebold and colleagues were able to demonstrate this surface-region dependent reactivity by showing that water preferentially adsorbs onto step edges without dissociating and that water adsorbed onto a terraced region preferentially dissociates, thus hydroxylating the surface[14-16]. This preferential reactivity of TiO_2 depending on the surface morphology is important in identifying the reactive surface species of TiO_2 and the role that these reactive sites might play during perovskite deposition in which this non-inert surface will interact with perovskite precursor materials.

TiO_2 as both a bulk material and nanoparticles has previously been shown to be capable of heavy metal adsorption for environmental applications[21-24]. Work done by Jin and colleagues evaluated the adsorption of Pb on to TiO_2 from $Pb(NO_3)_2$ in aqueous solution, which can be modeled with the Langmuir isotherm[21]. Additionally, they determined that TiO_2 in its anatase form seem to be a more efficient absorber of lead than rutile TiO_2 and rutile/anatase mixtures, likely a result of different degrees of hydroxylation between the anatase and rutile surfaces[22]. Engates and Shipley performed exhaustion experiments on TiO_2 both as a bulk material and nanoparticles with Pb, Cd, Cu, Zn and Ni in which they determined that TiO_2 had a higher affinity for Pb than the other metals tested in solution[22]. A mechanism for the binding of lead accompanied by XPS spectroscopy data was presented by Nakayashiki and colleagues in an attempt to reveal the interfacial structure between

perovskite and TiO_2[75]. They showed improved perovskite photovoltaic device performance as a result of TiO_2 surface passivation. The surface chemistry of TiO_2 and how the reactive sites on the surface interact with perovskite precursor solutions remains an open investigation that also includes TiO_2 in different crystal forms and prepared by various deposition methods.

1.5 TiO_2 Thin Film Deposition Methods

TiO_2 surfaces can be prepared using a variety of methods, the most common of which include sol-gel deposition and chemical vapor deposition. Sol-gel deposition is done using a spin coater to deposit a thin layer of TiO_2 on a substrate. This TiO_2 deposition method is extremely versatile, as the substrates can be prepared and annealed in a variety of environments and at different temperatures to control the surface chemistry. The precursor material for this deposition process is commonly titanium tetraisopropoxide, $Ti(iPro)_4$ in IPA or ethanol and catalyzed with acid that is spin coated onto a substrate. The thickness of the TiO_2 layer can be controlled by tweaking the spin coating parameters.

The TiO_2 used in this work presented herein is fabricated by chemical vapor deposition (CVD), which has been shown to produce pinhole-free conformal films on indium tin oxide (ITO) that have been successfully integrated into an organic-based photovoltaic

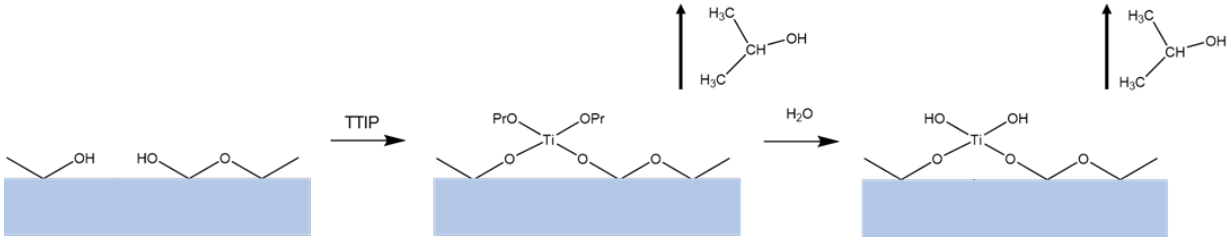

Figure 1.5: TiO_2 formation on an ITO surface from titanium (IV) tetraisopropoxide

device[12]. Additionally, this material, as prepared by CVD is believed to be polycrystalline with microdomains of TiO_2 anatase. The chemical vapor deposition process begins by bubbling ultra-high purity nitrogen, which acts as the carrier gas, through the precursor, liquid titanium tetraisopropoxide (TTIP). Nitrogen gas carries the precursor material through the chamber until it condenses on the heated substrates. The TTIP reacts with exposed hydroxyl groups on the surface (Figure 1.5), which releases gaseous alkoxyl groups. The bound $Ti(iPro)_2$ reacts with gaseous water vapor to form TiO_2 and again, gaseous alkoxyl groups are formed as a byproduct.

TiO_2 can also be prepared using atomic layer deposition (ALD). Similar to CVD, ALD allows for deposition of conformal films that have highly controllable thicknesses. However, ALD and CVD differ in the deposition mechanism. ALD must be done in cycles using ultrahigh vacuum, wherein a cycle consists of sequential chemical reactions that occur to form a single monolayer on the substrate. The limitation in this deposition method is the number of available reactive sites on the substrate surface, as all reaction vapors are purged away[58].

In general, TiO_2 is an extremely versatile material that can be prepared in ways to suit many needs. As an electron-selective interlayer, TiO_2 has a favorable band gap and can be prepared as a conformal layer on top of an electrical contact. However, the surface chemistry of TiO_2 is uniquely versatile, containing both acidic and basic sites capable of participating in chemical reactions with any active layer deposited on top of it, which can manifest as complications within the final device, such as a reduced charge-harvesting efficiency. Thus, understanding the TiO_2 surface chemistry and then understanding how perovskite materials behave once interfaced with TiO_2 introduces an active area of research that is critical for

advancing perovskites beyond an emerging photovoltaic material to one that can be brought to market on an industrial scale.

1.6 The Photovoltaic Effect

The photovoltaic effect describes the creation of a voltage and a current in a material upon photon absorption if the energy of the absorbed photon exceeds the band gap of the light-absorbing material: devices that utilize sunlight as the source of photons are solar cells. Solar cells are constructed as planar heterojunctions with a stacked architecture, as shown in Figure 1.6. The photoactive layer interfaces two electrical contacts and can either be a

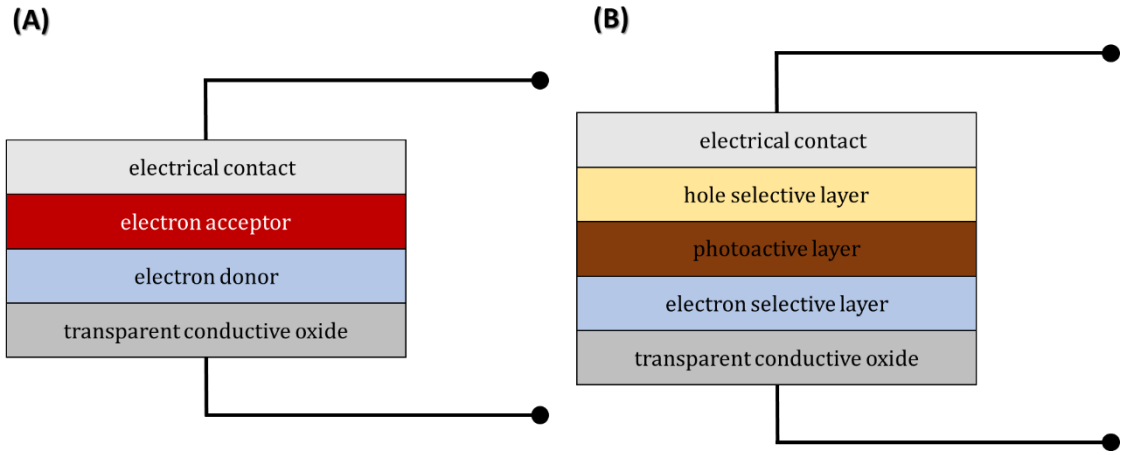

Figure 1.6: Schematic depicting planar heterojunction architecture of thin film photovoltaic devices with A. a donor/acceptor active layer and B. a P-I-N diode with charge-selective interlayers

donor/acceptor layer (Figure 1.6 A) or have a photoactive layer sandwiched between charge-selective interlayers (Figure 1.6 B). The materials between the electrical contacts are semiconductors that are doped, such that the material is electron-rich, electron-deficient, or neither. Semiconductors that have excess negative charge as a result of being electron-rich or hole-deficient are n-type semiconductors, whereas p-type semiconductors have excess

positive charge as a result of being electron-deficient or hole-rich materials, and intrinsic semiconductors lack significant concentrations of any dopants. When two or more of these materials are interfaced with one another with different degrees of doping, like a p-type and an n-type semiconductor for example, a space charge region forms as a result of charge carrier diffusion across the interface. The p-type semiconductor, which has a greater concentration of holes, acquires negative charge from electrons at the interface and the n-type semiconductor acquires positive charge from holes at the interface. This redistribution of charge at the interface results in band bending, which is seen as a change in the Fermi level as a direct result of the changing dopant concentration until Fermi level alignment between the two substances is achieved. If the band bending does not introduce an energetic barrier, then the charge carrier will move into the other material. The device acts as a P-I-N diode circuit element where three semiconductors, a p-type (hole selective), an intrinsic, and an n-type (electron selective) semiconductor are interfaced. If the current flow in the forward direction exceeds the current flow in the reverse direction by ca. three orders of magnitude, then rectification can be achieved by the device. This asymmetric current flow can only occur if there is proper energy level alignment (i.e. no energetic barriers to charge transfer) between the semiconductor materials, which is critical to constructing a photovoltaic device.

Figure 1.7 demonstrates the importance of choosing materials that allow for the flow of charge carriers without introducing energetic barriers.

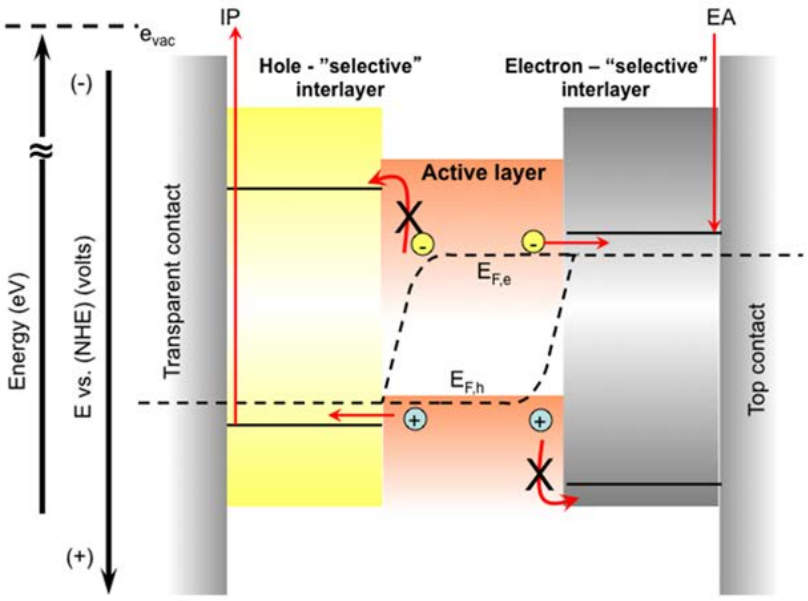

Figure 1.7: Block diagram of a thin film photovoltaic device demonstrating how charge carriers move between materials. Figure from Ref. 61

When semiconductors come into contact, charge equilibration forms the space charge region and Fermi level alignment is achieved within the materials. The Fermi level E_F is the average energy of electrons in the material, which can also be thought of as the chemical potential of the solid. A p-type material has the Fermi level closer to the valence band, an n-type material as the Fermi level closer to the conduction band, and an intrinsic semiconductor has the Fermi level located halfway between the valence band and the conduction band. The energetic offset between Fermi levels of semiconductors determines the degree of band bending at the interface[59-61]. Improper energy level alignment can introduce energetic charge injection barriers, which is an energetic cost for a charge carrier to migrate out of the active layer upon photoexcitation. Therefore, an ideal solar cell would

have all three semiconductor materials that have proper energy level alignment, meaning that the Fermi levels of the three materials are close enough in energy that it allows the charge carriers to diffuse across the interface along a favorable potential energy surface, but different enough in energy such that the charge carriers do not get trapped in a potential energy well where they have a high probability of recombination. Since the efficiency of a photovoltaic device is contingent on the charge collection efficiency of the respective interlayers, the ability to tune the energy level alignment is a powerful method to engineer high efficiency devices. Chemical modification of surfaces has been demonstrated as a handle for exploring electronic tunability of inorganic materials.

1.7 Surface Modification of Metal Oxides

Methods for tuning the energy level alignment of a solid all focus on changing the Fermi level or the local vacuum level of that material. The Fermi level dictates the work

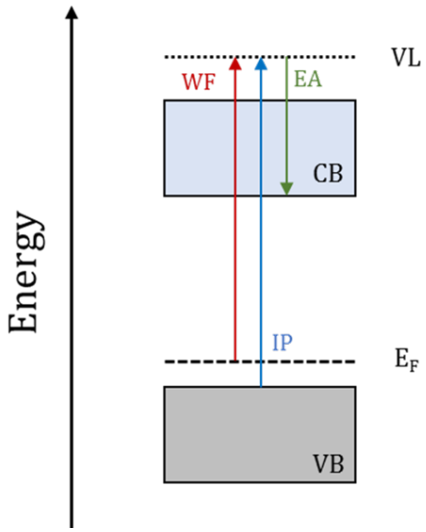

Figure 1.8: Band diagram of a p-type semiconductor. The work function (red arrow) is the energy required to eject an electron. The ionization potential (blue arrow), is the energy gap between the top of the valence band and the vacuum level. The electron affinity (green arrow) and is defined as the energy gap between the bottom of the conduction band and the vacuum level.

function, the location of the valence band affects the ionization potential, and the location of the conduction band affects the electron affinity, as shown in Figure 1.8. The Fermi level and/or the local vacuum level can be tuned by chemical modification of a material. The work function of a surface/interface can be described using an electrostatic model[62], in which the energy level alignment of an interfacial system, like a self-assembled monolayer (SAM) on a metal, relies on the potential step across the interface, which can be impacted by the formation of a dipole induced by the SAM. Depending on the orientation of the dipole moment, this can either raise or lower the work function of a material, seen as a redistribution of charge density at the surface, which forms an electric field, as shown in Figure 1.9. When the dipole moment is oriented along the surface normal, a work function increase is observed due to an induced Coulombic repulsion by the electron density

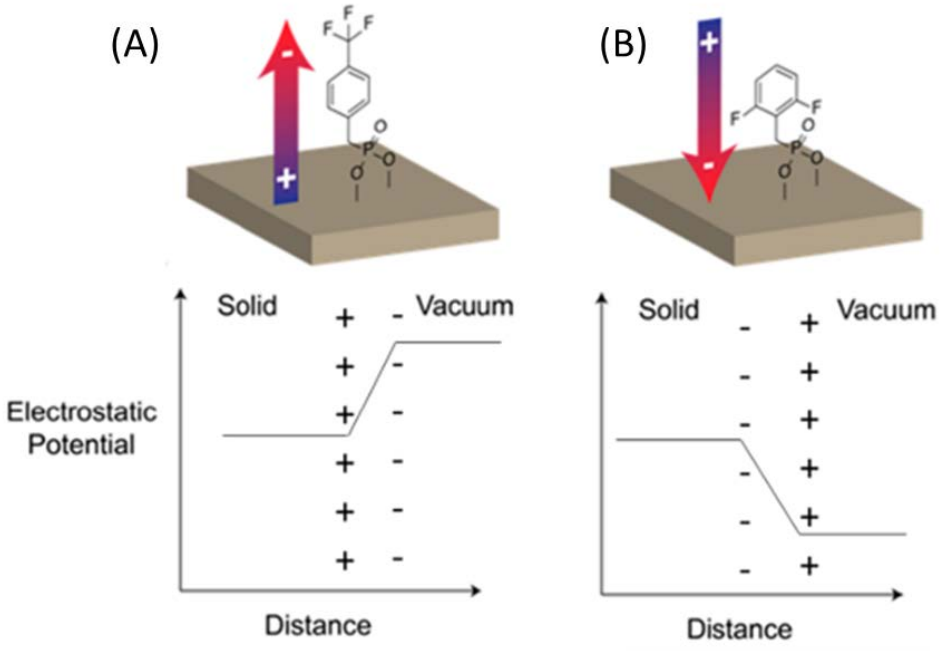

Figure 1.9: An example of how the molecular dipole of a self-assembled monolayer can impact the interface dipole formed upon adsorption depending on the orientation of the dipole along the surface normal and the subsequent effect the dipole has on the work function using an electrostatic model. The SAM increases the work function in (A) and decreases the work function in (B). Figure from Ref. 63

associated with the molecular dipole that a photoelectron experiences as it is ejected from the surface. Conversely, a SAM that produces a larger electron density closer to the surface rather than at the tail end will have a lower work function resulting from an electrostatic attraction, thus lowering the energetic barrier for the electron to eject from the surface. Thus, self-assembled monolayers change the energetics of a system by changing the electric field density at the surface, which impacts the local vacuum level and therefore the work function[63]. A noteworthy caveat to this phenomenological description is that it does not account for strong surface/adsorbate interactions, like coupling though a true chemical bond with the surface or hybridization between the adsorbate and the dangling orbitals of the surface. Therefore, it is necessary to discuss changes to the Fermi level of a material by doping.

Dopants can be intrinsic to the semiconductor or introduced to it, thus forming an extrinsic semiconductor. The doping species can either be another atom, like in the case of the III-V semiconductors such as gallium nitride, gallium phosphide, and gallium arsenide, or defects within the material. For example, oxygen vacancies within metal oxides are reported to be the primary source of doping within thin films of TiO_2[64], resulting in a greater concentration of electrons therefore making the TiO_2 more n-type. Tailoring the defect density of TiO_2 or any other semiconductor is critical to the efficacy of whatever role the semiconductor plays in a system in which it is implemented.

Shallcross *et al.* presented a comprehensive study that highlights the critical role of the TiO_2 surface chemistry in the nucleation and growth of perovskite films deposited *in vacuo*, wherein they were able to determine that specific sites on the chemically heterogeneous metal oxide surface react with the methylammonium lead halide perovskites

adversely[66]. In contrast, they were able to show that surface modification of TiO_2 with silanes passivated reactive sites on the TiO_2 that would otherwise prevent the perovskite from forming. Moreover, they were able to show that surface modification has a favorable impact on the energetics by reducing the amount of band bending at the interface. Thus, charges that are generated in the perovskite layer will be screened more readily and should therefore increase the charge collection efficacy of TiO_2, which serves as the electron-selective interlayer. Although silane modification has been shown to enhance the nucleation and growth of methylammonium lead halide perovskite films, cesium-based perovskites require high temperature annealing at 350°C for complete conversion to the cubic (α) perovskite phase, which would result in degradation of the organic modifier.

1.8 Research overview

We introduce lead ion adsorption onto TiO_2 from solution as an alternative surface modifier that is simple and robust with the intent of passivating surface defects and homogenizing the surface upon which the perovskite active layer is deposited. We hypothesize that surface modification by lead adsorption allows for the lead ions to titrate away reactive sites on the TiO_2 surface (Figure 1.10 A) that would otherwise be kinetically slow to bind lead, but thermodynamically favorable since the adsorption experiment is done over a two-hour period. We hypothesize that once the lead ions are bound to the TiO_2, the surface is more chemically homogeneous, which results in the formation of an interface that has less disorder once the perovskite is deposited than that of the unmodified surface. Because the perovskite film must nucleate on the TiO_2 surface, any disorder on the TiO_2 leads

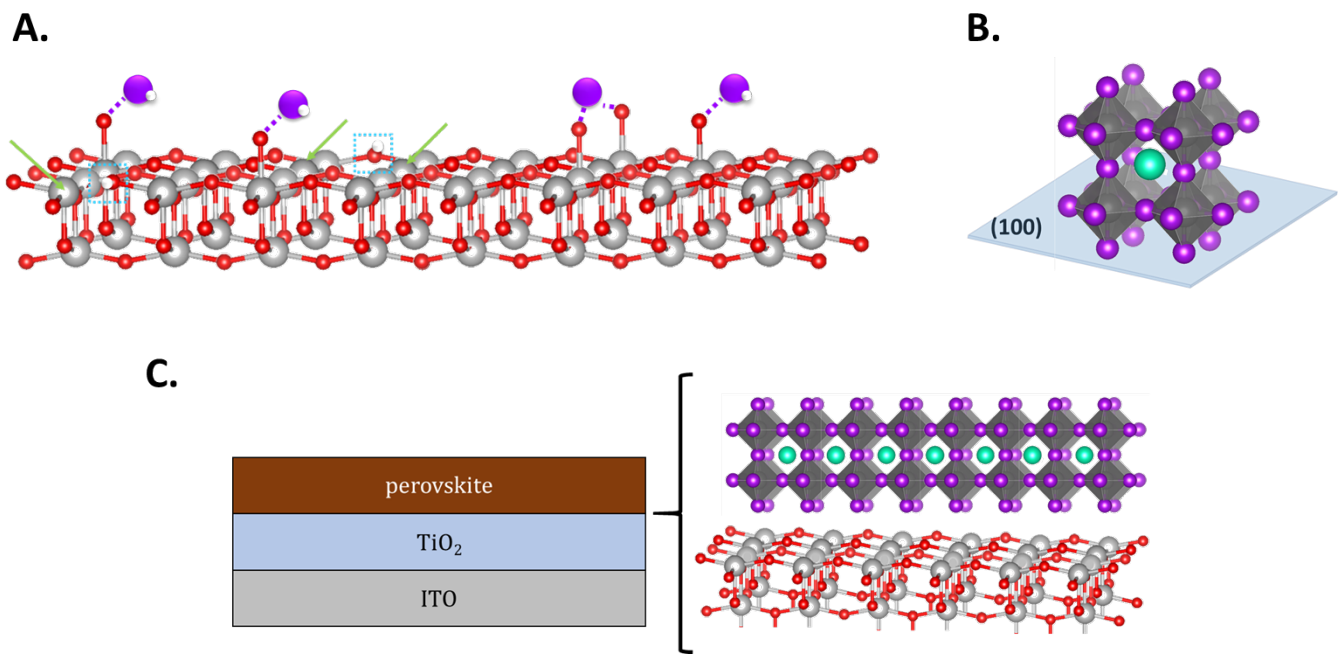

Figure 1.10: A. Idealized TiO_2 surface with adsorbed lead shown in purple bound to hydroxyl sites. Undercoordinated Ti atoms are indicated by green arrows. Hydroxyl groups are indicated in cyan boxes. B. Perovskite unit cell. The [100] direction of the perovskite unit cell contains the lead octahedral centers. C. Block diagram of the surfaces and interfaces relevant to this study, shown with TiO_2 and the perovskite unit cells (not to scale).

to disordered nucleation events that can disrupt crystallization of the film. Moreover, the lead ions on the surface are now coordinated to TiO_2 and are hypothesized in this study to act as nucleation sites for the perovskite, whereby the precursor halide ions can displace the residual solvent coordinated to the lead bound to the surface, which has already passivated the most reactive sites on the metal oxide. With the lead ions already on the surface, this is hypothesized to direct the crystallization of $CsPbBrI_2$ perovskites with a preference for the (100) crystallographic direction, which contains lead in the octahedral centers that form the cage-like structure of the perovskite (Figure 1.10 B). Controlling the nucleation and subsequent growth of the perovskite is critical for charge transport, especially if there is anisotropic transport along certain crystallographic directions[65]. Surface modification by precursor ion adsorption provides a previously undescribed method of modifying the active

layer/electron selective layer interface (Figure 1.10 C) without introducing any foreign chemical species, such as a carbonaceous self-assembled monolayer.

In the following chapters, this thesis presents experimental methods for the lead adsorption experiments and subsequent analysis (Chapter 2), work demonstrating that lead adsorption onto TiO_2 results in a range of surface coverages from 26-67% of a monolayer in Chapter 3, and conclusions and future directions in Chapter 4. Although the lead adsorption experiments are done at a high concentration, the surface coverage is limited to the amount of adjacent hydroxyl groups on the TiO_2 surface, as Pb requires bidentate binding. Although the data do not support the original hypothesis, as lead-modified oxide substrates produce unfavorable changes to the morphology, crystallinity, and preferential orientation of mixed halide cesium perovskite films, this body of work has highlighted the important role adjacent hydroxyl groups have in the initial nucleation and growth of perovskite thin films on TiO_2.

Chapter II: Experimental Procedures

2.1 Preparing ITO for TiO_2 Deposition

Indium tin oxide (ITO) on glass obtained from Colorado Concepts, Inc. are sonicated in a heated bath with 10% (v/v) Triton X in nanopure water, then acetone (EMD Millipore, ACS grade), followed by isopropanol (Fisher, ACS grade), each for 10 minutes. The ITO substrates are rinsed in ethanol (technical grade), then dried under a stream of N_2.

To remove adventitious carbon, the ITO pieces are placed into a bell jar that has been plasma cleaned for 30 minutes prior to substrate introduction. Oxygen plasma cleaning (Harrick plasma, Model PDC-32G) is done at a pressure of 800 mtorr for 10 minutes using 17 W. Argon plasma cleaning is done at 800 mtorr for 20 minutes.

2.2 Deposition of TiO_2

Thin films of titania (ca 25-30 nm thick, as measured by SEM cross-section) are deposited using chemical vapor deposition in a homebuilt chamber[12] from a liquid titanium (IV) isopropoxide (TTIP) (97%, Sigma-Aldrich) precursor. The chamber is pumped down to ca. 800 mTorr prior to deposition. Ultrahigh purity nitrogen is used as the carrier gas, which has a flow rate of 0.66 mL/min. The TTIP enters a tube furnace set at 180°C to prevent condensation and the ITO glass substrates are held at 210°C. Deposition occurs for 25 minutes and the substrates are cooled to 100°C before removing them from the chamber. Substrates are stored in the air away from light.

2.3 Lead Adsorption

Lead adsorption is done from a 30 mg/mL solution of PbI_2 in anhydrous dimethylformamide (Sigma Aldrich) within a nitrogen glovebox to ensure saturation coverage and to mitigate redox activity from ambient air. The TiO_2 substrates are submerged in the PbI_2 solution for 30 minutes at 70°C, then spin-rinsed with dimethylformamide (3x) to remove any physisorbed material and rinsed again (2x) with isopropanol that had been dried under molecular sieves and degassed with argon to remove residual DMF from the surface.

2.4 Drying Solvents for Use in the Glovebox

Solvents used in the glovebox are dried using 3 Å molecular sieves activated at 450°C. The sieves are placed in an amber jar and solvent is carefully poured over them while still hot. The solvent is left for 24 hours and then degassed with argon by bubbling for 30 minutes and then introduced into the glovebox.

2.5 Perovskite Deposition

$CsPbBrI_2$ perovskites are deposited from a single solution of CsI, PbI_2, and $PbBr_2$ with a total concentration of 0.4 M in DMF. The solution is stirred for ca. 45-60 minutes at 70°C prior to deposition. The TiO_2 was immediately transferred to the glovebox and annealed at

120°C for 20 minutes to remove any adsorbed water on the surface. The substrates were all removed from the hotplate at once. Immediately prior to deposition, the precursor solution was filtered through a 0.2 μm PTFE filter and remained at 70°C throughout. Perovskite films were deposited on the TiO_2 by spin coating using 25 μL of precursor solution at 2000 rpm for 30 seconds. The films were solvent vapor annealed with 60 μL DMF at 350°C for 10 minutes then cooled for 10 minutes with the lid off at room temperature.

2.6 XPS Characterization and Fitting

XPS data was collected on a Kratos Ultra Spectrometer equipped with a monochromatic Al Kα source (1486.7 eV) at a takeoff angle of 90° with respect to the sample surface. The analysis chamber had a base pressure of ca. 1×10^{-9} torr. High-resolution core level regions were collected with the analyzer pass energy set to 20 eV. Fitting of XPS data is done using Vision 2 processing software. Shirley backgrounds are used for all core levels.

The I 3d doublet is fit with a 30:70 Lorenzian:Gaussian Voight function. The change in binding energy between the $3d_{5/2}$ and the $3d_{3/2}$ is 11.5 eV and the FWHM of the peaks was set to 1.3 eV and the peaks maintained a 3:2 area ratio.

The O 1s envelope is fit with multiple peaks that correspond to different oxygen species with a constant binding energy relative to the TiO_2 lattice oxygen[69] which appears at ca. 530.7 eV. Each peak is a 30:70 Lorenzian:Gaussian Voight function. The bridging oxygen peak is set to a binding energy of lattice + 1.25 eV with a FWHM of 1.3 eV, and the "terminal OH" peak is set to a binding energy of lattice + 2.4 eV with a FWHM of 1.3 eV. For oxygen plasma treated samples, the high binding energy doublet assigned to superoxide has the

lower binding energy component at a binding energy of lattice + 5.9 eV and the higher binding energy component of the doublet is at lattice + 7.0 eV. Both components of the superoxide doublet have a FWHM of 1.3 eV. TiO_2 samples that have been treated by lead adsorption show a Pb-O feature at a binding energy of lattice - 1.9 eV and fit with a FWHM of 1.3 eV.

The Ti 2p doublet is fit with an asymmetric 70:30 Lorenzian:Gaussian Voight function[68] with the binding energy separation between the $2p_{3/2}$ and the $2p_{1/2}$ at 5.8 eV. The FWHM of the Ti $2p_{3/2}$ peak was 1.4 eV and the FWHM of the Ti $2p_{1/2}$ peak was 2.2 eV.

The C 1s envelope was fit with all other peaks relative to the C-C carbon peak, which is seen at ca. 285.0 eV. Singly oxidized carbon appears at 1.2 eV above the primary peak. Carbonyls are 3.2 eV above the primary peak, and O-C=O moieties appear at 3.7 eV higher than the primary peak. All carbon species peaks are fit with a FWHM of 1.5 eV.

The Pb 4f region was fit with two doublets. The first doublet is lead (II) and the second doublet is lead that has been oxidized. The binding energy difference between the two doublets is 0.9 eV. The FWHM was kept the same for all the peaks and was 1.1 eV for PbI_2 thin films and 1.35 eV for the Pb-adsorbed samples.

O 1s difference spectra are done by binding energy normalizing the spectra of interest to an arbitrary value of 530.7 eV. Differences are observed by subtracting the O 1s spectrum of a bare TiO_2 substrate from the O 1s spectrum of a TiO_2 substrate that had been treated by lead adsorption.

Angle-resolved XPS data was collected by changing the sample angle such that the photoelectrons were collected at an angle of 60° with respect to the surface.

2.7 AFM Image Acquisition

Atomic force microscopy (AFM) images were acquired on a Bruker Multimode 8 using ScanAsyst mode in air with the corresponding AFM cantilevers purchased from Bruker. The tips have a spring constant of 0.4 N/m and a resonant frequency of 70 kHz.

2.8 XRD Characterization

XRD data is collected as intensity as a function of angle, 2θ, which is acquired by sweeping through angles of the x-ray source and the detector, which are kept at the same angle. Diffraction peaks are observed as a result of constructive interference occurring from the incident radiation and the lattice spacing of the material, which are related by Bragg's law, where n is the diffraction order, λ is the incident wavelength of X-ray radiation, d is the spacing between diffracting planes, and ϑ is the incident and diffraction angle, shown in Equation 2.03.

$$n\lambda = 2d \sin\theta \qquad \text{(Eq. 2.1)}$$

X-ray diffractograms were collected on a Phillips X'PERT MPD instrument equipped with a monochromatic Cu anode (Cu Kα, 1.54 Å). The generator voltage was set to 45 kV with a tube current of 40 mA. Scans were done from 2ϑ= 5 - 65° with a step size of 0.0083°. Fityk[70] was used to subtract the background and fit peaks with a Pearson function to determine FWHM values of the Bragg peaks. An estimate of the average crystallite size is calculated for perovskites using the Scherrer equation (Eq. 2.04), where D is the average crystallite size, κ is a form factor, which is 0.96 for spherically symmetrical cubic systems, λ is the wavelength

of the incident X-ray radiation, β is the adjusted FWHM of the Bragg peak of interest including the natural line width of the instrument.

$$D = \frac{\kappa\lambda}{\beta \cos\vartheta} \qquad \text{(Eq. 2.2)}$$

2.9 GIWAXS

Grazing incident wide-angle X-ray scattering (GIWAXS) is a 2D X-ray scattering technique that uses an area detector rather than a point detector. Using an area detector allows one to see diffraction from crystal planes that are oriented in all directions in space.

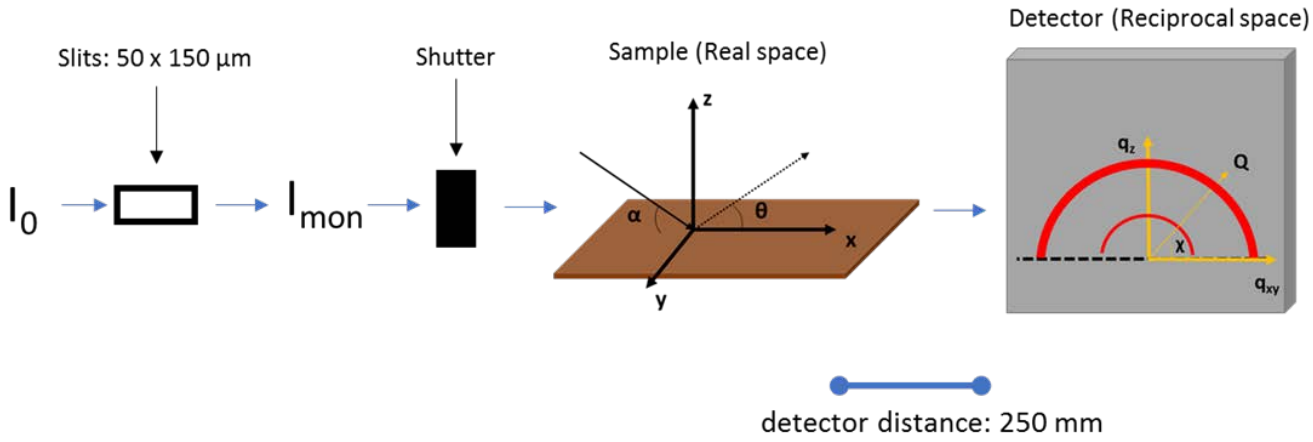

In contrast, an X-ray diffraction experiment using a point detector in the θ-2θ geometry to

Figure 2.1: An instrument schematic of the GIWAXS experimental setup at BL 11-3 at the Stanford Synchotron Radiation Lightsource

probe thin films can only probe crystal planes that lie parallel to a surface. Additionally, GIWAXS is a technique performed using synchotron radiation, which has a light intensity that is ca. 15 orders of magnitude greater than a copper anode and allows for extremely high throughput. An instrumental schematic is shown in Figure 2.1, where I_0 is the incident synchotron radiation, I_{mon} is the radiation that hits the sample after intensity loss from the

optics, α is the angle of the incident radiation measured with respect to the sample plane (xy), and θ is the diffraction angle. Each ring that appears on the image has a radius, Q that corresponds to the lattice spacing of that diffraction plane, which is intrinsic to the material and does not depend on the incident X-ray radiation wavelength, as shown in Equation 2.05.

$$Q = \frac{2\pi}{d} \qquad \text{(Eq. 2.3)}$$

Each Q value has q_Z and q_{XY} components, where q_Z is indicative of diffraction from planes that are perpendicular to the q_Z direction (in plane) and q_{XY} is indicative of diffraction from planes that are perpendicular to the q_{XY} plane (out of plane). The angle χ is the angle of Q with respect to q_{XY}.

GIWAXS experiments give two primary pieces of information. The first relates to the overall sample crystallinity and the second relates to the preferential orientation of the sample, which can both be extracted by linearizing a Debye-Scherrer ring, which is shown in Figure 2.2. Once linearized, the Debye-Scherrer ring is now realized as a multidimensional

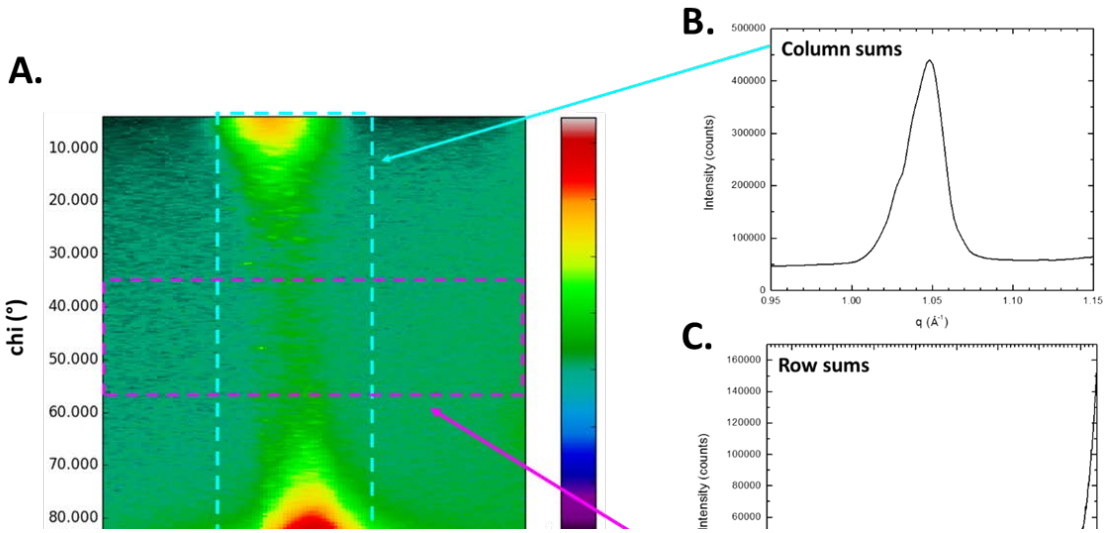

Figure 2.2: A linearized Debye-Scherrer ring is shown (A) with subsequent plots by integrating along the columns (B) and the rows (C). Column sums give an intensity versus q plot and row sums give an intensity versus angle with respect to the sample plane

figure with χ (degrees) on the vertical axis, q ($Å^{-1}$) on the horizonal axis, and intensity shown as color contrast. Integrating this figure along the columns gives a plot of intensity vs. q, which shows Bragg peak intensity as a function of lattice spacing by the relation given above in Eq. 2.05. From the column sums plot, one can acquire information about lattice spacing, strain, coherence length, and crystallinity. In contrast, the row sums plot, which is obtained by integrating the linearized Debye-Scherrer ring along the rows results in an intensity vs. chi plot, which shows Bragg diffraction intensity as a function of angle with respect to the sample plane. The row sums plot can give information about the orientation of the crystallographic diffraction planes and can indicate if the sample has any preferential orientation or an isotropic distribution of crystallites.

GIWAXS data was collected on Beamline 11-3 at the Stanford Synchotron Radiation Lightsource (SSRL). The incident radiation had an energy of ca. 12.7 keV, which provides an x-ray wavelength of 0.976 Å. The detector was positioned 250 mm away from the sample stage. A LaB_6 sample was used to calibrate the detector distance and was used to generate the calibration file that converts pixels to q-space. Each sample measured at Beamline 11-3 was subjected to the same measurement conditions. The incident angle was stepped from 0.10°-0.50° in increments of 0.05° for a total of 9 exposures. Exposure time to the x-rays for each sample was 30 seconds.

Chapter III: Results & Discussion

3.1 The Chemical Heterogeneity of TiO_2 and the Effect of Plasma Treatment Measured by X-ray Photoelectron Spectroscopy

The chemical composition of TiO_2 as-deposited (AD), argon plasma (AP) treated, and oxygen plasma (OP) treated TiO_2 was evaluated before and after lead adsorption from solution using X-ray photoelectron spectroscopy at collection angles of both 90° and 60°. High-resolution spectra were acquired for the O 1s, Ti 2p, C 1s, and Pb 4f regions.

The O 1s spectra (Figure 3.1) for AD and AP samples can be deconvoluted into three peaks, representative of lattice oxygen, bridging oxygen, and terminal hydroxyl species residing within the first 9 nm of the TiO_2 surface, where the probe depth of XPS sampling can be calculated using the universal curve for layer-by-layer growth[80] which is shown in Eq. 3.1,

$$\lambda_N = B_N(KE)^{1/2} \qquad (3.1)$$

where λ_N is the inelastic mean free path (IMFP), B_N is a constant of 0.096 nm/eV for inorganic materials, and KE is the kinetic energy of the core level, which is calculated using Eq. 3.2.

$$KE = h\nu - BE \qquad (3.2)$$

With KE being the kinetic energy of the detected photoelectron, $h\nu$ is the photon energy (1486.7 eV, Al Kα anode) and BE is the binding energy. The probe depth is $3\lambda_N$. OP treated samples, have a doublet at a high binding energy (ca. 536 eV) A doublet, which accounts for molecular oxygen, a paramagnetic species, bound to Ti_{5C} sites is added to the O 1s envelope for OP samples. Table 3.1. shows the O 1s peak positions for each of the oxygen species, which

Substrate	Oxygen species	BE (eV)	area %
AD*	O lattice	527.329 ± 0.144	79.4 ± 1.0
	O bridging	528.479 ± 0.144	15.4 ± 0.5
	O terminal	529.629 ± 0.144	5.2 ± 0.5
	O superoxide	nd	nd
AD-60*	O lattice	527.086	74.6
	O bridging	528.236	17.3
	O terminal	529.386	8.1
	O superoxide	nd	nd
ADPb*	O lattice	527.390 ± 0.084	80.2 ± 0.8
	O bridging	528.540 ± 0.084	15.0 ± 0.5
	O terminal	529.690 ± 0.084	4.7 ± 0.3
	O superoxide	nd	nd
ADPb-60*	O lattice	527.007	72.1
	O bridging	528.157	20.3
	O terminal	529.307	7.6
	O superoxide	nd	nd
AP	O lattice	530.672 ± 0.019	74.6 ± 0.5
	O bridging	531.822 ± 0.019	18.7 ± 0.4
	O terminal	532.972 ± 0.019	6.7 ± 0.2
	O superoxide	nd	nd
AP-60	O lattice	530.577	65.6
	O bridging	531.727	24.4
	O terminal	532.877	10.1
	O superoxide	nd	nd
APPb	O lattice	530.708 ± 0.010	76.7 ± 2.8
	O bridging	531.858 ± 0.010	16.7 ± 1.6
	O terminal	533.008 ± 0.010	6.6 ± 1.3
	O superoxide	nd	nd
APPb-60	O lattice	530.553	73.5
	O bridging	531.703	18.2
	O terminal	532.853	8.3
	O superoxide	nd	nd
OP	O lattice	530.295 ± 0.009	71.1 ± 2.4
	O bridging	531.445 ± 0.009	15.4 ± 0.5
	O terminal	532.595 ± 0.009	6.8 ± 1.4
	O superoxide	536. 077 ± 0.009	5.5 ± 0.4
OP-60	O lattice	530.267	65.4
	O bridging	531.399	18.0
	O terminal	532.567	9.9
	O superoxide	536.216	5.0
OPPb	O lattice	530.358	71.2 ± 0.3
	O bridging	530.358 ± 0.004	16.8 ± 0.4

	O terminal	531.508 ± 0.004	6.0 ± 0.5
	O superoxide	532.658 ± 0.004	6.1 ± 0.6
OPPb-60	O lattice	530.262	64.4
	O bridging	531.412	18
	O terminal	532.562	9.8
	O superoxide	536.191	6.2

Table 3.1: A list of binding energies and O 1s peak positions for every surface treatment including the angle-resolved data. Asterisks indicate that the binding energy had to be corrected for charging. The plus/minus values are standard deviations with n=3.

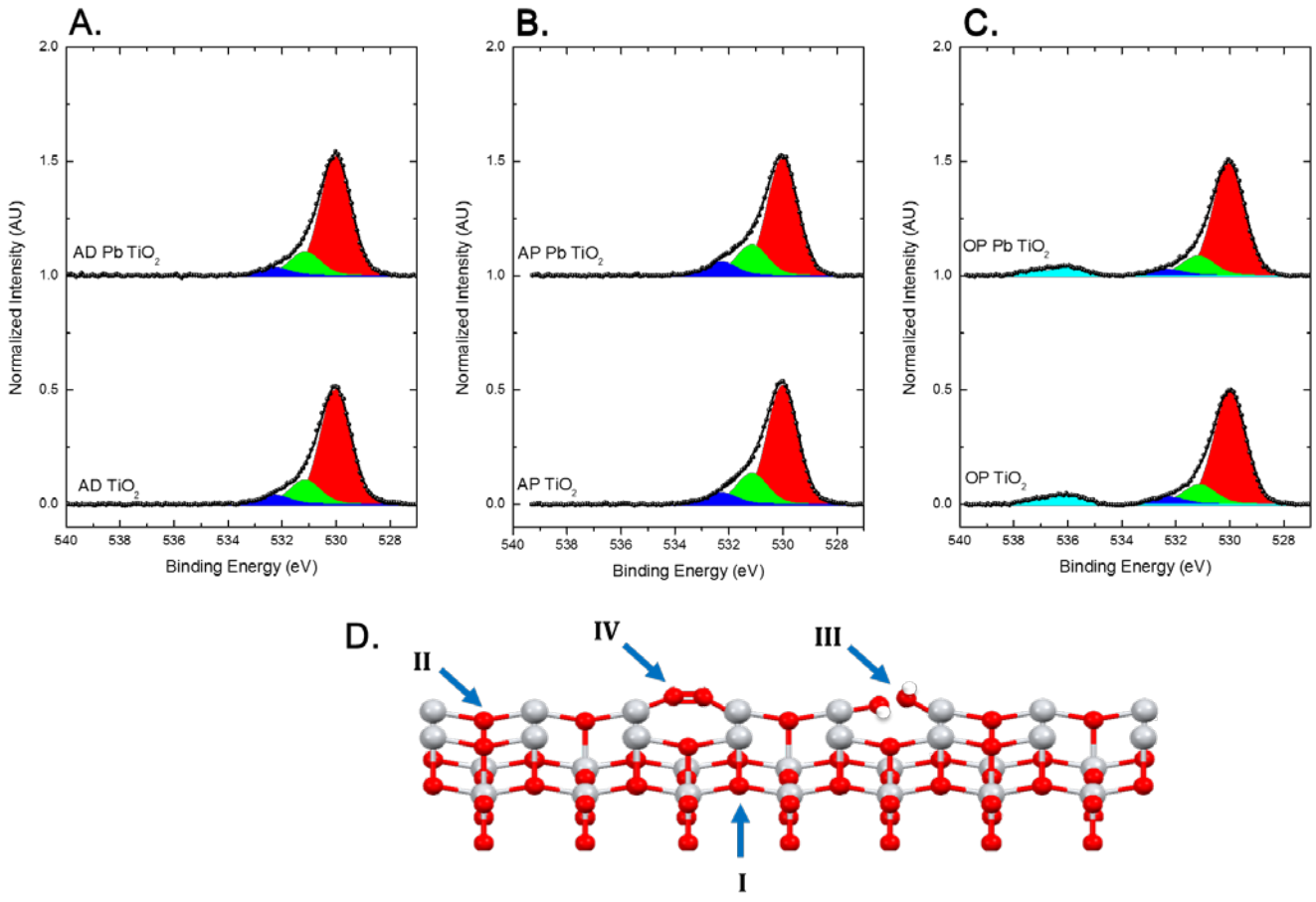

Figure 3.1: High-resolution XPS data for the O 1s region for (A.) AD TiO_2 and AD Pb-TiO_2 (B.) AP TiO_2 and AP Pb-TiO_2, and (C.) OP TiO_2 and OP Pb-TiO_2. The red region indicates lattice oxygen, the green region is bridging oxygen, the blue region is terminal hydroxyl groups, and the cyan region is molecular oxygen adsorbed to TiO_2, which are the species indicated in (D).

was consistently maintained throughout the fitting process. The O 1s lattice peak was normalized to 530.00 eV and all peaks with increasing binding energies were fit with respect

to the lattice peak. The peak area percentages, which indicate the percent area each individual oxygen species occupies within the overall O 1s envelope are shown for all the spectra presented in Figure 3.1. Table 3.1 also shows area percentages of each oxygen species within the O 1s envelope.

AD TiO_2 has an O 1s envelope that is 79.4 ± 1.0% lattice oxygen, 15.4 ± 0.5% bridging oxygen, and 5.2 ± 0.5% oxygen from terminal hydroxyl sources. This finding is consistent with other XPS studies performed on TiO_2 that detected lattice oxygen, bridging oxygen groups, and terminal hydroxyl oxygen species in the near-surface region[12]. This chemical heterogeneity observed within in the O 1s envelope gives rise to the different reactivities of the TiO_2 surface because bridging oxygen groups and terminal hydroxyl groups have different chemical reactivities, where bridging oxygen is capable of donating a proton with a pKa ca. 5 and terminal hydroxyl groups can act as Lewis bases with a pKa of ca. 8. The surface concentration of oxygen on a TiO_2 anatase (101) surface when calculating using the hard sphere volume and unit cell dimensions of a = 3.79 Å, b = 3.79 Å, and c = 9.52 Å is 1.39 x 10^{15} atoms/cm^2, which is then indicative that as-deposited TiO_2 has a bridging oxygen surface concentration of 2.14 x 10^{14} atoms of hydroxyl surface concentration that is ca. 7.23 x 10^{13} hydroxyl groups/cm^2. Thus, the oxygen content of TiO_2 as-deposited by chemical vapor deposition is the largest contributor to the chemical heterogeneity and reactivity of the surface. Relative area ratios (which have the X-ray cross section of the elements accounted for) of the terminal hydroxyl O(t) species and bridging oxygen species O(br) with respect to the lattice oxygen (Table 3.2) give insight to the concentrations of these surface species and can be further evaluated to determine the chemical changes occurring after the TiO_2 substrates are subjected to further treatments.

	O/Ti	O(t)/O(l)	O(br)/O(l)
AD	2.35 ± 0.02	0.07 ± 0.01	0.19 ± 0.01
ADPb	2.35 ± 0.05	0.06 ± 0.00	0.19 ± 0.01
AP	2.51 ± 0.01	0.09 ± 0.00	0.25 ± 0.01
APPb	2.48 ± 0.04	0.09 ± 0.02	0.22 ± 0.03
OP	2.52 ± 0.04	0.07 ± 0.01	0.22 ± 0.01
OPPb	2.53 ± 0.01	0.08 ± 0.01	0.24 ± 0.01

Table 3.2: XPS area ratios. Plus/minus values are calculated by error propagation and n=3.

The Ti 2p spectra are shown in Figure 3.2. The Ti 2p region was used to normalize the other core level data, as the Ti content of the TiO_2 substrates should remain constant even with surface modification. AD TiO_2 has one Ti species, which corresponds to a Ti^{4+} oxidation state based on the Ti $2p_{3/2}$ binding energy at ca. 459 eV[12]. Although we would hypothesize to observe Ti^{3+} species on the surface, as this is the primary dopant of TiO_2 and binds molecular oxygen[72], this species was not detected. A binding energy difference of 71.4 eV between the O 1s lattice peak and the Ti $2p_{3/2}$ peak was observed, which is also consistent with previous XPS studies[12] on TiO_2. The O/Ti ratio and the Ti/O(t) area ratios can be used

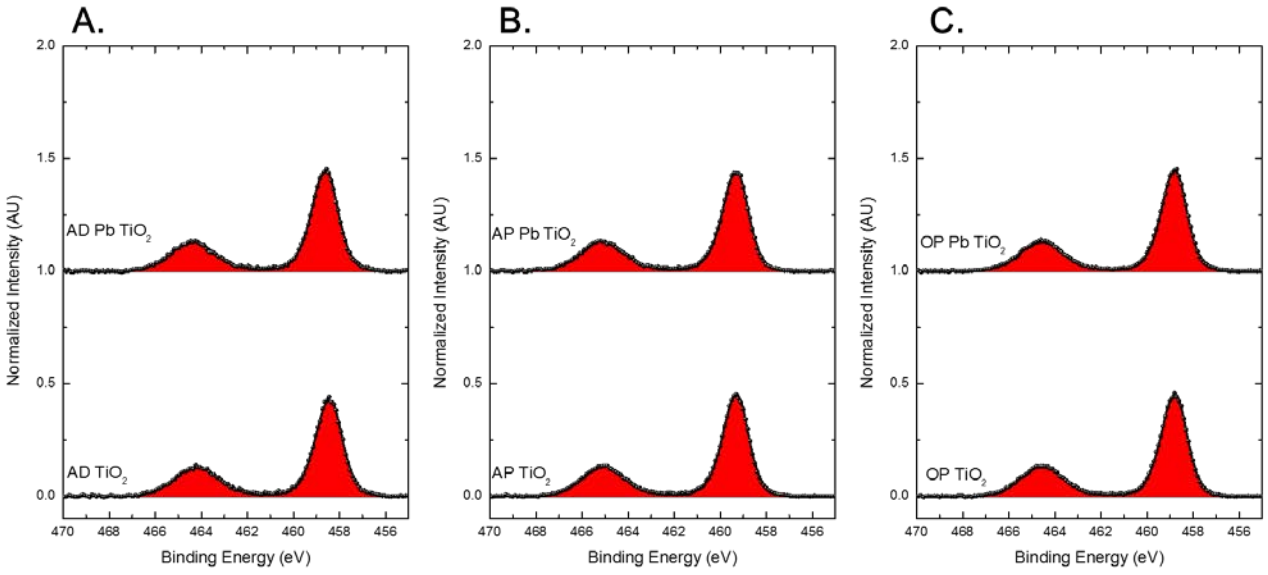

Figure 23.2: Ti 2p core level spectra for (A) AD TiO_2 and AD Pb TiO_2 (B) AP TiO_2 and AP Pb TiO_2 (C) OP TiO_2 and OP Pb TiO_2. All spectra indicate a single Ti species in the Ti^{4+}oxidation state.

to evaluate the relative stoichiometry and the relative amounts of terminal hydroxyl groups, respectively. AD TiO_2 was found to have an O/Ti ratio of 2.35 ± 0.02, indicating that the near-surface region has titanium defects even though these cannot be detected in the Ti 2p core level. The Ti/O(t) ratio was found to be 0.12 ± 0.09, which provides a baseline for comparing the surface chemistry as-deposited TiO_2 to TiO_2 subjected to argon plasma and oxygen plasma.

Device-relevant interfaces, such as the TiO_2/perovskite interface are not prepared in ultrahigh vacuum conditions and are therefore exposed to the ambient atmosphere, i.e. carbonaceous contaminants. Thus, it is important to assess the C 1s spectra (Figure 3.3) to ascertain how the presence of adventitious carbon affects the TiO_2 surface chemistry. Moreover, adventitious carbon adds to interfacial heterogeneity, which can adversely affect the electron-harvesting efficacy of TiO_2 in a device setting. The C 1s spectra of AD TiO_2 is deconvoluted into four peaks: (in order from low to high binding energy) aliphatic carbon,

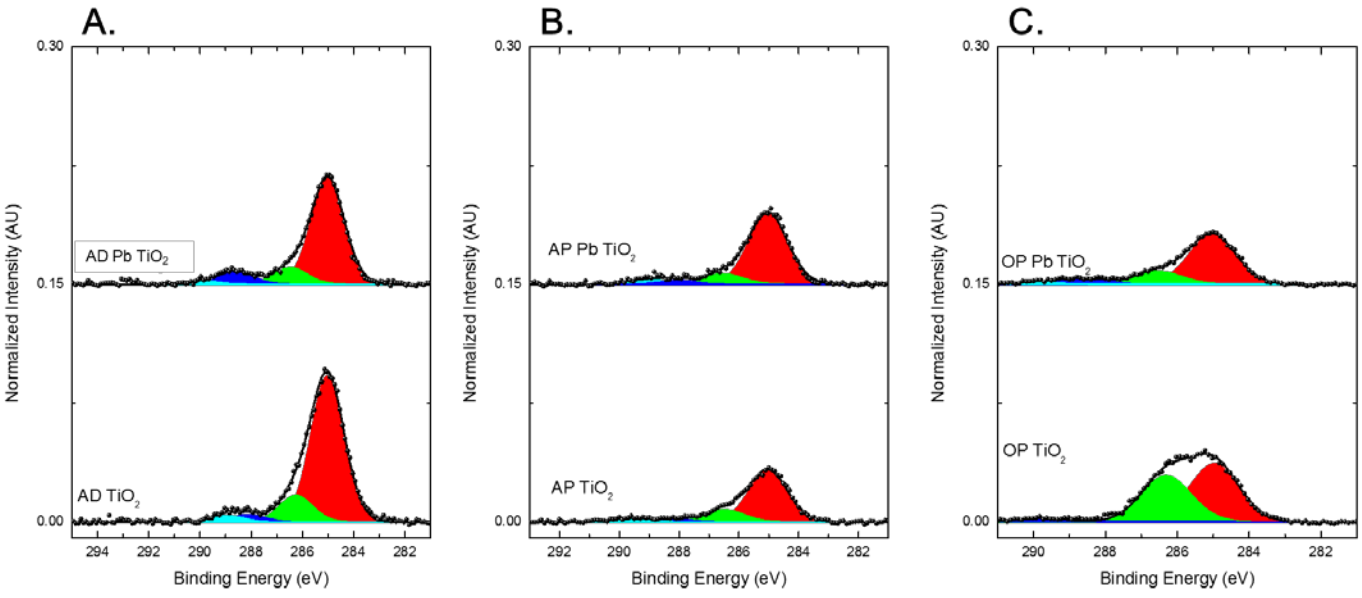

Figure 3.3: C 1s spectra for (A) AD TiO_2 and AD Pb TiO_2 (B) AP TiO_2 and AP Pb TiO_2 (C) OP TiO_2 and OP Pb TiO_2. The deconvolution of the C 1s envelope shows aliphatic carbon in red, R-OH in green, R-COO-R in blue, and R-COOH in cyan.

alcohols (R-OH), esters (R-COO-R), and carboxylic acids (R-COOH)[67]. The atomic concentration of carbon in AD TiO_2 is 30.06 ± 0.54%, with the majority (78.20%) originating from aliphatic sources and the rest of the C 1s envelope originates from oxidized carbon species, which can be either oxidized species from the atmosphere or carbon-containing molecules that are bound to surface oxygen atoms.

In order to characterize more surface-sensitive species, core level spectra were also acquired at a collection angle of 60° with respect to surface normal to provide a qualitative comparison of deconvoluted peak intensities. Changing the collection angle to 60° decreases the sampling depth by half (to ca. 4-5 nm for TiO_2), given by Eq. 3.3, where I is the photoemission intensity at 60°, I_0 is the photoemission intensity at a take-off angle of 0°, z is the sampling depth, λ_N is the IMFP, and ϑ is the take-off angle with respect to surface normal.

$$I = I_0 \exp\left[-\frac{z}{\lambda_N \cos\vartheta}\right] \qquad (3.3)$$

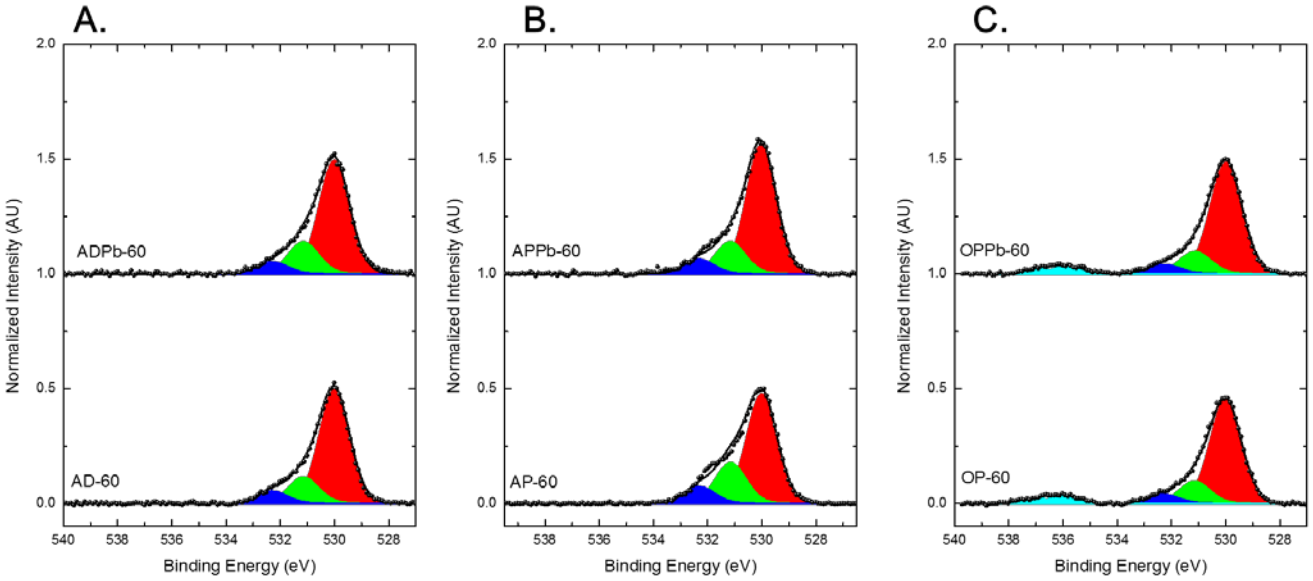

Figure 3.4: Angle-resolved O 1s spectra collected at an angle of 60 degrees with respect to surface normal for (A) AD and AD Pb TiO_2 (B) AP and AP Pb TiO_2 (C) OP and OP Pb TiO_2. The O 1s envelope is deconvoluted into lattice oxygen (red), bridging oxygen (green), terminal hydroxyl groups (blue), and superoxide (cyan).

When comparing the angle-resolved O 1s data of AD TiO_2 (Figure 3.4), we observe an increase in the bridging oxygen species and the terminal hydroxyl species and a decrease in the lattice species compared to the 0° collection angle, which are tabulated in Table 3.1. This finding is expected, as the bridging oxygen atoms and terminal hydroxyl groups are found on the TiO_2 surface rather than the bulk. Ti 2p data collected at 60° shows no significant changes in the binding energy, nor the chemical composition, which is indicative of no changes in the Ti species on the surface compared with the 0° w.r.t. surface normal. Additionally, the O/Ti ratio remains the same as the 0° data, which indicates no stoichiometric changes with the change in sampling depth. As expected, C 1s intensity and overall atomic concentration increased with the increased collection angle, as the carbonaceous species originate as a contaminate overlayer. Thus, the angle-resolved data confirm qualitatively that bridging oxygen and hydroxyl species exist primarily at the surface and that the carbonaceous overlayer is on top of the surface rather than integrated within

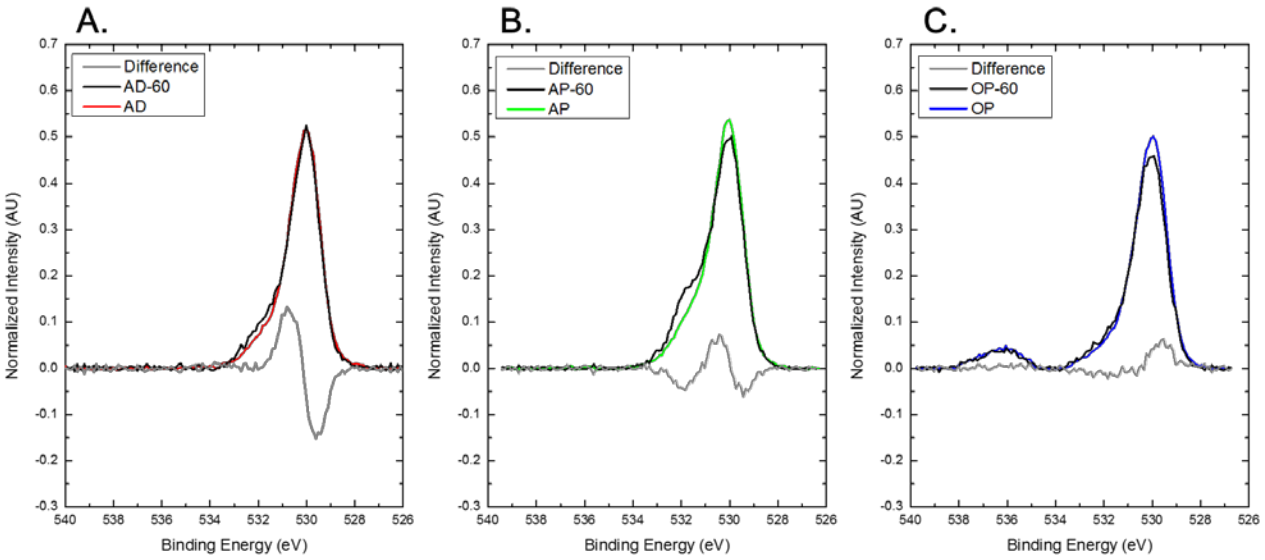

Figure 3.5: O 1s difference spectra showing the bare substrates (A) AD TiO_2 (B) AP TiO_2 and (C) OP TiO_2 in comparison with the angle-resolved data.

the bulk of the film. To further assess the difference between the collection angles, O 1s difference spectra are plotted in Figure 3.5, which also indicate a decrease in the lattice species and the increase in bridging oxygen and hydroxyl species. Overall, the surface of AD TiO_2 prepared by CVD contains titanium bound to both bridging oxygen and hydroxyl groups that are concentrated at the surface with a carbonaceous overlayer resulting from atmospheric exposure and a relatively high deposition pressure.

Argon plasma treatment involves the bombardment of the TiO_2 surface with argon atoms for the purpose of removing carbonaceous contaminants from the surface, exposing the reactive TiO_2 surface. The O 1s region can be found in Figure 3.1. AP TiO_2, like AD TiO_2, contains three oxygen species, including oxygen originating from the lattice, bridging oxygen groups, and terminal hydroxyl groups. Deconvoluting the O 1s envelope yields 74.6±0.5% lattice oxygen, 18.7±0.4% bridging oxygen, and 6.7±0.2% terminal hydroxyl groups. This deconvolution indicates a decrease in the relative lattice oxygen species and an increase in the detected surface species, relative to AD TiO_2. Therefore, argon plasma treatment increases the relative concentration of reactive surface oxygen species compared to AD TiO_2 without drastically altering the chemical composition.

The Ti 2p region of AP TiO_2 (Fig. 3.2) also did not indicate that argon plasma treatment induces any major change to the surface chemistry. Like AD TiO_2, the Ti 2p region measured for AP TiO_2 also shows that there is one Ti species in the Ti^{4+} oxidation state, based on the binding energy of the Ti $2p_{3/2}$ peak at ca. 459 eV. However, changes occur in the surface stoichiometry when evaluating the O/Ti ratios tabulated in Table 3.2. Compared to AD TiO_2, we observe the film become overall more defective in the near-surface region,

shown by an increase in the O/Ti ratio from 2.35±0.02 to 2.51±0.01, yet the O(lat)/Ti ratio remains the same for both AD and AP TiO_2. Moreover, AP TiO_2 overall has more bridging oxygen and hydroxyl groups on the surface than AD TiO_2, given by the increased O(t)/O(lat) and O(br)/O(lat) ratios. Thus, argon plasma treatment has not altered the Ti composition of the film, but has increased the amount of oxygen surface species, i.e. bridging and hydroxyl oxygens.

Another effect argon plasma treatment has on AD TiO_2 is the overall reduction of the carbonaceous contaminant layer on the surface, as seen in the C 1s spectrum in Figure 3.3. AP TiO_2 shows from the quant. report that the average atomic concentration of carbon on the surface is 13.99±0.48% compared to 30.06±0.54% for AD TiO_2. Additionally, the removal of carbonaceous species on the surface appears to be relatively non-discriminant toward the different types of carbon species, e.g. atomic percentages of the aliphatic, R-OH, R-COO-R, and R-COOH regions remain in similar proportions with respect to the C 1s spectrum of AD TiO_2, while decreasing the overall atomic percentage of carbon. Thus, the carbon content AP TiO_2 retains similar surface chemistry to that of AD TiO_2, while reducing the overall quantity of carbonaceous contaminants on the surface.

Additionally, angle-resolved data at 60° were collected for AP TiO_2 in order to qualitatively compare the core level spectra to the spectra collected at a 0° and the AD TiO_2 core levels. Difference spectra allow us to ascertain which species are closer to the top of the film, as the 60° collection angle is more surface-sensitive. As shown in Table 3.1, there is a decrease in the lattice oxygen atomic percent and an increase in the bridging oxygen and hydroxyl regions, similar to AD TiO_2. Thus, we can confirm that the oxygen species on the

surface of AP TiO_2 are like that of AD TiO_2, but with a greater concentration of bridging oxygens and terminal hydroxyls. Similar to AD TiO_2, the Ti 2p region of AP TiO_2 collected at 60° did not show any significant changes within the Ti 2p envelope, i.e. the Ti species detected toward the top of the film show no indication of compositional deviations from Ti^{4+} species in the TiO_2 lattice. With the angle-resolved data, we observe a slight increase in the O/Ti ratio from 2.51 to 2.60, which is consistent with the detected increase in the hydroxyl and bridging oxygen species. Additionally, we observe an increase in the atomic concentration of carbon with a decreased probe depth, which occurs as expected. The O 1s difference spectrum showing the 60° collection angle subtracted from the 0° collection angle (Fig. 3.4) further highlights the slight compositional changes observed at the different probe depths, which demonstrate an increase in the surface bridging oxygens and hydroxyl groups. When holistically comparing the surface chemistry of AD TiO_2 versus AP TiO_2, both species have bridging oxygen and hydroxyl groups on the surface with AP TiO_2 having a higher concentration of these surface species than AD TiO_2, as indicated by the greater O/Ti ratio. Both films have Ti^{4+} as the only detected Ti species, and therefore argon plasma does not seem to impact Ti species. Lastly, argon plasma treatment has the primary effect of removing part of the carbonaceous overlayer resulting from atmospheric exposure while maintaining similar surface chemistry to the as-deposited film.

As-deposited TiO_2 films were also treated with oxygen plasma, a common step in the fabrication of photovoltaic devices[54], and then analyzed using X-ray photoelectron spectroscopy in order to ascertain the effect that oxygen plasma has on the surface chemistry of AD TiO_2 compared to that of AP TiO_2. The O 1s spectrum of OP TiO_2 (Fig. 3.1) introduces a new oxygen species into the O 1s envelope at a binding energy of ca. 536 eV, which has been

identified as a superoxide species that spectroscopically appears as a doublet, resulting from the paramagnetic nature of oxygen. Diebold and colleagues[72] have also observed this species on TiO_2 by XPS and assert that this species binds to undercoordinated Ti_{5C} sites, thus saturating the surface with oxygen. This superoxide species only appears after oxygen plasma cleaning and appears to be a significant chemical change to the surface chemistry of TiO_2. Moreover, the presence of this species suggests that although they are not detected by XPS, there are undercoordinated Ti_{5C} sites present on the surface and the binding of this superoxide species contributes to a de-doping of the surface by coordinating to these sites on the surface. The superoxide doublet accounts for 2.58±0.34% of the atomic composition of the film, which is a significant contribution to the surface chemistry. Introduction of this superoxide species does alter the distribution of oxygen species within the O 1s envelope. When compared to AD TiO_2, OP TiO_2 shows a decreased percentage of lattice oxygen (Table 3.1) yet contains comparable amounts of both bridging oxygen and hydroxyl groups. In comparison to AP TiO_2, OP TiO_2 has a lower concentration of surface bridging oxygen and hydroxyl groups: the surface chemistry is more akin to AD TiO_2 with the addition of superoxide and a rearrangement of oxygen species throughout the film.

Much like AD and AP TiO_2, the Ti 2p region of OP TiO_2 (Fig. 3.2) indicates that there is one Ti species on the surface corresponding to Ti^{4+}, based on the binding energy of the Ti $2p_{3/2}$ peak at ca. 459 eV. However, changes occur in the surface stoichiometry when evaluating the O/Ti ratios tabulated in Table 3.2. Compared to AD TiO_2, we observe an increase in the O/Ti ratio from 2.35±0.02 to 2.52±0.04; however, the O(lat)/Ti ratio sees a slight decrease, increasing that the oxygen plasma treatment process results in a reorganization of the oxygen species in the lattice. Further support of this reorganization is

seen as an increase in the O(t)/Ti ratio when compared to AD TiO_2, which is indicative that more surface species are being revealed during the plasma etching process. Interestingly, AP TiO_2 and OP TiO_2 have the same O/Ti ratio, indicating that the carbonaceous overlayer likely obscures the proper measurement of the surface oxygen species. Additionally, the O(br)/Ti ratio of OP TiO_2 slightly increases with respect to the bare substrate. Overall, the Ti composition of the TiO_2 film has not been altered drastically by oxygen plasma cleaning.

The C 1s spectrum of OP TiO_2 is shown in Figure 3.3. Interestingly, the deconvolution of the C 1s spectrum indicates a lack of oxidized carbon species and the major contributors to the envelope are aliphatic carbon and R-OH groups, which is consistent with the mechanism by which oxygen plasma removes carbonaceous species from the surface. This observation is in contrast to the C 1s spectra of AD and AP TiO_2, which both have oxidized carbon species on the surface, with AP TiO_2 having an overall reduction of carbon species via the argon plasma treatment. In this particular measurement, the atomic percent of carbon is larger than usual (see Appendix A); however, in typical XPS measurements of OP TiO_2, the carbon content is approximately equal to the carbon content of AP TiO_2, which is ca. 11%.

Upon examination of the angle-resolved spectra, we observe changes in the O 1s spectrum characterized by an overall decrease in the concentration of the lattice oxygen, which is consistent for what was seen with AD TiO_2 and AP TiO_2 collected at 60° with respect to surface normal. Additionally, angle-resolved data further confirmed that the bridging oxygen and hydroxyl groups show increased area percentage with an increased collection angle (Table 3.1). Interestingly, the superoxide species does not show significant changes with the changed collection angle, indicating that the superoxide species is not a surface-

sensitive oxygen species, which is clearly seen in the O 1s difference spectra in Figure 3.4. Thus, oxygen plasma treatment acts to remove surface carbon species while depositing this superoxide species throughout the near-surface region of the film. As with the other bare TiO_2 films, the Ti 2p spectra collected do not show any differences in the chemical composition, i.e. any different Ti oxidation states with the increased collection angle, indicating consistent Ti composition throughout the near-surface region. Additionally, we observe an increase in the overall atomic concentration of carbon, which, as for the AD and AP TiO_2 is expected because the carbon species are on the top layer of the film, which occurs as expected. When comparing the surface chemistry of AD TiO_2 with TiO_2 that has been argon plasma and oxygen plasma treated, we observe a general reduction in the carbonaceous overlayer that covers the surface. Controlling this contaminant layer is important at the device level, as contaminants that introduce interfacial heterogeneity can adversely impact the charge collection efficacy.

Argon plasma affects the surface chemistry by facilitating the removal of carbon and exposes the bridging oxygen and terminal hydroxyl groups located on the surface. Thus, this treatment method is most ideal for removal of adventitious carbon, while retaining the surface species of the as-deposited film in higher concentrations. Moreover, the increased concentration of oxygen species of this surface makes it subject to oxidation processes, which decreases the work function of the surface (Appendix A): low work function contacts are ideal for electron-selective interlayers, as high work function materials can introduce undesirable charge injection barriers depending on the energetics of the active layer[83]. In contrast, oxygen plasma cleaning introduces a superoxide species to the film that has been shown by angle-resolved XPS to be distributed throughout the film. The O/Ti ratio of AP and

OP TiO_2 remain the same; however, the distribution of oxygen species on the OP surface revealed by deconvolution indicate that the reactive hydroxyl species on the surface are at a lower concentration than the AP surface. Thus, the OP surface is not as electron-rich as the AP surface, making the work function of the surface increase (Appendix A). Therefore, devices made utilizing a Cs-pvsk active layer and TiO_2 as an electron-selective interlayer would benefit from use of argon plasma rather than oxygen plasma in the removal of carbonaceous species on the TiO_2 surface.

3.2 Examining the Impact of Lead Adsorption on the Surface Chemistry of TiO_2

In addition to the electronic effects, the surface chemistry after plasma cleaning is a primary concern at the TiO_2/perovskite interface, as it is non-inert. We hypothesize that the perovskite precursor solution containing PbI_2 and CsBr in solution contain ions that bind to the reactive hydroxyl species on the TiO_2 surface. In this experiment, bare TiO_2 substrates were subjected to a lead adsorption from DMF solution at a concentration of 56 mM (3 mg/mL) for two hours at 70°C with the intent of saturating the surface with lead cations with one full monolayer of Pb^{2+} on TiO_2 having a surface coverage of 9.18×10^{-11} mol/cm^2 when calculated under the assumption that each TiO_2 anatase unit cell has one hydroxyl group[74] and assuming that Pb^{2+} binds as a bidentate ligand to TiO_2. The resulting surface composition was determined by XPS and compared to the bare substrate surface chemistry. An additional comparison was done with thin films of PbI_2 that were spin-coated using the same solution used for the lead adsorption experiment.

The O 1s spectra for the lead treated as-deposited TiO_2 (AD Pb TiO_2) is shown in Figure 3.1. Like the O 1s spectra for AD TiO_2, this O 1s spectrum is also deconvoluted into

three components, which still indicate lattice oxygen (80.2 ± 0.8%), bridging oxygen (15.0 ± 0.5%), and terminal hydroxyl groups (4.7 ± 0.3%). In comparison to AD TiO_2 (Table 3.1), the AD Pb TiO_2 surface has similar composition within a standard deviation of lattice oxygen and bridging oxygen, but has a lower amount of terminal hydroxyl oxygen detected that is one standard deviation away, suggesting that terminal hydroxyl oxygen detected is changing when lead cations are on the surface. Studies examining the mechanism of lead binding to TiO_2 have proposed that lead cations bind to hydroxyl groups on the surface[23] and the results here would suggest that there is an attenuation of photoelectron signal from hydroxyl groups once they are bound to Pb^{2+} that is hypothesized to arise from increased scattering from the presence of Pb atoms. It is worth nothing that the fitting parameters in the O 1s spectra for the lead-adsorbed substrates do not include an additional peak for a Pb-O bond. A study done by Shallcross and colleagues[54] show that the binding energy for Pb-O obtained from an oxidized lead foil sample has a binding energy of 529.5 eV and Pb-OH having a binding energy of 531.5 eV. The binding energy of Pb-O is 1.1 eV lower in binding energy than the TiO_2 lattice and the binding energy of Pb-OH is just 0.1 eV lower than the TiO_2 lattice. Essentially, the photoemission signal originating from the terminal hydroxyl groups in the near-surface region attenuates as a result of the shift in the local electronic environment shift toward the O 1s lattice peak. The resolution of the spectrometer is not high enough to distinguish the Pb-OH peak and the Pb-O peak appears in the low-binding energy shoulder of the lattice oxygen peak. The amount of lead adsorbed on to TiO_2 is not at a high enough coverage to introduce a peak with an acceptable level of confidence (i.e. >95%) and therefore, these peaks have been omitted from the deconvolution of the O 1s envelope. For the three oxygen species that comprise the O 1s envelope, the O/Ti, O(t)/O(l), and the O(br)/O(l) ratios

remain the same as they are for AD TiO_2 (Table 3.2), which indicate that the deposition of lead ions does not alter the underlying substrate chemistry aside from the Pb^{2+} binding event. Overall, very minor changes were observed in the O 1s envelope upon lead adsorption.

The Ti 2p region (Figure 3.2) of AD Pb TiO_2 indicates that there is a single Ti^{4+} species based on the binding energy of the Ti $2p_{3/2}$ peak at ca. 459 eV. Additionally, the surface stoichiometry when evaluating the O/Ti ratios tabulated in Table 3.2. do not change within a standard deviation compared to AD TiO_2, indicating that the Ti composition does not undergo any significant changes. Compared to the bare substrate, there is an apparent increase in the overall atomic concentration of Ti, yet the O/Ti ratio remains the same. This observation is a result of a decrease in the carbonaceous overlayer facilitated by the rinsing steps following the lead adsorption process. The physisorbed overlayer has a stronger affinity to the organic solvents, DMF and isopropanol compared to the TiO_2, which leaves behind the lead ions and some carbon species remain.

The C 1s region (Figure 3.3) also provides insight into the lead adsorption process. Like the C 1s spectrum of AD TiO_2, the C 1s envelope of AD Pb TiO_2 is deconvoluted into four peaks: (in order from low to high binding energy) aliphatic carbon, alcohols (R-OH), esters (R-COO-R), and carboxylic acids (R-COOH)[67]. The atomic concentration of carbon decreased from 30.06 ± 0.54% (AD TiO_2) to 22.84 ± 0.46%, which accounts for a loss of carbonaceous species from the rinsing process after lead adsorption. In the AD Pb TiO_2 deconvolution, there are not significant alterations in the peak area percentages for the aliphatic regions, but there appears to be more oxidized carbonaceous species on the surface, likely originating from the solvents, isopropanol and DMF.

Lead adsorption was done from a solution of PbI_2 in DMF and the I 3d signal was measured (Figure 3.4). Interestingly, the I 3d signal was absent from all lead adsorbed substrates, thus indicating that during the lead adsorption process, iodine must leave the system, either as iodide anions stabilized by the solvent that are then washed away during the rinsing process, or iodine leaves as HI upon reacting with the surface, as shown below.

$$2\ (\text{-OH})_{\text{surface}} + Pb^{2+} + 2\ I^{-} \rightarrow 2\ HI + (\text{O-Pb-O})_{\text{surface}}$$

Scheme 3.1: surface equilibrium reaction of lead iodide with surface species on TiO_2

This equilibrium process that occurs between lead iodide and the TiO_2 surface offers insight into how an integral component of the perovskite precursor solution interacts with the TiO_2 surface in solution and therefore how the initial nucleation of the perovskite layer begins on the TiO_2 surface. The Pb^{2+} ion is in equilibrium with PbI_2 when dissolved in solution. Iodide ions are proton acceptors and thus, an ion-exchange reaction occurs with the TiO_2 surface.

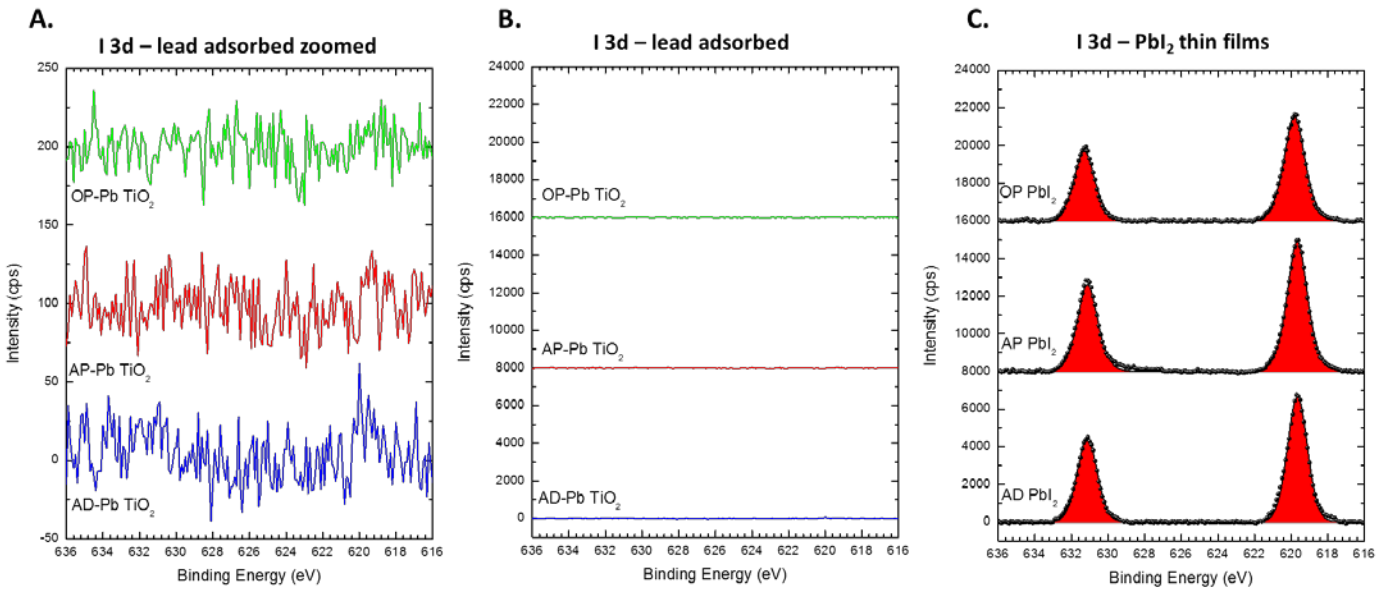

Figure 3.4: I 3d signal for (A) the lead adsorbed substrates, AD Pb TiO_2, AP Pb TiO_2, and OP Pb TiO_2. (B) The same I 3d signal as A., but on the same scale as (C.) the I 3d signal originating from thin films of PbI_2 on AD TiO_2, AP TiO_2, and OP TiO_2.

Furthermore, the lack of iodine observed by XPS on the surface is consistent with other findings[75] that assert that binding mechanism for lead to TiO_2 involves the capture of lead by

hydroxyl groups, which is consistent with data revealed in the O 1s spectrum and preserves electroneutrality. Additionally, Sargent and colleagues have reported[76] that halogens can bind to Ti_{5C} sites, but the ionic radius of iodide compared to chloride for example is 140 pm versus 100 pm and the absence of the I 3d signal indicates that the iodide anion is likely too large to bind to any exposed Ti_{5C} sites on the TiO_2 surface. Thus, halogen reactivity to the surface must also be considered when considering the interfacial chemistry between TiO_2 and perovskite in addition to the concentration of Ti_{5C} sites.

The Pb 4f core level (Figure 3.5) was also measured in order to quantify the lead deposited on the surface from the lead adsorption process. The Pb $4f_{7/2}$ peak of AD Pb TiO_2 has a binding energy of ca. 139 eV, which is a shift of ca. 0.5 eV higher binding energy with respect to the thin PbI_2 films. The binding energy shift is indicative that there is a change in the local electronic environment of the lead ions on the surface of TiO_2 compared to PbI_2 to a more electron-withdrawing coordination environment. The binding energy of the lead on

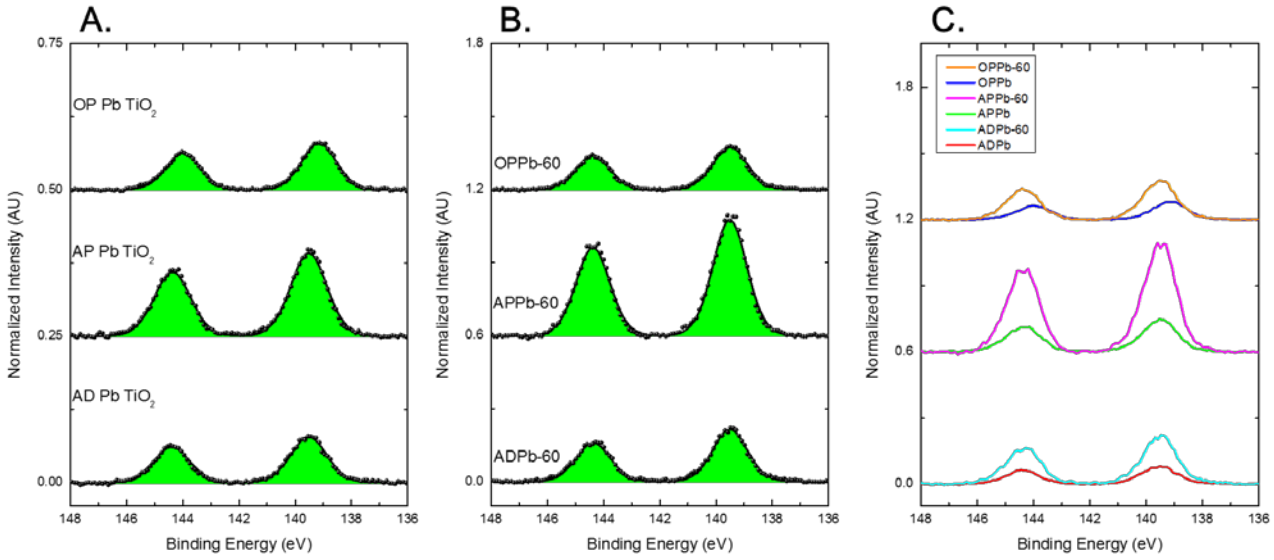

Figure 3.5: Pb 4f spectra at (A) normal collection angle (B) at 60 degrees with respect to the surface and (C) both angles collected and plotted on the same scale. The increased intensity in the angle-resolved data indicates that the Pb detected is toward the top of the TiO_2 film

TiO_2 has a binding energy similar to $PbTiO_3$, which has the Pb $4f_{7/2}$ binding energy at 139.0 eV[77] and a similar coordination environment as Pb on TiO_2. The atomic percentage of Pb on the AD Pb TiO_2 surface is 1.49 ± 0.34%, which is equivalent to a surface coverage of 3.44 x 10^{-11} mol/cm^2, or 37% of a monolayer. This result is representative of a relatively low surface coverage considering that the lead ions were deposited from a solution in the millimolar regime. However, the low surface coverage of Pb^{2+} likely arises from a required two adjacent hydroxyl groups to bind lead. Thus, the data presented in the rest of this chapter aims to highlight the effects of having neighboring hydroxyl groups bound to lead (lead adsorbed substrates) compared to TiO_2 with free adjacent hydroxyls (bare substrates) that are capable of participating in chemical reactions with the perovskite layer upon deposition.

Angle-resolved data collected at 60° w.r.t. surface normal (Figure 3.6) provides information on which species are surface-sensitive comparison to the 90° collection angle. The O 1s-60 spectrum of AD Pb TiO_2, similar to the O 1s-60 spectra of the bare substrates,

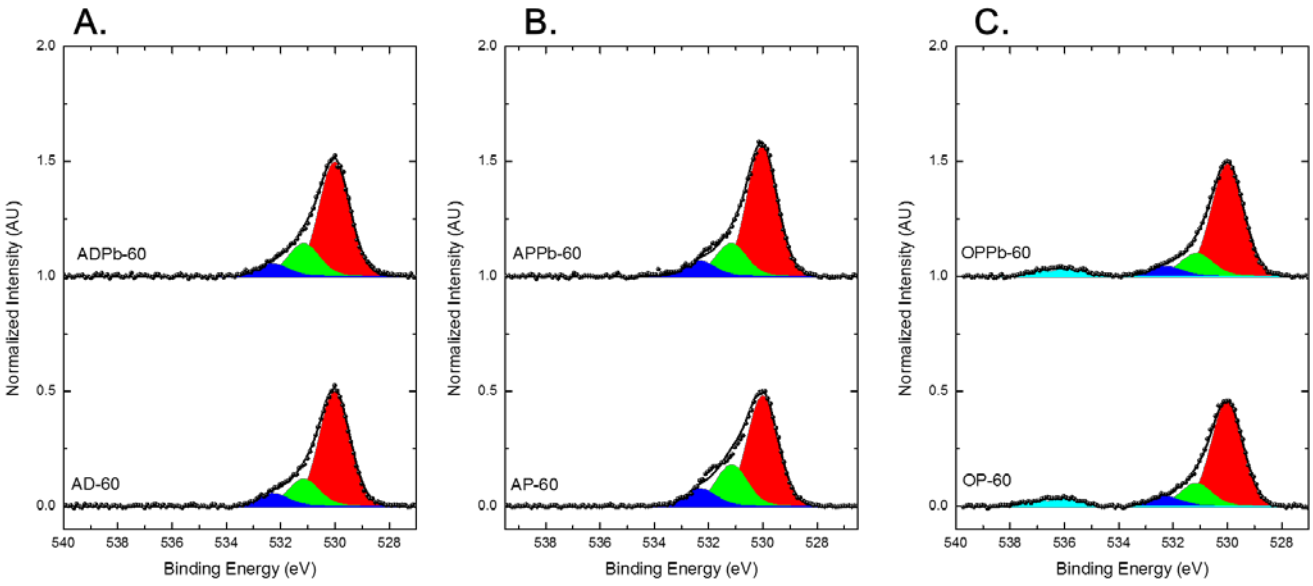

Figure 3.6: O 1s spectra collected at 60 degrees for (A) AD TiO_2 and AD Pb TiO_2 (B) AP TiO_2 and AP Pb TiO_2 (C) OP TiO_2 and OP Pb TiO_2 where the red region is lattice oxygen, green is bridging oxygen, blue is terminal hydroxyls and cyan is superoxide.

shows an increase in the bridging oxygen region from 15.0% of the envelope to 20.3% and the terminal hydroxyl region increased from 4.7% to 7.6%, which is similar to the increases observed for the AD-60 samples, indicating that the bridging and terminal hydroxyl groups are on the TiO_2 surface when looking at the surface species binding energies around 532 eV. Similarly, there was no significant change observed in the Ti 2p angle-resolved data (Figure 3.7), as the Ti^{4+} species are part of the bulk of the film rather than surface-specific species.

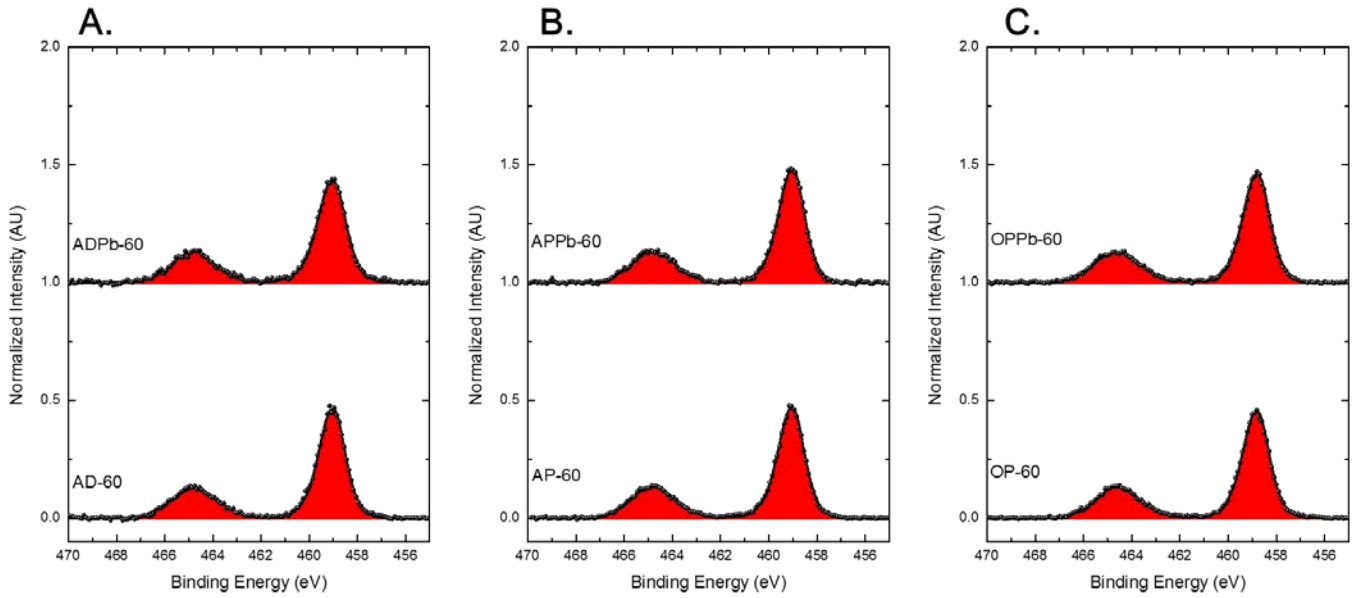

Figure 3.7: Angle-resolved Ti 2p spectra collected at 60 degrees for (A) AD TiO_2 and AD Pb TiO_2 (B) AP TiO_2 and AP Pb TiO_2 (C) OP TiO_2 and OP Pb TiO_2. The Ti 2p spectra are composed of signal originating from a Ti^{4+} species.

The overall O/Ti ratio decreases to 0.83 resulting from the reduced detection of the oxygen that is part of the bulk lattice, as this is the primary contributor comprising ca. 72% of the O 1s envelope. An increase was seen in the atomic percent of the C 1s region (Figure 3.8) from 22.84% to 39.65%, which is expected, as the carbonaceous overlayer deposits from the atmosphere; however, there were no significant deviations in the deconvolution of the C 1s spectrum, thus indicating that the carbon species are surface-sensitive. A revealing aspect of the angle-resolved data is the Pb 4f spectrum (Figure 3.9), wherein an atomic percentage

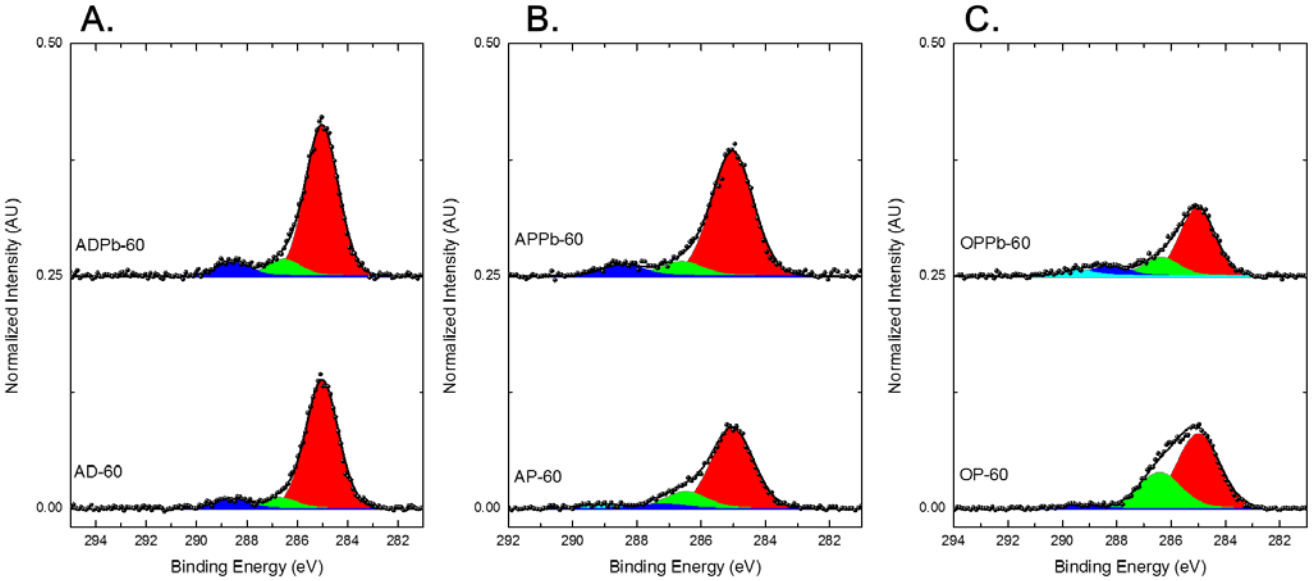

Figure 3.8: Angle-resolved C 1s spectra collected at 60 degrees with respect to the surface for (A) AD and AD Pb TiO_2 (B) AP and AP Pb TiO_2 (C) OP and OP Pb TiO_2. The red region is aliphatic carbon, green is R-OH, blue is R-OOR, and cyan is R-COOH

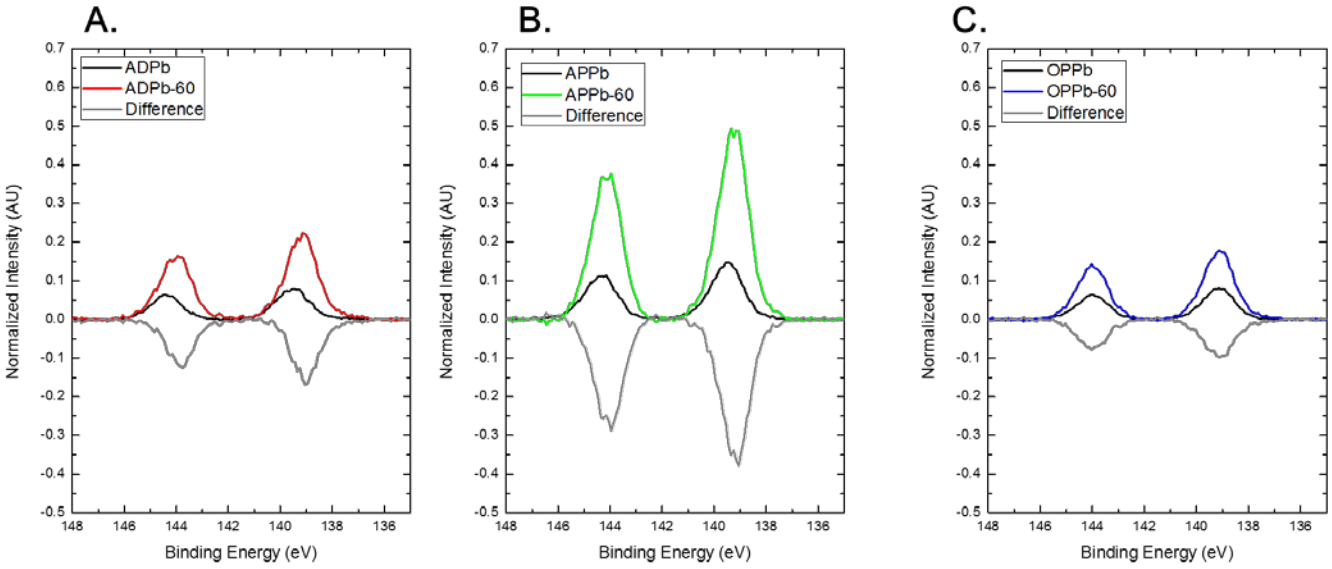

Figure 3.9: Pb 4f difference spectra showing the 60-degree collection angle subtracted from the normal collection angle for (A) AD Pb TiO_2 (B) AP Pb TiO_2 (C) OP Pb TiO_2. The greater intensity shown with the 60-degree spectra indicate that the Pb signal on the TiO_2 film is depth-dependent and that the Pb cations reside toward the top of the film.

increase from 1.49% to 2.60% is observed, which indicates that there are more Pb species within the top ca. 4 nm of the film. These data indicate that the binding site of the Pb species is highly specific to the chemical species found within the first 4 nm of the TiO_2 film, which

supports hypotheses discussed in the literature that Pb binds to terminal hydroxyl groups on the TiO_2 surface[23]. Thus, angle-resolved data indicates that the Pb cations are surface-bound to species specific to the top 4.5 nm of the TiO_2 surface, which is supported by previously done studies[23] indicating that TiO_2 binds to terminal hydroxyl groups.

Argon-plasma treated TiO_2 was also subjected to the lead adsorption process (AP Pb TiO_2) and compared to both AP TiO_2 and AD Pb TiO_2 in order to elucidate the effect that the initial surface treatment has on the lead adsorption process. The O 1s spectrum of AP Pb TiO_2 (Fig. 3.1) is deconvoluted into three peaks, which are (from low BE to high BE) lattice oxygen (76.7 ± 2.8%), bridging oxygen (16.7 ± 1.6%), and terminal hydroxyl groups (6.6 ± 1.3). When compared to the O 1s spectrum of AP TiO_2, the Pb-treated surface has an approximately similar concentration of lattice oxygen and terminal hydroxyl detected but has a slightly decreased concentration of bridging oxygen groups. This observation is likely linked to an increased amount of carbon on the surface and the lead atoms that are now present that can scatter the signal. In comparison to AD Pb TiO_2, the O 1s envelope of AP Pb TiO_2 shows reduced atomic percentages of lattice oxygen, but increased amounts of bridging oxygen and terminal hydroxyls, which is consistent with the findings of the bare substrates that were not treated with lead (AD and AP TiO_2). However, AP Pb TiO_2 has a greater O/Ti ratio than AD Pb TiO_2 (2.48 ± 0.04 versus 2.35 ± 0.05, respectively), resulting from a lesser amount of surface carbon.

The Ti 2p region (Figure 3.2) of AP Pb TiO_2 shows the Ti $2p_{3/2}$ peak at ca. 459 eV. The envelope is comprised of a single Ti^{4+} species. The surface stoichiometry indicated by the O/Ti ratio does increase resulting from a reduced amount of surface carbon. In comparison to AP TiO_2, the O/Ti ratio, O(t)/O(l), and O(br)/O(l) remains relatively the same within a

standard deviation, thus indicating that the lead adsorption process does not significantly change the stoichiometry detected by XPS. Compared to AD Pb TiO_2, the O/Ti ratio increases from 2.35 ± 0.05 to 2.48 ± 0.04, which indicates that even though there is more carbon on the surface from the post-deposition rinsing process, there are still more exposed surface oxygen species when argon-plasma treated versus the as-deposited substrate.

The C 1s spectrum (Figure 3.3) envelope of AP Pb TiO_2 is deconvoluted into four peaks: (in order from low to high binding energy) aliphatic carbon, alcohols (R-OH), esters (R-COO-R), and carboxylic acids (R-COOH)[67], consistent with the C 1s spectra of AD TiO_2, AP TiO_2, and AD Pb TiO_2. In comparison to AP TiO_2, the atomic concentration of carbon slightly increased from 13.99 ± 0.48% (AP TiO_2) to 15.60 ± 0.66%, which accounts for an increase in carbonaceous species from the rinsing process after lead adsorption. In the AP Pb TiO_2 deconvolution, the aliphatic region is slightly increased and the oxidized carbon species overall slightly decreased likely from longer atmospheric exposure, but the ester peak slightly increased. Since this substrate was subjected to plasma cleaning prior to the lead adsorption process, the result is likely from new oxygen species that are chemically bound to the surface, as the physisorbed material was removed during the rinsing process.

The Pb 4f core level (Figure 3.5) was also measured for AP Pb TiO_2 in order to quantify the lead deposited on the surface from the lead adsorption process when the bare substrate is subjected to argon plasma treatment prior to deposition. Like AD Pb TiO_2, the Pb $4f_{7/2}$ peak of AP Pb TiO_2 has a binding energy of ca. 139 eV, which is a shift of ca. 0.5 eV higher binding energy with respect to the thin PbI_2 films, indicating a change in the local electronic environment of the lead ions on the surface of TiO_2 compared to PbI_2 to a more electron-withdrawing coordination environment. The binding energy of the lead on TiO_2 has a binding

energy similar to $PbTiO_3$, which has the Pb $4f_{7/2}$ binding energy at 139.0 eV[77] and a similar coordination environment as Pb on TiO_2. The atomic percentage of Pb on the AP Pb TiO_2 surface is 2.69 ± 0.16%, which is equivalent to a surface coverage of 6.21 x 10^{-11} mol/cm^2, or 68% of a monolayer. Compared to AD Pb TiO_2, this is a significant increase in surface coverage from 37% of a monolayer. The increased lead concentration on argon-plasma treated TiO_2 originates from the greater concentration in terminal hydroxyl groups and bridging oxygens that can become hydroxyl groups upon reaction when argon-plasma treated. Moreover, argon plasma treatment helps to reduce the carbonaceous overlayer, which contains species that can occupy possible reactive sites to which Pb can bind.

As with the other substrates, angle-resolved data was collected to qualitatively determine which species reside closer to the top of the film. The O 1s-60 spectrum (Figure 3.6) of AP Pb TiO_2 has the envelope deconvoluted into three regions with O(l) representing 73.5%, O(br) representing 18.2%, and O(t) representing 8.3%. Compared to AP TiO_2, AP Pb TiO_2 shows an increase in the lattice oxygen, and decreased concentrations of bridging oxygen and terminal hydroxyl groups. Since the Pb cations are binding to these surface-bound species, this is a reasonable result compared to that of AD Pb TiO_2 because the carbonaceous overlayer obfuscates quantitation. As with the other substrate measurements, no significant changes were observed in the Ti 2p angle-resolved data (Figure 3.7). When evaluating the O/Ti ratios, we also do not observe any significant changes beyond a widening of the standard deviation, which indicates an increase in compositional heterogeneity originating from the lead now being on the surface and scattering some of the O 1s signal. As with previous angle-resolved data discussed, there is an increase in the atomic percent of carbon (Figure 3.8) from 15.60% to 32.51% without any significant deviations in the atomic

percentages of the deconvoluted envelope that resides on the top layer of the TiO_2 surface. Like the Pb 4f spectrum for AD Pb TiO_2, AP Pb TiO_2 shows an increase (Figure 3.5) in the atomic percentage of Pb on the surface from 2.69% to 5.44%, which is representative of a nearly doubled increase in the atomic concentration of Pb, similar to what was observed for AD Pb TiO_2. This observation further confirms the location of the Pb cations on the TiO_2 surface to be bound in the top 4 nm of the film, which is where the reactive species (i.e. bridging oxygens and terminal hydroxyl oxygen atoms) reside. O 1s difference spectra (Figure 3.10) and Pb 4f difference spectra (Figure 3.9) help to further illustrate this point by

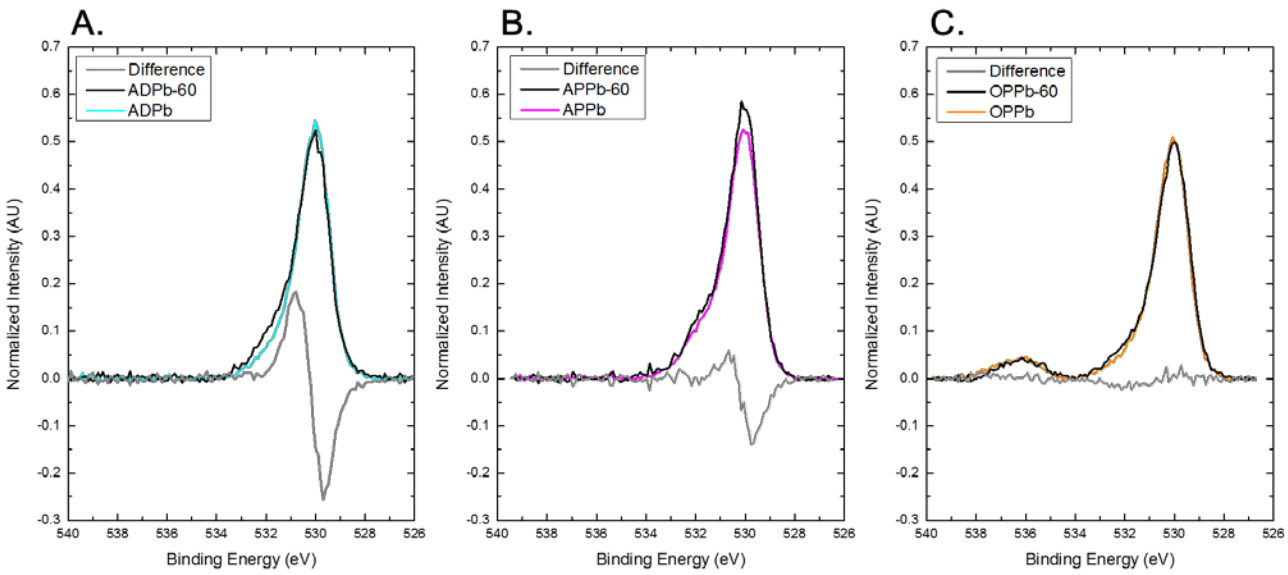

Figure 3.10: O 1s difference spectra showing the 60-degree collection angle subtracted from the normal collection angle for the lead-treated substrates (A) AD Pb TiO_2 (B) AP Pb TiO_2 (C) OP Pb TiO_2

showing the clear differences in the envelope when measuring the angle-resolved data and the normal collection angle data. Overall, argon plasma treatment acts to remove carbonaceous contamination from the TiO_2 surface while also exposing more reactive bridging oxygens and hydroxyl groups. These species on the surface, specifically the terminal hydroxyl groups are responsible for providing electrons that coordinate to the Pb^{2+} center when deposited from solution. Thus, Pb deposition from solution onto AP TiO_2 results in a

higher Pb surface coverage by approximately double, resulting from the removal of carbon and slight increase in the bridging oxygen and terminal hydroxyl groups. This increased surface coverage of Pb implies that upon perovskite deposition, more reactive sites are capable of binding Pb from the precursor solution: the effects of which are explored further in the chapter.

Lastly, lead treated OP TiO_2, hereafter referred to as OP Pb TiO_2 and the composition was evaluated using XPS and then compared to OP TiO_2 and AP Pb TiO_2 in order to evaluate how the surface chemistry of TiO_2 subjected to oxygen plasma cleaning impacts how this substrate could behave in the presence of perovskite precursor solution modeled by Pb adsorption from solution. The O 1s envelope (Figure 3.1) is deconvoluted into four regions, represented by lattice oxygen (O(lat)) accounting for 71.2 ± 0.3% of the envelope, bridging oxygen (O(br)) at 16.8 ± 0.4%, terminal hydroxyl oxygen (O(t)) at 6.0 ± 0.5%, and the superoxide species found on OP TiO_2, O(SO) at 6.1 ± 0.6%. Compared to OP TiO_2, OP Pb TiO_2 shows basically the same amounts of lattice oxygen but shows an increase in bridging oxygen and the superoxide species. This finding is likely a result of the high carbon content on OP TiO_2, which is discussed previously, which explains the inconsistency between AP TiO_2 and OP TiO_2.

The Ti 2p region (Figure 3.2) of OP Pb TiO_2 shows the Ti $2p_{3/2}$ peak at ca. 459 eV. The envelope is comprised of a single Ti^{4+} species. The surface stoichiometry indicated by the O/Ti ratio does not differ much, despite the reduced amount of surface carbon. In comparison to OP TiO_2, the O/Ti ratio and theO(t)/O(l) remains relatively the same within a standard deviation, thus indicating that the lead adsorption process does not significantly change the stoichiometry detected by XPS. Compared to AD Pb TiO_2, the O/Ti ratio increases

from 2.35 ± 0.05 to 2.53 ± 0.01, which indicates that there are still more exposed surface oxygen species when oxygen-plasma treated versus the as-deposited substrate.

The C 1s spectrum of OP Pb TiO_2 is shown in Figure 3.3. Interestingly, the deconvolution of the C 1s spectrum indicates a lack of oxidized carbon species and the major contributors to the envelope are aliphatic carbon and R-OH groups, which is consistent with the mechanism by which oxygen plasma removes carbonaceous species from the surface; however, after the lead adsorption process, there is a small amount of oxidized carbon species, though much less than that of AD and AP TiO_2. The oxidized carbon species originate from the solvent rinsing process, as DMF and isopropanol both contain oxidized carbon and could engage in interactions with both the TiO_2 surface and act as weak coordinators for the lead that is on the surface.

The Pb 4f core level (Figure 3.5) was also measured for OP Pb TiO_2 in order to quantify the lead deposited on the surface from the lead adsorption process when the bare substrate is subjected to oxygen plasma treatment prior to deposition. Like AD Pb TiO_2 and AP Pb TiO_2 the Pb $4f_{7/2}$ peak of OP Pb TiO_2 has a binding energy of ca. 139 eV, a binding energy similar to $PbTiO_3$, which has the Pb $4f_{7/2}$ binding energy at 139.0 eV[77] and a similar coordination environment as Pb on TiO_2. The atomic percentage of Pb on the OP Pb TiO_2 surface is 1.05 ± 0.09%, which is equivalent to a surface coverage of 2.42 x 10^{-11} mol/cm^2, or 26% of a monolayer. Compared to AD Pb TiO_2, this is a significant reduction in surface coverage from 37% of a monolayer and a greater reduction when compared to AP Pb TiO_2, which had a surface coverage of 68% of a monolayer. This decreased lead concentration on oxygen-plasma treated TiO_2 is likely impacted by the superoxide species that forms during the plasma treatment process. The superoxide species present throughout the film increases the

work function of the surface (Appendix A), which means that oxygen plasma treatment is removing available electrons that could otherwise participate in the Pb coordination process. Thus, the oxygen plasma treated surface is the least effective at capturing Pb ions from solution.

Angle-resolved data reveals which species are surface-specific by reducing the probe depth by half. The O 1s-60 spectrum (Figure 3.6) of OP Pb TiO_2 has the envelope deconvoluted into four regions with O(l) representing 64.4%, O(br) representing 18.0%, O(t) representing 9.8%, and O(SO) with 6.2%. Compared to the OP Pb TiO_2 substrate collected at 90° rather that 60°, there is a decrease in the lattice oxygen concentration and an increase in the O(br) and O(t) concentrations, which is consistent with other angle-resolved data in this study. Interestingly, the O(SO) species appears to be evenly distributed throughout the film, as the concentration does not change with the collection angle. Although the reactive O(br) and O(t) species are on the surface of the film and should be capable of coordinating Pb^{2+}, the O(SO) species spread throughout the TiO_2 near-surface region seems to be preventing that coordination by being more electron-withdrawing. This result is not ideal for an electron-selective interlayer, as the superoxide species raises the work function of the TiO_2 contact and can introduce electron injection barriers when implemented in a photovoltaic device. As with the other substrate measurements, no significant changes were observed in the Ti 2p angle-resolved data (Figure 3.7). When evaluating the O/Ti ratios the O/Ti ratio remains the same, indicating that there are no depth-dependent stoichiometric changes in the film. As with previous angle-resolved data discussed, there is an increase in the atomic percent of carbon (Figure 3.8) from 21.30% to 41.32% without any significant deviations in the atomic percentages of the deconvoluted envelope that resides on the top

layer of the TiO_2 surface. Like the Pb 4f spectrum for AD Pb TiO_2 and AP Pb TiO_2, OP Pb TiO_2 shows an increase (Figure 3.10) in the atomic percentage of Pb on the surface from 1.05% to 1.77%, which is representative of a nearly doubled increase in the atomic concentration of Pb, similar to what was observed for AD Pb TiO_2 and AP Pb TiO_2. This observation further confirms the location of the Pb cations on the TiO_2 surface to be bound in the top 4 nm of the film, which is where the reactive species (i.e. bridging oxygens and terminal hydroxyl oxygen atoms) reside. O 1s difference spectra (Figure 3.10) and Pb 4f difference spectra (Figure 3.9) help to further illustrate this point by showing the clear differences in the envelope when measuring the angle-resolved data and the normal collection angle data. Overall, oxygen plasma treatment acts to remove carbonaceous contamination from the TiO_2 surface while also depositing a new superoxide species during the plasma treatment process. These species on the surface, specifically the terminal hydroxyl groups are responsible for providing electrons that coordinate to the Pb^{2+} center when deposited from solution, while the superoxide species seem to prevent the surface from binding more Pb cations.

3.3 Characterizing Perovskite Film Crystallinity on Bare TiO_2 and Lead-Adsorbed TiO_2

Device-relevant $CsPbBrI_2$ perovskite films were deposited onto AD TiO_2, AP TiO_2, OP TiO_2, and the oxide substrates modified with adsorbed Pb^{2+} to examine the effect of TiO_2 surface chemistry on the crystallinity of perovskite films. The perovskite films yield two Bragg peaks (Figure 3.11), at 14.75° and 29.65°, which correspond to the (100) and (200)

crystallographic planes and a cubic crystal structure with a unit cell length of 6.01 Å. These numbers are in good agreement with literature reporting on the same material[11].

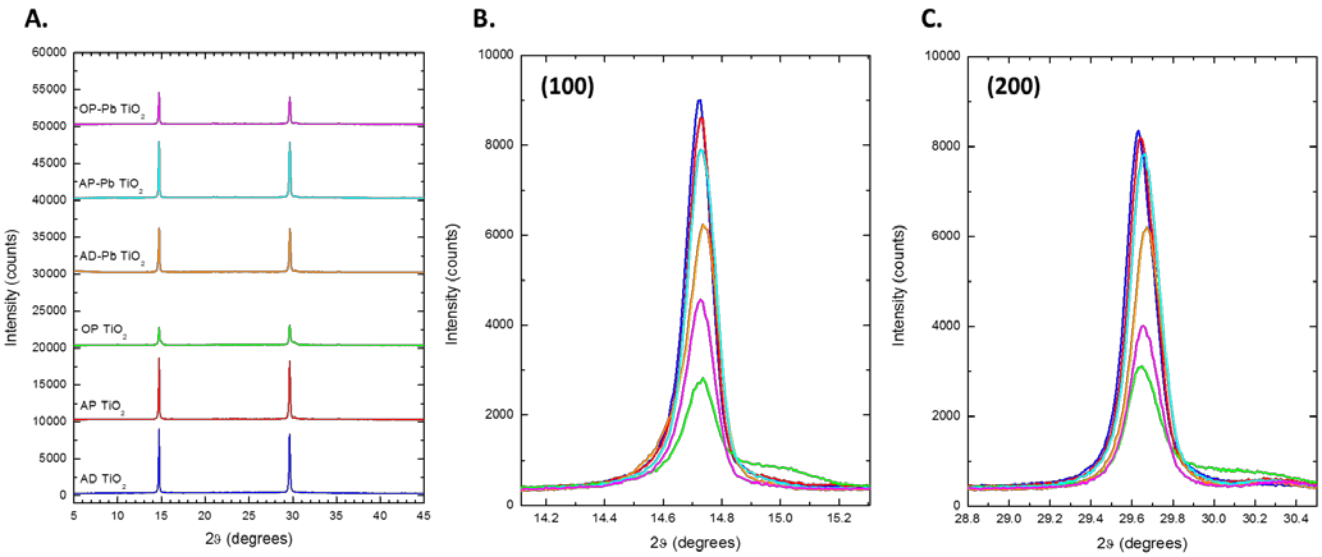

Figure 3.11: (A) X-ray diffraction data for $CsPbBrI_2$ on AD TiO_2, AP TiO_2, OP TiO_2, AD Pb-TiO_2, AP Pb-TiO_2, and OP Pb-TiO_2 (B.) Zoomed in view of the (100) Bragg peak and the (C.) (200) Bragg peak.

The Scherrer equation (Eq. 3.4) was used to determine the crystal coherence length

$$\tau = \frac{K\lambda}{\beta \cos\vartheta} \qquad (3.4)$$

using the FWHM of the (100) peak, where τ is the coherence length of the diffracting crystal averaged over the space of the film that is sampled. The maximum value of τ is the grain size. *K* is a dimensionless shape factor that accounts for the shape of the peak distribution. For a cubic lattice, a value of 0.96 can be used. The incident x-ray radiation wavelength, λ is 1.54 Å, which is the wavelength produced by a Cu $K\alpha_1$ anode. The peak FWHM is indicated by β, which does not include the natural line width from the instrument. Lastly, ϑ is the diffraction angle. The calculated coherence lengths are given in Table 3.3.

Surface	Coherence Length (nm)	Pb %Difference
AD TiO_2	162.170 ± 0.001	32%
AD Pb-TiO_2	110.922 ± 0.009	
AP TiO_2	161.151 ± 0.000	-11%
AP Pb-TiO_2	145.586 ± 0.001	
OP TiO_2	123.188 ± 0.000	15%
OP Pb-TiO_2	145.587 ± 0.002	

Table 3.3: Calculated coherence lengths using the Scherrer equation for $CsPbBrI_2$ on TiO_2

AD TiO_2 had the longest crystal coherence length at 162 nm and the highest crystallinity. After lead adsorption onto AD Pb-TiO_2, the perovskite crystal coherence decreased by ca. 50 nm. A similar result was seen for AP TiO_2, which has a crystal coherence length of 161 nm and a degree of crystallinity similar to that of AD TiO_2. When a perovskite film was deposited on AP Pb-TiO_2, the crystal coherence length also decreased, but by ca. 15 nm instead. The (100) peak intensity of OP TiO_2 is three times less than the Bragg peak intensity of AD TiO_2 and also shows a lower crystal coherence length of 123 nm. Unlike the other substrates that had been treated by lead adsorption, perovskites deposited on OP Pb-TiO_2 show an increase in crystal coherence length to 146 nm. Origininally, we had hypothesized that the lead on the surface would act as nucleation points on the TiO_2 that would reduce the epitaxial strain inherenent to the system, given that the perovskite unit cell is 6.0 Å and the TiO_2 unit cell is 3.7 Å. Moreover, the lead adsorbed to TiO_2 would result in a more chemically heterogeneous surface once the reactive terminal hydroxyl groups are tied up by the lead. However, these results suggest that the lead cations on the surface are benefical to surface homogenization if there is molecular oxygen on the surface. Additionally, the observed decrease in coherence length is ultimately contrary to the original hypothesis. Lead modification does not improve crystallinity. Considering that the lead adsorption process titrates away the adjacent hydroxyl sites on the TiO_2 surface, these particular

chemical species are likely important for the initial nucleation of the perovskite film. The free energy of formation of PbO (-244.58 kJ/mol) is more favorable than formation of PbI_2 (-235.36 kJ/mol). Thus, once lead adsorption ties up these most reactive sites on the TiO_2 surface, these adjacent hydroxyl groups are no longer available to begin initial nucleaton of the perovskite films. Discussed in more detail at the end of the next section, the spacing of the hydroxyl groups with respect to the lattice spacing of the lead atoms in the perovskite unit cell are significantly mismatched at 3.8 Å versus 6.0 Å, respectively. Thus, the adsorption of lead onto these sites that aid in the nucleation of the perovskite crystal from the precursor solution can disrupt the nucleation by reaction with these reactive terminal hydroxl sites on the TiO_2.

Overall, lead treatment of TiO_2 improved the crystallinity and coherence length of perovskite films that were grown on OP Pb-TiO_2, compared to perovskite grown on OP TiO_2, but decreased the crystallinity on AD Pb-TiO_2 and AP Pb-TiO_2. Compared to others studies done on the $CsPbBrI_2$ perovskite[11] the XRD data of the films presented herein show very low intensities of or the absence of the (101) and (110) Bragg peaks. The perovskite film growth on TiO_2 in general are therefore highly oriented films in the cubic phase. The differences in the intensity and the coherence length of these films as a function of surface treatment demonstrates the impact that the TiO_2 surface chemistry has on the bulk crystallographic properties of perovskite films.

3.4 Preferential Orientation of Perovskite Films Determined with GIWAXS

Wide-angle X-ray scattering data were collected at grazing incidence angles for perovskite films that had been grown on bare TiO_2 substrates and the TiO_2 films after lead adsorption, shown in Figure 3.12. GIWAXS data is useful for determining if there is preferential orientation of a crystalline thin film because the 2D detector allows one to collect diffraction data through all of reciprocal space.

Depth profiling of the films can be done by examining the integrated diffraction intensity as a function of incident angle. When the incident X-rays are below the critical angle, the measurement becomes surface-sensitive, but when the incidence angle of the X-rays is above the critical angle, the diffraction originates from the near-surface region and bulk regions. The critical angle (α_C) of $CsPbBrI_2$ was calculated to be 0.23° for a wavelength of 0.976 Å using Equation 3.5 and Equation 3.6[78], where N_0 is Avogadro's number, Z is the

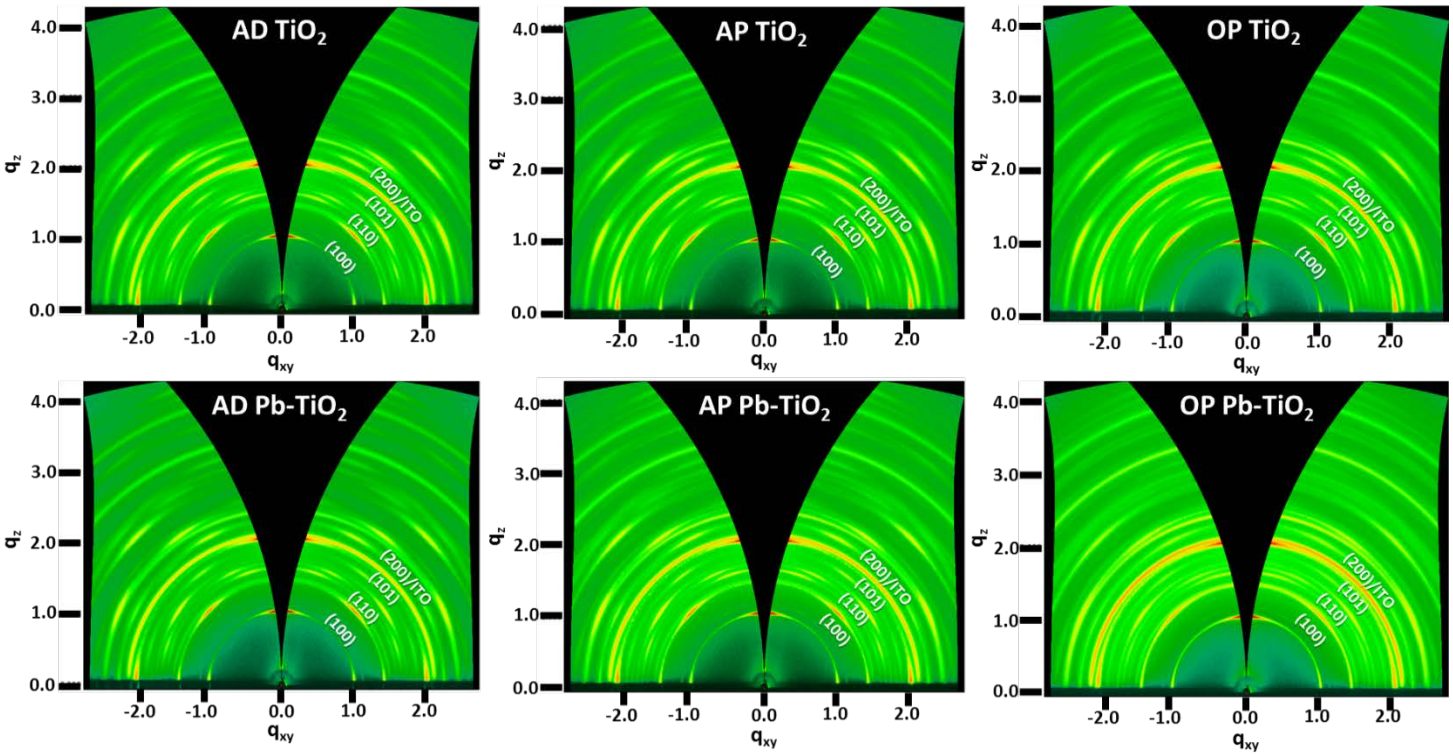

Figure 3.12: GIWAXS images collected for $CsPbBrI_2$ films on TiO_2 at an incidence angle of 0.50° in q_z versus q_{xy}.

average atomic number and A is the average atomic mass. This result agrees nicely with experimental data, which shows the critical angle to be ca. 0.20° (Figure 3.11) as that incidence angle gives the maximum integrated intensity value for all the films[78]. The measured value agrees nicely with the calculated value. Both the calculated critical angle and the experimental critical angle values are consistent with other perovskite materials that also have a critical angle of ca. 0.20° in the X-ray regime[8].

$$\alpha_C \cong \sqrt{2\delta} \qquad \text{(Eq. 3.5)}$$

$$\delta = N_0 \frac{e^2}{2\pi mc^2} \frac{Z\rho}{A} \lambda^2 \qquad \text{(Eq. 3.6)}$$

The measured value agrees nicely with the calculated value. Both the calculated critical angle and the experimental critical angle values are consistent with other perovskite materials that also have a critical angle of ca. 0.20° in the X-ray regime[8].

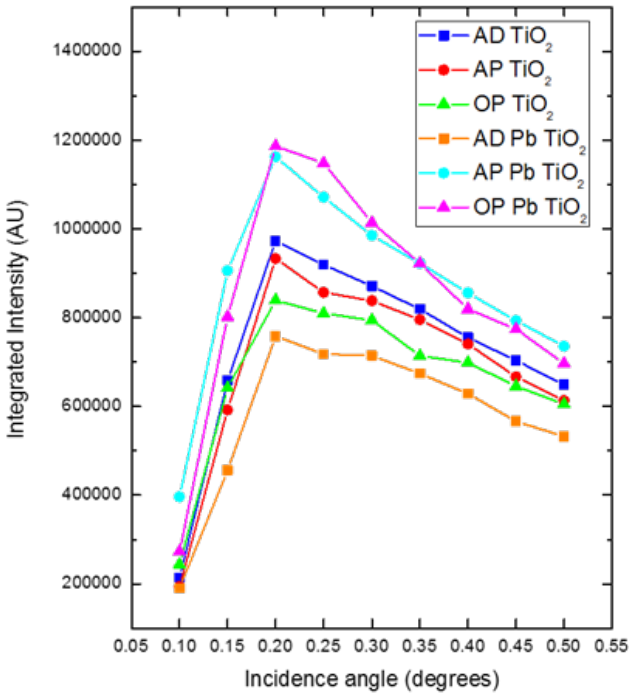

Figure 3.13: Plot of integrated intensity of the (100) Bragg peak as a function of incidence angle. The maximum integrated intensity value indicates the incidence angle.

Figure 3.14 shows a plot of incidence angle versus depth probed calculated using Equations 3.7 and 3.8[78], where D(φ) is the depth as a function of incidence angle, λ is the incidence radiation wavelength, and q is given in equation 3.8. In the GIWAXS images measured below the critical angle (not shown), the diffraction rings for ITO, which have a q

$$D(\varphi) = \frac{\lambda}{4\pi q} \qquad \text{(Eq. 3.7)}$$

$$q = \frac{\left[\sqrt{\varphi^2 - \varphi_C^2 + 4\delta_i^2} + \varphi_C^2 - \varphi^2\right]^{1/2}}{\sqrt{2}} \qquad \text{(Eq. 3.8)}$$

value of 2.15 Å^{-1} are not visible until measuring at α = 0.25°. Based on this measurement, the perovskite films are on the order of 100 nm thick and measurements made below this angle reveal depth-dependent properties.

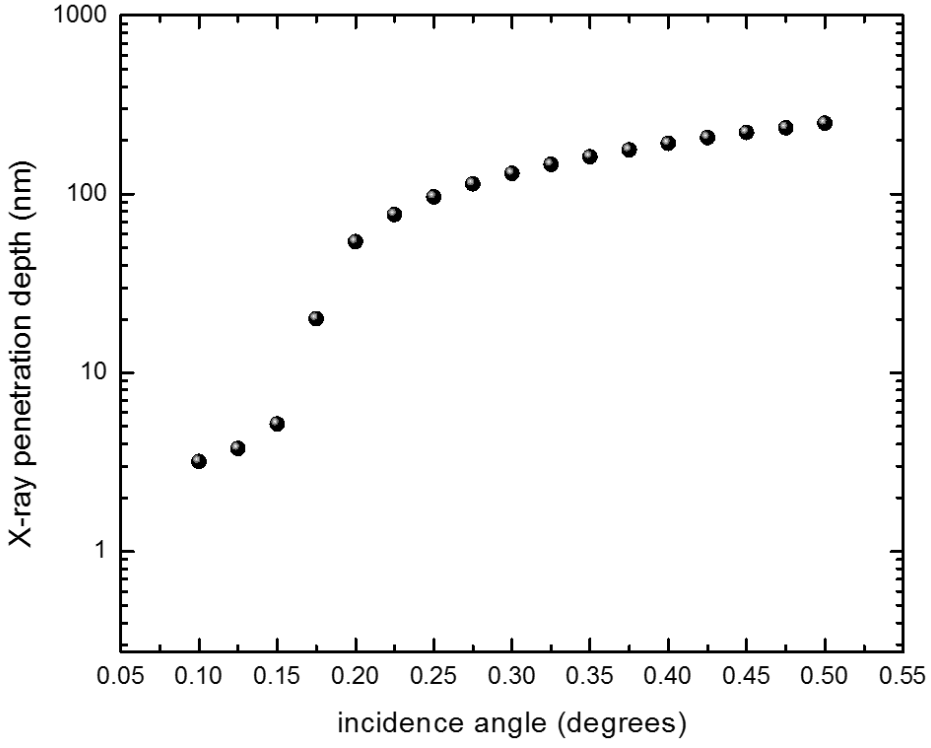

Figure 3.14: X-ray penetration depth as a function of incidence angle using calculated values for $CsPbBrI_2$

The Debye-Scherrer ring corresponding to the (100) plane of the $CsPbBrI_2$ perovskite has a *q* value of 1.045 $Å^{-1}$, which is equivalent to an interplanar spacing of 6.01 Å, the same value measured using XRD. All of the perovskite films grown on TiO_2 exhibit an anisotropic distribution of intensity values of the (100) ring as a function of angle, χ. In order to determine the degree of preferential orientation, the Debye-Scherrer ring is linearized and then integrated over 0.95-1.15 $Å^{-1}$ to yield the plots in Figure 3.15.

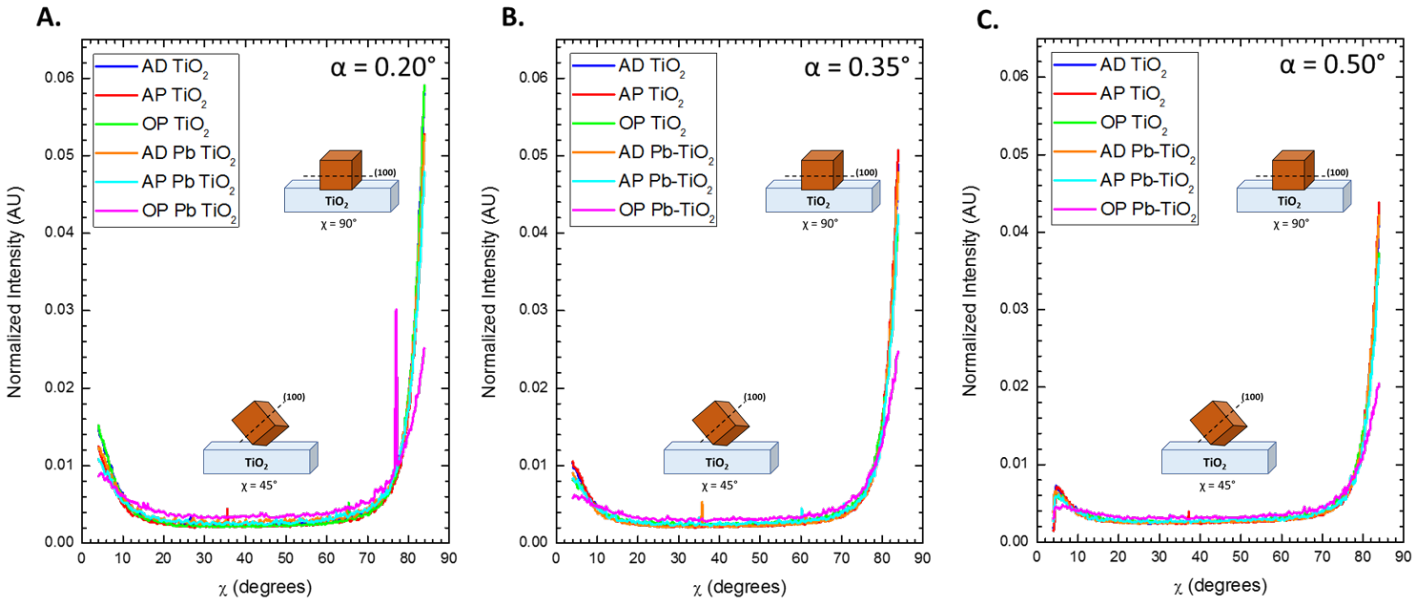

Figure 3.15: Normalized intensity of the (100) Debye-Scherrer ring as a function of azimuthal angle, χ which is the angle of vector Q with respect to the q_{xy} plane. The anisotropic distribution of intensity values skewed toward ca. 90° indicates preferential orientation along q_z for all samples.

There is a depth-dependence on preferential orientation of the perovskite. Figure 3.16 is a plot of the In-Plane:Out-of-Plane intensity ratios as a function of incidence angle, which was calculated by integrating the intensity versus chi plot from 80-84° to find the in-plane integral then dividing by the integral from 43-47° to obtain the out-of-plane value. At a depth that exceeds the RMS roughness of all films at ca. 50 nm, which is achieved by measuring at an incidence angle of 0.20 degrees, the perovskite on OP TiO_2 exhibits the greatest degree of preferential orientation, with the IP:OOP ratio at 15.5. This value is in stark

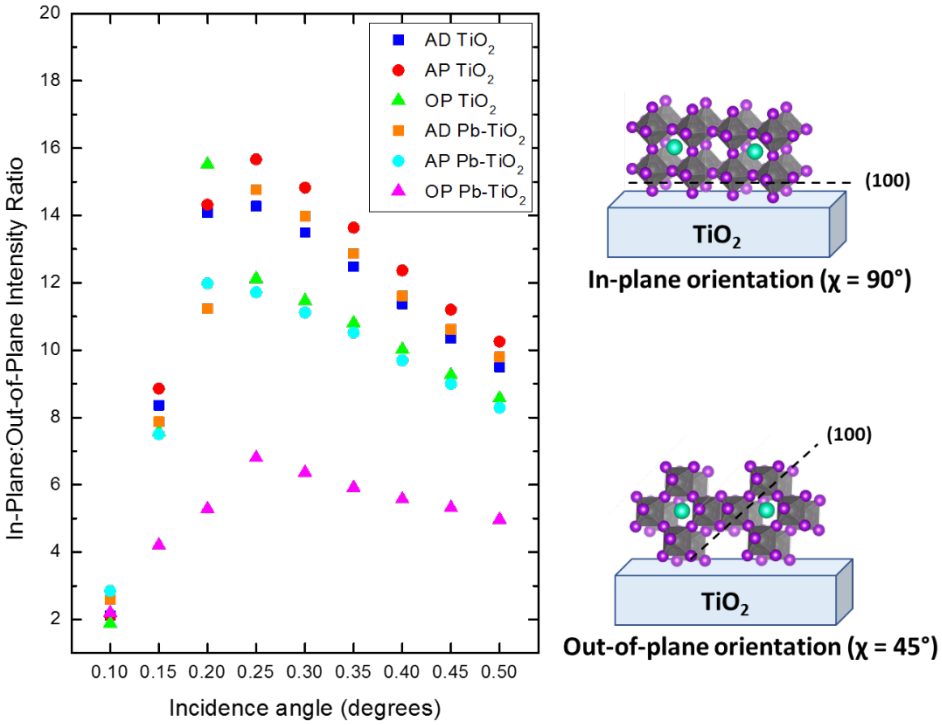

Figure 3.16: Preferential orientation plot describing the in-plane to out-of-plane integrated intensity ratios as a function of incidence angle for $CsPbBrI_2$ on TiO_2

contrast to the OP-Pb TiO2 ratio of 5.3 at the same angle. At 0.20 degrees, the bare substrates exhibit the greatest degree of preferential orientation compared to the lead-modified oxide substrates. AD and AP TiO_2 have similar preferential orientation ratios of 14.1 and 14.3 respectively. Lead adsorption on TiO_2 did not improve the degree of preferential orientation of the perovskite films at this angle. AD Pb-TiO_2 and AP Pb-TiO_2 had IP:OOP ratios of 11.2 and 12.0, corresponding to a decrease in preferential orientation of 20.4% and 16.4% respectively. However, this observation does not persist as the incidence angle increases and more of the film is measured. At $\alpha = 0.50°$, the substrate that results in the greatest degree of preferential orientation is AP TiO_2. Lead adsorption has slightly improved preferential orientation on AD TiO_2 by 3.2%, but AP Pb-TiO_2 and OP Pb-TiO_2 continue to show lower degrees of preferential orientation. Although lead adsorption was only shown to improve perovskite preferential orientation on AD Pb-TiO_2 versus AD TiO_2, these data do show a

definitive difference in preferential orientation changes based on the amount of accessible hydroxyl groups on the TiO_2 surface. These accessible hydroxyl groups give rise to a preference for the <100> plane because the hydroxyl groups can capture lead and therefore begin to orient with the most lead-rich low-index plane parallel to the TiO_2 surface.

With the exception of AD Pb-TiO_2, the perovskite preferential orientation was not enhanced by lead adsorption. The enhancement of orientation on AD Pb-TiO_2 likely has to do with the removal of adventitious carbon from the substrate during the lead adsorption process. Additionally, the removal of carbon during lead adsorption reveals newly accessible hydroxyl groups. In the case of AP Pb-TiO_2 and OP Pb-TiO_2, XPS data show instead that lead adsorption increases the amount of carbonaceous material on the surface, as discussed in section 3.1. The amount of adventitious carbon on the TiO_2 surface impacts the preferential orientation of perovskite films negatively because adventitious carbon increases the interfacial disorder at the perovskite/TiO_2 interface, which impedes the initial nucleation of the perovskite on TiO_2. Based on the XPS data, there are certain reactive hydroxyl sites on the TiO_2 surface that do react with lead cations. If those reactive sites are not immediately accessible because they are blocked by the carbonaceous overlayer, then the nucleation event and subsequent perovskite growth is also impeded.

Overall, GIWAXS experiments have revealed that the crystallinity and preferential orientation of the perovskite thin films are impacted by the amount of adventitious carbon on the underlying substrate, TiO_2. Although AD TiO_2 exhibited the greatest crystallinity, this film does not have the greatest degree of preferential orientation, which was seen on AP TiO_2. The preferential orientation of AD TiO_2 was improved by the lead adsorption process because the solvent washing removes carbonaceous material from the surface. Conversely,

AP Pb-TiO_2 and OP Pb-TiO_2 did not see improvements in preferential orientation over AP TiO_2 and OP TiO_2, respectively. AP TiO_2 and OP TiO_2 have comparable amounts of carbon on the surface but see differences in crystallinity and preferential orientation because AP TiO_2 has a more homogeneous chemical environment on the surface, whereas the oxygen plasma treatment process introduces molecular oxygen to the surface, which increases the surface heterogeneity. Additionally, the lead adsorption experiments revealed that the OP TiO_2 surface is not as efficient as capturing lead, which seems to be critical in the formation of the perovskite/TiO_2 interface and subsequent growth of the perovskite layer.

Although the lead surface coverage is relatively small at ca. 2 x 10^{-11} mol/cm^2, this amount of lead on the surface does begin to inhibit growth of the perovskite unit cell. A likely origin of this observation is the lattice mismatch between the perovskite and TiO_2 anatase, with unit cell dimensions in the plane of the substrate at 6.0 Å and 3.8 Å, respectively (Figure 3.17). The nucleation and growth process of perovskite on TiO_2 proceeds semi-epitaxially, with the TiO_2 being polycrystalline. Lead bound to the TiO_2 surface has an ionic radius of

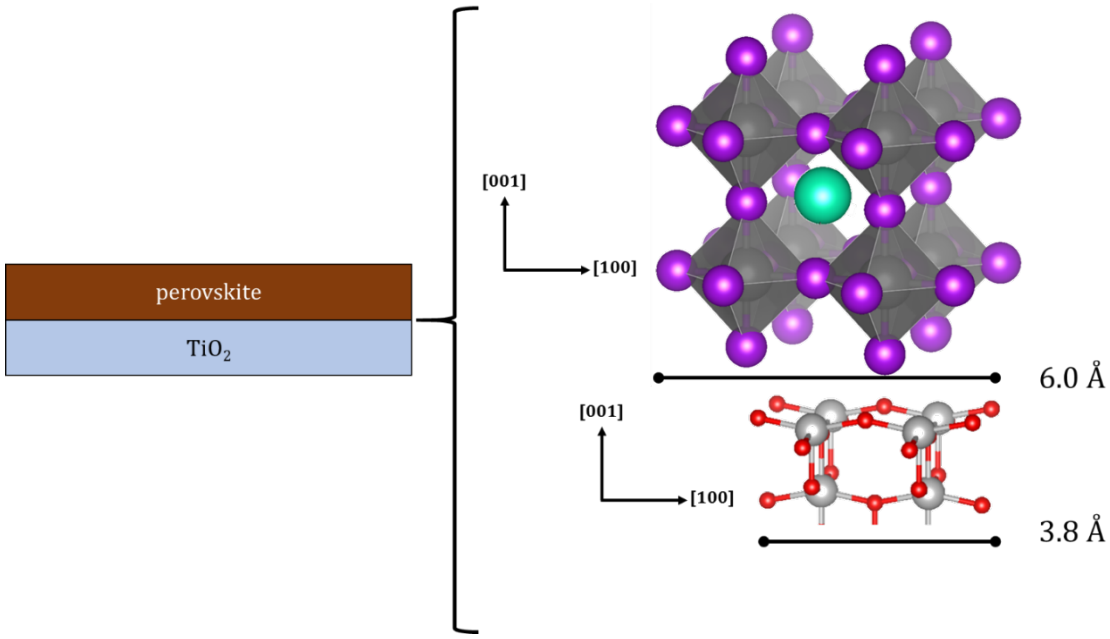

Figure 3.17: Perovskite unit cell and TiO_2 anatase unit cell shown with the unit cell dimensions to scale

1.43 Å, which is approximately half of the anatase unit cell. The position of the adsorbed lead atoms on TiO_2 does not match up with the unit cell of $CsPbBrI_2$. Thus, we suggest that the addition of adsorbed lead inhibits both the crystallinity and the crystal coherence length because adsorbed lead is introducing an interfacial layer that is amorphous and disordered because there is a significant lattice mismatch of the adsorbed lead on TiO_2 and the perovskite. When compared to bare substrates without any adsorbed lead, the crystallinity and coherence length are greater in magnitude, as these substrates are allowing the reactive sites of the TiO_2 to interact with the perovskite precursors in solution. It is reasonable to suggest that some templating could occur with this system on the metal oxide surface given a higher surface coverage of adsorbed lead or if there was a change in the hydroxyl density on the surface that would allow for a higher surface coverage of adsorbed lead. Nevertheless, we have shown that the surface chemistry of TiO_2, specifically the reactive hydroxyl groups on the surface, plays a role in directing the nucleation and growth of a perovskite overlayer on this contact.

3.5 Perovskite Film Morphology Revealed by AFM

The morphology of perovskite films grown on TiO_2 that had been subject to various plasma treatment was evaluated using atomic force microscopy (AFM) in order to determine if TiO_2 surface treatment impacts the morphology of the perovskite film. AFM images of

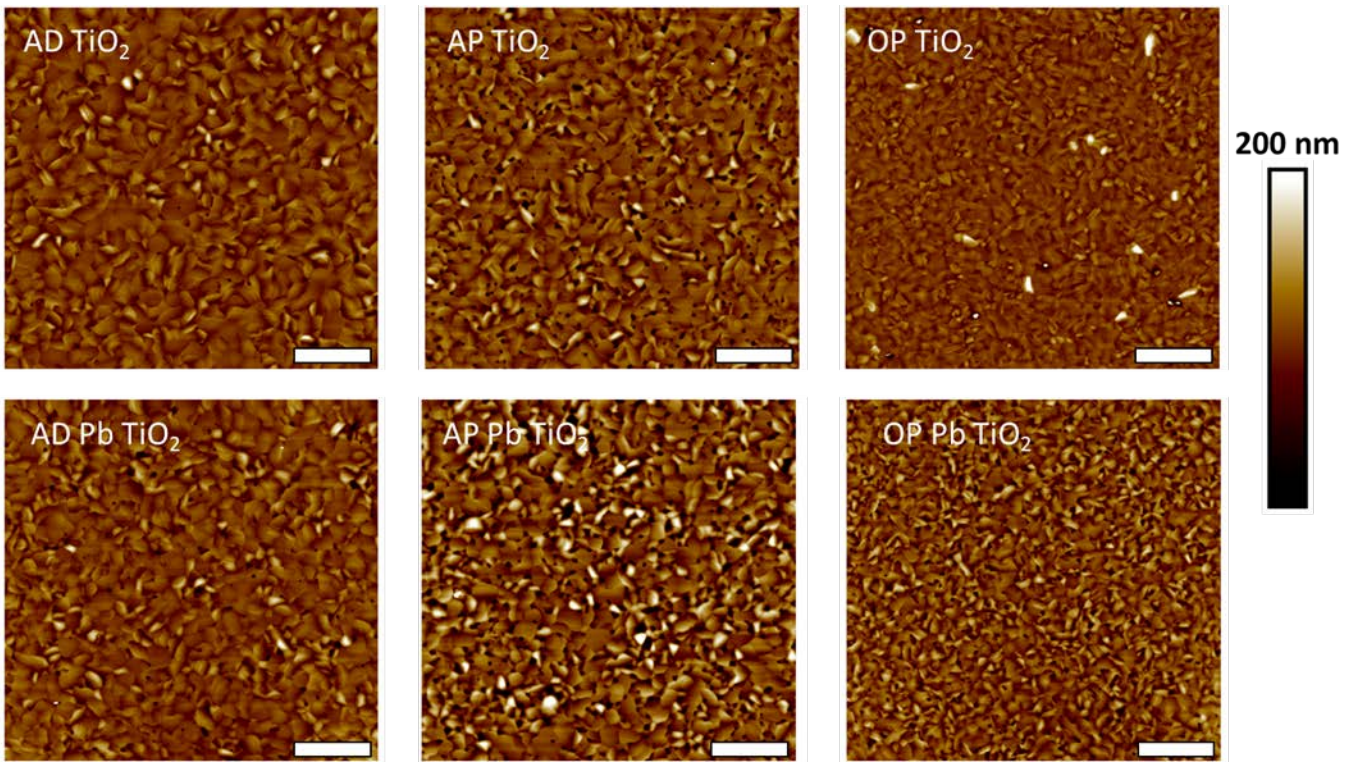

Figure 3.18: AFM images of $CsPbBrI_2$ films on TiO_2 with the surface treatment indicated in the upper left corner. Scale bar is 4 μm.

perovskite on the bare substrates (AD TiO_2, AP TiO_2, and OP TiO_2), and the lead-adsorbed substrates (AD Pb-TiO_2, AP Pb-TiO_2, and OP Pb-TiO_2) are shown in Figure 3.18. The RMS roughness of each film was measured and displayed in Table 3.4.

The morphology of the TiO_2 substrate shows that TiO_2 deposition by chemical vapor deposition results in the conformal growth of a film on ITO. The TiO_2 maintains a consistent

Surface treatment	RMS roughness (nm)
AD TiO_2	16.3 ± 0.8
AD Pb-TiO_2	18.1 ± 1.1
AP TiO_2	23.2 ± 0.5
AP Pb-TiO_2	33.8 ± 1.5
OP TiO_2	13.2 ± 1.8
OP Pb-TiO_2	23.5 ± 0.9

Table 3.4: RMS roughness of the films shown in Figure 3.18 and averaged over 4-5 measurements of the same film.

grain size of ca. 150 nm and an RMS roughness of ca. 3.0 nm with ITO. Plasma treatment does not affect the TiO_2 morphology.

The perovskite crystallites on AD TiO_2 have a smooth appearance with some crystallites oriented up rather than oriented in the plane of the film. Although there are some pinholes in the film, the film itself is rather smooth with an RMS roughness of 16.3 nm and the film lacks significant gaps between grains that are ca. 1 μm in size. In contrast, the perovskite film on AP TiO_2 has a large number of pinholes within the film that are both at grain boundaries and within grains. In general, the perovskite grains on AP TiO_2 are approximately the same size as the grains on AD TiO_2 but has a larger density of smaller crystallites. Consequently, this film has a greater RMS roughness of 23.2 nm. The increased roughness of the film from the irregular grains and the pinholes compared to the film on AD TiO_2 result in a lower crystal coherence length and lower diffraction intensity, as seen with the XRD results. The perovskite film on OP TiO_2 has grains that are also ca. 1 μm in size, but the grains on average have a more consistent size than those on AD and AP TiO_2. This film has a lower density of pinholes than the films on AD and AP TiO_2, but does have some larger gaps in the film at the grain boundaries. Compared to the other two films on bare substrates, this film has only minimal grains that are oriented perpendicular to the surface instead of along the surface axis. Additionally, the RMS roughness is 13.2 nm, which is approximately 10 nm less than the RMS roughness of AP TiO_2 and about 10% less than that of AD TiO_2. Although the film on OP TiO_2 is the smoothest film with the lowest RMS roughness, the perovskite film has the lowest crystallinity and the lowest coherence length.

The perovskite film on AD Pb-TiO_2, similar to the perovskite film on AD TiO_2 has grains that are ca. 1 μm in size, however there is about 5% of the film that has grains oriented upward that are smaller in size, on the order of 200 nm in size. This film has more pinholes in it than the film made on AD TiO_2 and has an RMS roughness of 18.8 nm, which is larger than the roughness of AD TiO_2 and OP TiO_2, but less than AP TiO_2. Lead adsorption appears to have increased the amount of grains oriented away from the plane of the film, and slightly increased the RMS roughness. The XRD data also shows a decrease in the coherence length of the perovskite, which could be attributed to the increased amount of out-of-plane grains on the film surface. Lead adsorption appears to have the same effect on AP Pb-TiO_2 as it does on AD Pb-TiO_2. The perovskite film on AP Pb-TiO_2 sees an increase in RMS roughness from 23.2 nm on the bare substrate to 33.8 nm, a result of increased pinholes. This film also has a lower diffraction intensity and a smaller coherence length. The perovskite film on OP Pb-TiO_2, like the rest of the perovskites on lead-adsorbed TiO_2 substrates, shows an increase in RMS roughness from 13.2 nm to 23.5 nm. This represents a 10 nm increase in RMS roughness upon lead adsorption, which is consistent for both plasma treated (AP and OP) substrates. There is also an increase in the number of pinholes in the film, which is consistent with all of the lead-adsorbed substrates. A morphological change beyond the number of pinholes is observed for OP Pb-TiO_2 versus OP TiO_2 as the grain size has decreased upon lead adsorption. Interestingly, the diffraction intensity and crystal coherence length increased for OP Pb-TiO_2 compared to OP TiO_2; however, the AFM images suggest that changes made to adjacent hydroxyl groups that are capable of participating in chemical reactions either by plasma treatment or by lead adsorption has a negative impact on the RMS roughness of the film and the average crystallite size. Thus, we demonstrate that the surface chemistry of the

TiO_2 substrate impart changes to the perovskite layer in the interfacial region that propagate to the top of the film.

From the AFM images, we conclude that the morphology of perovskite films on TiO_2 is not enhanced by lead adsorption. Lead adsorption results in a film that has a larger RMS roughness. The roughness of the films could negatively impact the growth of the hole transport layer on top of the perovskite layer when making photovoltaic devices, as the roughness of the underlying film could prevent the hole transport layer from growing conformally on the perovskite. Additionally, the Pb-TiO_2 films show an increase in the number of pinholes in the perovskite film, which would negatively impact the electrical properties by causing shorts if the pinholes extend all the way through to the TiO_2 layer.

3.6 Concluding Remarks

From this XPS study, we can conclude that the chemical heterogeneity of TiO_2 affects the lead capturing efficacy of the surface. Argon plasma treatment of TiO_2 yield a surface that has a similar chemical composition to the as-deposited TiO_2, while still removing adventitious carbon. Conversely, a consequence of oxygen plasma cleaning TiO_2 is a change in the surface chemistry that includes the insertion of superoxide into the TiO_2 lattice, making the surface even more chemically heterogeneous. Despite changes made to the near-surface region by plasma treatment, the TiO_2 prepared in this work retains the binding energy difference of 71.5 eV previously reported[12] and the binding energies are in good agreement with other work[12,57].

TiO_2 with a larger concentration of terminal hydroxyl groups on the surface are more efficient at capturing lead, specifically those surfaces that have adjacent hydroxyl groups. The lead adsorption process onto TiO_2 proceeds through a mechanism in which a hydroxyl group donates electrons to the coordination sphere of lead. The lead most likely binds in a bidentate fashion, in which two hydroxyl groups are required for surface binding. The lead coverage on the surface is on the order of 3×10^{-11} mol/cm^2 for AD TiO_2, 6×10^{-11} mol/cm^2 AP TiO_2 and 2×10^{-11} mol/cm^2 for OP TiO_2. The surface chemistry of AD TiO_2 and AP TiO_2 with similar degrees of hydroxylation are better suited for capturing lead, though with less carbon on the surface, AP TiO_2 is much more capable of Pb capture. We assert that the binding of lead indeed requires adjacent hydroxyl groups and is assisted by the morphological heterogeneity of the TiO_2 surface, as indicated by AFM.

The surface chemistry of TiO_2 was shown by X-ray diffraction data to impact the crystallinity of perovskite films deposited on the various TiO_2 surfaces. The surface most efficient at lead capture, AD TiO_2, demonstrated the highest degree of crystallinity. Of the bare substrates, AD TiO_2 showed the highest crystallinity and OP TiO_2 showed the lowest crystallinity. The differences in crystallinity observed likely stem from the differences in surface chemistry. Although the AD and AP TiO_2 surfaces are chemically heterogeneous and defective, oxygen plasma treatment has shown to increase the surface heterogeneity by introducing a molecular oxygen species that decreases the amount of doping on the surface by reducing the density of oxygen vacancies. This surface heterogeneity introduced by oxygen plasma results in a film that is smoother, yet less crystalline than the other bare substrates.

The addition of lead on the surface was shown to decrease the perovskite film crystallinity and coherence length for AD Pb-TiO_2 versus AD TiO_2 and AP Pb-TiO_2 versus AP TiO_2, but increase both crystallinity and coherence length for OP Pb-TiO_2 versus OP TiO_2. The molecular oxygen species on OP TiO_2, which makes the surface more reducing, makes the surface less favorable for lead capture. However, the addition of lead already on the surface does help mitigate the effect of the surface chemistry on the crystallinity and coherence length. Moreover, we have shown that addition of adsorbed lead onto TiO_2 substrates with even a surface coverage as low as ca. 37% of a monolayer begins to impact the nucleation and growth of perovskite films on TiO_2.

AP TiO_2 showed the greatest degree of preferential orientation and comparable crystallinity to AD TiO_2. The surfaces of AP TiO_2 and AD TiO_2 have similar chemical environments because argon plasma treatment removes carbon from the surface without inflicting changes to the surface chemistry.

Based on these data, we highlight the importance of surface hydroxyl groups to the nucleation of perovskite films on TiO_2. Adjacent hydroxyl groups capture lead ions from solution to aid in the initial nucleation of the perovskite. Although contrary to the initial hypothesis, these reactive sites become titrated away via the lead adsorption experiment and the nucleation and growth of the perovskite film becomes hindered, as the precursor materials cannot easily bind to the TiO_2 surface.

Chapter IV: Conclusions and Future Directions

4.1 Conclusions

The chemical composition of the TiO_2 contact at the surface is critical in understanding the nucleation and growth of perovskite active layers. TiO_2 surfaces contain a myriad of chemical species including 6-fold coordinated Ti atoms, 5-fold coordinated Ti atoms (oxygen defects), terminal hydroxyl groups, and bridging oxygen, as determined by X-ray photoelectron spectroscopy. Argon plasma treatment retains the chemical environment of as-deposited TiO_2 while removing adventitious carbon. Oxygen plasma treatment reacts with the TiO_2 surface and introduces a molecular oxygen species that remains stable after the lead adsorption process. Lead adsorption introduces lead cations to TiO_2 that bind to terminal hydroxyl groups in a bidentate fashion with a surface coverage ranging from. 2 x 10^{-11} mol/cm^2 (OP Pb TiO_2) to 6 x 10^{-11} mol/cm^2 (AP Pb TiO_2) depending on the plasma treatment which impacts the surface chemistry.

Lead adsorption was hypothesized to reduce interfacial disorder at the perovskite/TiO_2 interface by titrating away reactive sites on the TiO_2 surface, while also acting as a nucleation site for the perovskite to grow. X-ray diffraction data indicate that lead adsorption leads to a decrease in crystallinity compared to the bare substrates but does increase the crystal coherence length of perovskite on OP Pb-TiO_2, which indicates that there is some critical threshold of Pb concentration on the surface wherein the concentration begins to inhibit crystal growth. GIWAXS data show that all surface treatments of TiO_2 result in a perovskite film that is preferentially oriented with the <100> crystallographic axis aligned normal to the surface. Lead adsorption improved the preferential orientation of the

$CsPbBrI_2$ films on AD Pb-TiO_2 compared to AD TiO_2, but ultimately, the AP TiO_2 substrate yielded the greatest degree of preferential orientation. The decline in perovskite preferential orientation originates at the TiO_2 surface. We have demonstrated that titrating away the adjacent hydroxyl groups on the surface with lead adsorption is detrimental to the crystallographic properties of the perovskite, likely originating from the TiO_2/perovskite lattice mismatch, thus highlighting the important role of the chemical reaction between TiO_2 and Pb-containing species in the perovskite precursor solutions. Although theoretical studies have shown that the TiO_2/$MAPbI_{3-x}Cl_x$ lattice mismatch is < 2% for the pseudocubic (001) surface, these experimental results suggest that the hydroxyl groups on the surface, not just the lattice match are the critical to the nucleation of perovskite active layers on TiO_2 surfaces.

Oxygen plasma treatment yielded the smoothest films by AFM, but all the perovskite films on bare substrates had RMS roughness values of ca. 20 nm. Lead adsorption did not improve the RMS roughness of the films and showed larger pinhole densities on all surface treatments. The perovskite surface morphology differences reflect differences in the interfacial surface chemistry. Substrates with a higher density of adjacent hydroxyl groups (i.e. AD and AP TiO_2) produced films that had larger, more uniform grain sizes, albeit slightly higher in RMS roughness than OP TiO_2. When adjacent hydroxyl groups in the near-surface region are bound to lead, the nucleation of these films become disrupted as the precursors cannot easily bind to the TiO_2 surface.

From the data herein, we ultimately conclude that lead adsorption on TiO_2 at a surface coverage of ca 2-6 x 10^{-11} mol/cm^2 has highlighted the important role that adjacent hydroxyl groups play on the nucleation and growth of perovskite films. Although the initial hypothesis

concerning the positive effect lead adsorption would have on the nucleation and growth of perovskite films was not supported by these data, we have demonstrated the critical role of the TiO_2 surface chemistry in the nucleation process.

4.2 Future Directions

Future directions for this project divert into two avenues. The first of which would be efforts to tightly control the surface coverage of Pb^{2+} on TiO_2 or use a different cationic surface modifier capable of forming octahedral complexes. The second direction for this project includes preparation of the mixed halide cesium perovskites such that they can be analyzed by high-resolution transmission electron microscopy equipped with electron energy loss spectroscopy capabilities. This experiment would be capable of spatially resolving the chemical composition of the perovskite/TiO_2 interface and would reveal the preferential reaction sites for the perovskite on TiO_2, which should complement the XPS data presented in this thesis.

In general, cesium-based perovskites offer an attractive alternative to the organic-inorganic hybrids because they offer increased stability. Additionally, this all-inorganic perovskite has components with good X-ray cross sections, so all atoms can be more easily detected compared to the carbon-based cations of MA and FA.

Studies such as those presented in this thesis help drive the fundamental science necessary to exhaustively understand how these materials can become viable products in the future.

Appendix A

Substrate	Work function (eV)
AD TiO_2	3.51 ± 0.02
AD Pb TiO_2	3.51 ± 0.02
AP TiO_2	3.67 ± 0.05
AP Pb TiO_2	3.69 ± 0.02
OP TiO_2	3.86 ± 0.01
OP Pb TiO_2	3.86 ± 0.07

Table A1: Tabulated values of measured work function for the differently treated TiO_2 surfaces

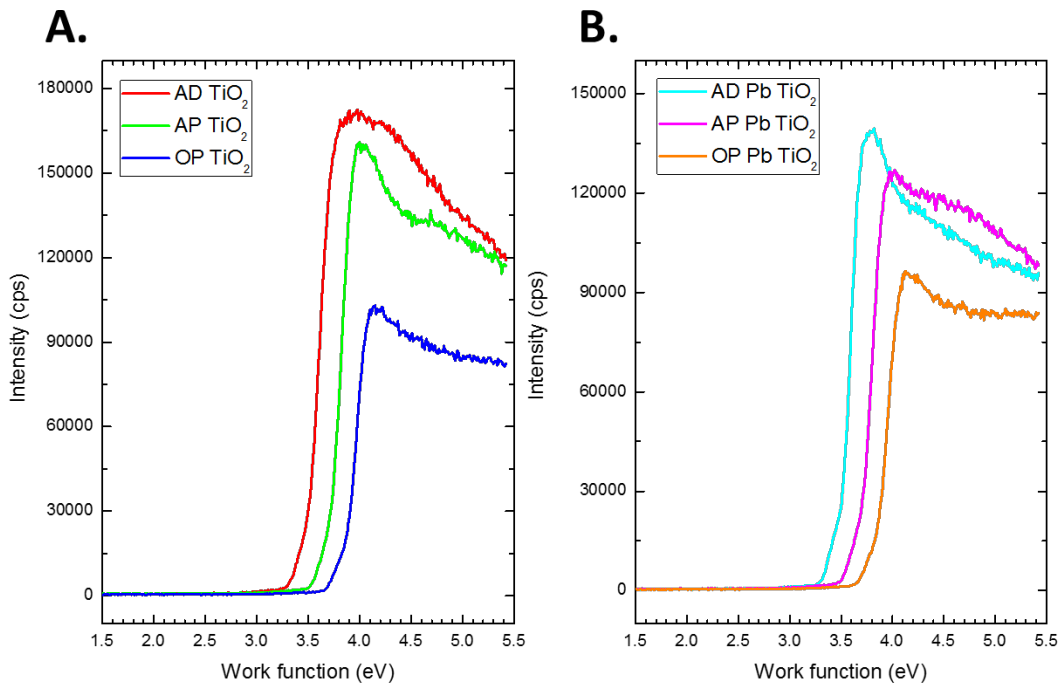

Figure A.1: Work function data for (A) AD TiO_2, AP TiO_2, and OP TiO_2 and (B) AD Pb TiO_2, AP Pb TiO_2, and OP Pb TiO_2. Addition of Pb on the surface does not significantly impact the work function, which is tabulated in Table A.1. The difference in work function can be attributed to the differences in surface chemistry, which are discussed in detail in Ch.3

References

1. A. Kojima, K. Teshima., Y. Shirai, T. Miyasaka, Organometal Halide Perovskites as Visible-Light Sensitizers for Photovoltaic Cells. *J. Am. Chem. Soc.* 2009, 131 (17), 6050-6051.

2. W. S. Yang, B.-W. Park, E. H. Jung, N. J. Jeon, Y. C. Kim, D. U. Lee, S. S. Shin, J. Seo, E. K. Kim, J. H. Noh, S. I. Seok, Iodide Management in Formamidinium-Lead-Halide-Based Perovskite Layers for Efficient Solar Cells. *Science.* 2017, 356 (6345), 1376-1379.

3. Q. Chen, N. De Marco, Y. Yang, T.-B. Song, C.-C. Chen, H. Zhao, Z. Hong, H. Zhou, and Y. Yang, Under the Spotlight: The Organic-Inorganic Hybrid Halide Perovskite for Optoelectronic Applications. *Nano Today*. 2015, (10), 355-396.

4. G. E. Eperon, T. Leijtens, K. A. Bush, R. Prasanna, T. Green, J. T.-W. Wang, D. P. McMeekin, G. Volonakis, R. L. Milot, R. May, A. Palmstrom, D. J. Slotcavage, R. A. Belisle, J. B. Patel, E. S. Parrott, R. J. Sutton, W. Ma, F. Moghadam, B. Conings, A. Babayigit, H.-G. Boyen, S. Bent, F. Giustino, L. M. Herz, M. B. Johnston, M. D. McGehee and H. J. Snaith, Perovskite-Perovskite Tandem Photovoltaics with Optimized Band Gaps. *Science*. 2016, 354 (6314), 861-865.

5. J.H. Noh, S. H. I., J.H. Heo, T. N. Mandal, S. I. Seok, Chemical Management for Colorful, Efficient, and Stable Inorganic-Organic Hybrid Nanostructured Solar Cells. *Nano Lett*. 2013, 13 (4), 1764-1769.

6. M. R. Filip, G. E. Eperon, H. J. Snaith, and F. Giustino, Steric Engineering of Metal-Halide Perovskites with Tunable Optical Band Gaps. *Nature Communications*. 2014, 5 (5757), 1-9.

7. C. Wehrenfenning, G. E. Eperon, M. B. Johnston, H. J. Snaith, and L. M. Herz, High Charge Carrier Mobilities and Lifetimes in Organolead Trihalide Perovskite. *Adv. Mater*. 2013, 26 (10), 1584-1589.

8. C. C. Stoumpos, C. D. Malliakas, and M. G. Kanatzidis, Semiconducting Tin and Lead Iodide Perovskites with Organic Cations: Phase Transitions, High Mobilities, and Near-Infrared Photoluminescent Properties. *Inorg. Chem*. 2013, 52 (15), 9019-9038.

9. K. Hwang, Y.-S. Jung, Y.-J. Heo, F. H. Scholes, S.E. Watkins, J. Subbiah, D.J. Jones, D.-Y. Kim, and D. Vak, Toward Large-Scale Roll-to-Roll Production of Fully Printed Perovskite Solar Cells. *Adv. Mater*. 2015, 27 (7), 1241-1247.

10. R. J. Sutton, G. E. Eperon., L. Miranda, E. S. Parrott, B. A. Kamino, J. B. Patel, M. T. Hörantner, M. B. Johnston, A. A. Haghighirad, D. T. Moore, and H. J. Snaith, Bandgap-Tunable Cesium Lead Halide Perovskites with High Thermal Stability for Efficient Solar Cells. *Adv. Energy Mater.* 2016, 6 (8).

11. R. E. Beal, D. J. S., T. Leijtens, A. R. Bowring, R. A. Belisle, W. H. Nguyen, G. F. Burkhard, E. T. Hoke, M. D. McGehee, Cesium Lead Halide Perovskites with Improved Stability for Tandem Solar Cells. *J. Phys. Chem. Lett*. 2016, 7 (5), 746-751.

12. K.-L. Ou, D. T., K. X. Steirer, D. Placencia, M. Nguyen, P. Lee, N. R. Armstrong, Titanium Dioxide Electron-Selective Interlayers Created by Chemical Vapor Deposition for Inverted Configuration Organic Solar Cells. *J. Mater. Chem. A*. 2013, 1, 6794-6803.

13. R. Steim, F. R. Kogler, and C. J. Brabec, Interface Materials for Organic Solar Cells. *J. Mater. Chem.* 2010, 20, 2499-2512.

14. J.-M. Pan, B. L. Maschhoff, U. Diebold, and T. E. Madey, Interaction of Water, Oxygen, and Hydrogen with TiO_2 (110) Surfaces Having Different Defect Densities. Journal of Vacuum Science and Technology 1992, 10 (4), 2470-2476.

15. L.-M. Liu, P. C., P. Hu, The Interaction Between Adsorbed OH and O_2 on TiO_2 Surfaces. *Prog. Surf. Sci*. 2009, 84, 155-176.

16. Y. He, A. Tilocca, O. Dulub, A. Selloni, and U. Diebold, Local Ordering and Electronic Signatures, of Submonolayer Water on Anatase TiO_2 (101). *Nature Materials*. 2009, 8, 585-589.

17. P. J. Hotchkiss, S. C. Jones, S. A. Paniagua, A. Sharma, B. Kippelen, N. R. Armstrong, and S. R. Marder, Modification of Indium Tin Oxide with Phosphonic Acids: Mechanism of Binding, Tuning of Surface Properties, and Potential for Use in Organic Electronic Applications. *Acct. Chem. Res*. 2011, 45 (3), 337-346.

18. T. M. Schmidt, T. T. Larsen-Olsen, J. E. Carle, D. Angmo, and F. C. Krebs, Upscaling of Perovskite Solar Cells: Fully Ambient Roll Processing of Flexible Perovskite Solar Cells with Printed Back Electrodes. *Adv. Energy Mat*. 2015, 5.

19. E. M. Miller, Y. Zhao, C. C. Mercado, S. K. Saha, J. M. Luther, K. Zhu, V. Stevanovic, C. L. Perkins, and J. van de Lagemaat, Substrate-Controlled Band Positions in $CH_3NH_3PbI_3$ Perovskite Films. *Phys. Chem. Chem. Phys*. 2014, 16 (16), 22122-22130.

20. S. Olthof and K. Meerholz, Substrate-Dependent Electronic Structure and Film Formation of $MAPbI_3$ Perovskites. *Sci Rep*. 2017, 7.

21. Z. Jin, H. Gao, and L. Hu, Removal of Pb(II) by Nano-Titanium Oxide Investigated by Batch, XPS, and Model Techniques. *RSC Adv*. 2015, 5, 88520-88528.

22. K. E. Engates and H. J. Shipley, Adsorption of Pb, Cd, Cu, Zn, and Ni to Titanium Dioxide Nanoparticles: Effect of Particle Size, Solid Concentration, and Exhaustion. *Environ. Sci. Pollut. Res*. 2011, 18, 386-395.

23. M. S. Vohra and A. P. Davis, Adsorption of Pb(II), NTA, and Pb(II)-NTA onto TiO_2. *J. Coll. and Inter. Sci*. 1997, 194 (194), 59-67.

24. Y. Shu, R. Huang, X. Wei, L. Liu, Z. Jia, Pb(II) Removal Using TiO_2-Embedded Monolith Composite Cryogel as an Alternative Wastewater Treatment Method. *Water Air Soil Pollut*. 2017, 228.

25. D. Bi, W. Tress, M. I. Dar, P. Gao, J. Luo, C. Renevier, K. Schenk, A. Abate, F. Giodano, J.-P. C. Baena, J.-D. Decoppet, S. M. Zakeeruddin, M. K. Nazeeruddin, M. Grätzel, and A. Hagfeldt, Efficient Luminescent Solar Cells Based on Tailored Mixed-Cation Perovskites. *Sci. Adv*. 2016, 2 (1).

26. N. Pellet, P. Gao, G. Gregori, T.-Y. Yang, M. K. Nazeeruddin, J. Maier, and M. Grätzel, Mixed-Organic-Cation Perovskite Photovoltaics for Enhanced Solar-Light Harvesting. *Angew. Chem. Int. Ed*. 2014, 53, 3151-3157.

27. C. Yi, J. L., S. Meloni, A. Boziki, N. Ashari-Astani, C. Grätzel, S. M. Zakeeruddin, U. Röthlisberger, and M. Grätzel, Entropic Stabilization of Mixed A-Cation ABX_3 Metal Halide Perovskites for High Performance Perovskite Solar Cells. *Energy Environ. Sci*. 2016, 9, 656-662.

28. Y. Sun, J. P., Y. Chen, Y. Yao, and Z. Liang, Triple-Cation Mixed-Halide Perovskites: Towards Efficient, Annealing-Free and Air-Stable Solar Cells Enabled by $Pb(SCN)_2$ Additive. *Sci. Rep*. 2017, 7.

29. M. Saliba, T. Matsui, J.-Y. Seo, K. Domanski, J.-P. Correa-Baena, M. K. Nazeeruddin, S. M. Zakeeruddin, W. Tress, A. Abate, A. Hagfeldt, and M. Grätzel, Cesium-Containing Triple Cation Perovskite Solar Cells: Improved Stability, Reproducibility and High Efficiency. *Energy Environ. Sci*. 2016, 9, 1989-1997.

30. M. Stolterfoht, C. M. Wolff, Y. Amir, A. Paulke, L. Perdigon-Toro, P. Caprioglio, and D. Neher, Approaching the Fill Factor Shockley-Queisser Limit in Stable, Dopant-Free Triple Cation Perovskite Solar Cells. *Energy Environ. Sci*. 2017, 10, 1530-1539.

31. E. Mosconi, A. Amat, M. K. Nazeeruddin, M. Grätzel, and F. De Angelis, First-Principles Modeling of Mixed Halide Organometal Perovskites for Photovoltaic Applications. *J. Phys. Chem. C*. 2013, 117, 13902-13913.

32. G. Caldwell, P. K., The Hydrogen Bond Energies of the Bihalide Ions XHX- and YHX-. *Can. J. Chem* 1985, 63.

33. D. P. Nenon, J. A. Christians, L. M. Wheeler, J. L. Blackburn, E. M. Sanehira, B. Dou, M. L. Olsen, K. Zhu, J. J. Berry, and J. M. Luther, Structural and Chemical Evolution of Methylammonium Lead Halide Perovskites During Thermal Processing from Solution. *Energy Environ. Sci*. 2016, 9.

34. J. S. Manser, M. I. Saidaminov, J. A. Christians, O. M. Bakr, and P. V. Kamat, Making and Breaking of Lead Halide Perovskites. *Acc. Chem. Res*. 2016, 49, 330-338.

35. W. Xu, L. Liu., L. Yang, P. Shen, B. Sun, and J. A. McLeod, Dissociation of Methylammonium Cations in Hybrid Organic-Inorganic Perovskite Solar Cells. *Nano Lett*. 2016, 16, 4720-4725.

36. T. M. Brenner, Y. Rakita, Y. Orr, E. Klein, I. Feldman, M. Elbaum, D. Cahen, and G. Hodes, Conversion of Single Crystalline PbI_2 to $CH_3NH_3PbI_3$: Structural Relations and Transformation Dynamics. *Chem. Mater*. 2016, 28, 6501-6510.

37. J. H. Heo and S. H. Im, $CH_3NH_3PbBr_3$-$CH_3NH_3PbI_3$ Perovskite-Perovskite Tandem Solar cells with Exceeding 2.2 V Open Circuit Voltage. *Adv. Mater*. 2016, 28, 5121-5125.

38. D. Zhao, Y. Yu, C. Wang, W. Liao, N. Shrestha, C. R. Grice, A. J. Cimaroli, L. Guan, R. J. Ellingson, K. Zhu, X. Zhao, R.-G. Xiong, and Y. Yan, Low-Bandgap Mixed Tin-Lead Iodide Perovskite Absorbers with Long Carrier Lifetimes for All-Perovskite Tandem Solar Cells. *Nature Energy*. 2017, 2.

39. L. Oesinghaus, J. Schlipf, N. Giesbrecht, L. Song, Y. Hu, T. Bein, P. Docampo, and P. Müller-Buschbaum, Toward Tailored Film Morphologies: The Origin of Crystal Orientation in Hybrid Perovskite Thin Films. *Adv. Mater. Interf*. 2016, 3.

40. M. Xiao, F. H., W. Huang, Y. Dkhissi, Y. Zhu, J. Etheridge, A. Gray-Weale, U. Bach, Y.-B. Cheng, and L. Spiccia, A Fast Deposition-Crystallization Procedure for Highly Efficient Lead Iodide Perovskite Thin-Film Solar Cells. *Angew. Chem. Int. Ed*. 2014, 53, 9898-9903.

41. W. Zheng, M. Saliba, D. T. Moore, S. K. Pathak, M. T. Hörantner, T. Stergiopoulos, S. D. Stranks, G. E. Eperon, J. A. Alexander-Webber, A. Abate, A. Sadhanala, S. Yao, Y. Chen, R. H. Friend, L. A. Estroff, U. Wiesner, and H. J. Snaith, Ultrasmooth Organic-Inorganic Perovskite

Thin-Film Formation and Crystallization for Efficient Planar Heterojunction Solar Cells. *Nature Communications*. 2014, 6.

42. Q. Wu, P. Zhou, W. Zhou, X. Wei, T. Chen, and S. Yang, Acetate Salts as Nonhalogen Additives to Improve Perovskite Film Morphology for High-Efficiency Solar Cells. *ACS Appl. Mater. Interfaces*. 2016, 8 (24), 15333-15340.

43. D. Forgacs, M. Sessolo and H. J. Bolink. Lead Acetate Precursor Based P-I-N Perovskite Solar Cells with Enhanced Reproducibility and Low Hysteresis. *J. Mater. Chem. A*. 2015, 3.

44. E. Edri, S. K., M. Kulbak, G. Hodes, and D. Cahen, Chloride Inclusion and Hole Transport Material Doping to Improve Methyl Ammonium Lead Bromide Perovskite-Based High Open-Circuit Voltage Solar Cells. *J. Phys. Chem. Lett*. 2014, 5, 429-433.

45. E. Mosconi, E. Ronca, and F. De Angelis, First-Principles Investigation of the TiO_2/Organohalide Perovskites Interface: The Role of Interfacial Chlorine. *J. Phys. Chem. Lett*. 2014, 5, 2619-2625.

46. J. Burschka, N. Pellet, S.-J. Moon, R. Humphry-Baker, P. Gao, M. K. Nazeeruddin, and M. Grätzel, Sequential Deposition as a Route to High-Performance Perovskite-Sensitized Solar Cells. *Nature*. 2013, 499, 316-320.

47. S. Yang, Y. C. Zheng, Y. Hou, X. Chen, Y. Chen, Y. Wang, H. Zhao, and H. G. Yang, Formation Mechanism of Freestanding $CH_3NH_3PbI_3$ Functional Crystals: In Situ Transformation vs Dissolution-Crystallization. *Chem. Mater*. 2014, 26, 6705-6710.

48. A. Weir, P. Westerhoff, L. Fabricius, K. Hristovski, and N. von Goetz, Titanium Dioxide Nanoparticles in Food and Personal Care Products. *Environ. Sci. Technol*. 2012, 46, 2242-2250.

49. J.-Q. Xi, M. F. Schubert, J. K. Kim, E. F. Schubert, M. Chen, S.-Y. Lin, W. Liu, and J. A. Smart, Optical Thin-Film Materials with Low Refractive Index for Broadband Elimination of Fresnel Reflection. *Nature Photonics*. 2007, 1, 176-179.

50. A. Fujishima, X. Zhang, D. A. Tryk, TiO_2 Photocatalysis and Related Surface Phenomena. *Surf. Sci. Rep*. 2008, 63, 515-582.

51. A. Fujishima, T. N. Rao, D. A. Tryk, Titanium Dioxide Photocatalysis. *J. Photochem. Photobiol. C*. 2000, 1, 1-21.

52. H. Tang, K. Prasad, R. Sanjines, P. E. Schmid, and F. Levy, Electrical and Optical Properties of TiO_2 Anatase Thin Films. *J. Appl. Phys*. 1994, 75.

53. U. Diebold, The Surface Science of Titanium Dioxide. *Surf. Sci. Rep*. 2003, 48, 53-229.

54. G. D. Rajmohan, X. J. Dai, T. Tsuzuki, P. R. Lamb, J. du Plessis, F. Huang, Y.-B. Cheng, Modifying TiO_2 Surface Architecture by Oxygen Plasma to Increase Dye Sensitized Solar Cell Efficiency. *Thin Solid Films*. 2013, 545, 521-526.

55. S. Ghosh, G. G. Khan, K. Mandal, A. Samanta, and P. M. G. Nambissan, Evolution of Vacancy-Type Defects Phase Transition and Intrinsic Ferromagnetism during Annealing of Nanocrystalline TiO_2 studied by Positron Annihilation Spectroscopy. *J. Phys. Chem. C*. 2013, 117, 8458-8467.

56. M. Henderson, A Surface Science Perspective on TiO_2 Photocatalysis. *Surf. Sci. Rep*. 2011, 66, 185-297.

57. R. C. Shallcross, Y. Zheng, S. S. Saavedra, and N. R. Armstrong. Determining Band-Edge Energies and Morphology-Dependent Stability of Formamidinium Lead Perovskite Films Using Spectroelectrochemistry and Photoelectron Spectroscopy*. J. Am. Chem. Soc*. 2017, 139, 4866-4878.

58. H. Kim, K.-L. Ou, X. Wu, P. F. Ndione, J. Berry, Y. Lambert, T. Melin, N. R. Armstrong, and S. Graham. Investigation of Ultra-Thin Titania Films as Hole-Blocking Contacts for Organic Photovoltaics*. J. Mater. Chem. A* 2015, (3), 17332-17343.

59. H. Ishii, K. Sugiyama, E. Ito, and K. Seki, Energy Level Alignment and Interfacial Electronic Structures at Organic/Metal and Organic/Organic Interfaces. *Adv. Mater*. 1999, 11 (8), 605-625.

60. D. Cahen and A. Kahn, Electron Energetics at Surfaces and Interfaces: Concepts and Experiments. *Adv. Mater*. 2003, 15 (4), 271-277.

61. E. L. Ratcliff, B. Zacher, and N. R. Armstrong, Selective Interlayers and Contacts in Organic Photovoltaic Cells. *J. Phys. Chem. Lett.* 2011, 2, 1337-1350.

62. O. L. A Monti, Understanding Interfacial Electronic Structure and Charge Transfer: An Electrostatic Perspective. *J. Phys. Chem. Lett*. 2012, 3, 2342-2351.

63. S. A. Paniagua, A. J. Giordano, O. L. Smith, S. Barlow, H. Li, N. R. Armstrong, J. E. Pemberton, J.-L. Bredas, D. Ginger, and S. R. Marder. Phosphonic Acids for Interfacial Engineering of Transparent Conductive Oxides. *Chem. Rev*. 2016, 116, 7117-7158.

64. X. Pan, M.-Q. Yang, X. Fu, N. Zhang, and Y.-J. Xu, Defective TiO_2 With Oxygen Vacancies: Synthesis and Photocatalytic Applications. *Nanoscale*. 2013, 5.

65. N. Cho, F. L., B. Turedi, L. Sinatra, S. P. Sarmah, M. R. Parida, M. L. Saidaminov, B. Murali, V. M. Burlakov, A. Goriely, O. F. Mohammed, T. Wu, and O. M. Bakr. Pure Crystal Orientation and Anisotropic Charge Transport in Large-Area Hybrid Perovskite Films. *Nature Communications*. 2016, 7.

66. R. C. Shallcross, S. Olthof, K. Meerholz, and N. R. Armstrong. Chemical Interactions and Reactions between Vacuum-Deposited Methylammonium Lead Iodide ($MAPbI_3$) Perovskite Active Layers and TiO_2 Contacts. Submitted 2018.

67. J. F. Moulder, *Handbook of X-Ray Photoelectron Spectroscopy: A Reference Book of Standard Spectra for Identification and Interpretation of XPS Data*. Physical Electronics Division, Perkin-Elmer Corporation: 1992; p 261.

68. M. C. Biesinger, L. W. M. Lau, A. R. Gerson, R. St.C. Smart, Resolving Surface Chemical States in XPS Analysis of First Row Transition *Appl. Surf. Sci*. 2010, 257, 887-898.

69. P. Krishnan, M. Liu, P. A. Itty, V. Rheinheimer, M.-H. Zhang, P. J. M. Monteiro, and L. E. Yu, Characterization of Photocatalytic TiO_2 Powder Under Varied Environments Using Near Ambient Pressure X-ray Photoelectron Spectroscopy. Scientific Reports 2017, 7.

70. M. Wojdyr, Fityk: A General-Purpose Peak Fitting Program. *J. Appl. Cryst*. 2010, 43.

71. M. Tolan, *X-ray Scattering from Soft Matter Thin Films: Materials Science and Basic Research*. Springer: 1999; Vol. 148.

72. M. Setvin, J. Hulvan, G. S. Parkinson, M. Schmid, and U. Diebold. Electron Transfer Between Anatase TiO_2 and an O_2 Molecule Directly Observed by Atomic Force Microscopy. *Proc. Natl. Acad. Sci.* 2017, 114 (13), E2556-E2562.

73. J. Balajka, M. A. Hines, W. J. I. DeBenedetti, M. Komora, J. Pavelee, M. Schmid, U. Diebold, High-Affinity Adsorption Leads to Molecularly Ordered Interfaces on TiO_2 in Air and Solution. *Science*. 2018, 361 (6404), 786-789.

74. E. McCafferty and J. P. Wightman, Determination of the Concentration of Surface Hydroxyl Groups on Metal Oxide Films by a Quantitative XPS Method. *Surf. Interface Anal*. 1998, 26, 549-564.

75. S. Nakayashiki, H. D., Y. Ogomi, and S. Hayase, Interface Structure Between Titania and Perovskite Materials Observed by Quartz Crystal Microbalance System. *J. Photonics Energy* 2015, 5 (1).

76. H. Tan, A. Jain, O. Voznyy, X. Lan, F. P. Garcia de Arquer, J. Z. Fan, R. Quintero-Bermudez, M. Yuan, B. Zhang, Y. Zhao, F. Fan, P. Li, L. N. Quan, Y. Zhao, Z.-H. Lu, Z. Yang, S. Hoogland, E. H. Sargent, Efficient and Stable Solution-Processed Planar Perovskite Solar Cells via Contact Passivation. *Science*. 2017, 355 (6326), 722-726.

77. Y.-C. Lai, J.-C. Lin, C. Lee, Nucleation and Growth of Highly Oriented Lead Titanate Thin Films Prepared by a Sol-Gel Method. *Appl. Surf. Sci.* 1998, 125, 51-57.

78. M. F. Toney, S. Brennan, T. C. Huang, and Z. Rek, X-ray Depth Profiling of Iron Oxide Thin Films. *J. Mater. Res*. 1988, 3 (2), 351-356.

79. P.J. Linstrom and W.G. Mallard, Eds., NIST Chemistry WebBook, NIST Standard Reference Database Number 69, National Institute of Standards and Technology, Gaithersburg MD, 20899, https://doi.org/10.18434/T4D303, (retrieved November 17, 2018)

80. M. P. Seah and W. A. Dench, *Surf. Interf. Anal.*,1979, *1*, 2-11.

81. S. Mariotti, O. S. Hutter, L. J. Phillips, P. J. Yates, B. Kundu, and K. Durose. Stability and Performance of $CsPbBrI_2$ Thin Films and Solar Cell Devices. *ACS Appl. Mater. Interfaces.* 2018. *10*, 2750-3760

82. R. C. Shallcross, T. Stubhan, E. L. Ratcliff, A. Kahn, C. J Brabec, and N. R. Armstrong. Quantifying the Extent of Contact Doping at the Interface between High Work Function Electrical Contacts and Poly(3-hexylthiophene) (P3HT). *J. Phys. Chem. Lett.* 2015. *6*, 1303-1309